

**ELECTRODE MODIFICATION AND
CHARACTERISATION FOR MICROBIAL FUEL CELL
APPLICATIONS**

BY

SIRIRAT PHONSA

**A THESIS SUBMITTED IN PARTIAL FULFILLMENT OF
THE REQUIREMENTS FOR THE DEGREE OF MASTER OF
ENGINEERING (ENGINEERING TECHNOLOGY)
SIRINDHORN INTERNATIONAL INSTITUTE OF TECHNOLOGY
THAMMASAT UNIVERSITY
ACADEMIC YEAR 2016**

**ELECTRODE MODIFICATION AND
CHARACTERISATION FOR MICROBIAL FUEL CELL
APPLICATIONS**

BY

SIRIRAT PHONSA

**A THESIS SUBMITTED IN PARTIAL FULFILLMENT OF
THE REQUIREMENTS FOR THE DEGREE OF MASTER OF
ENGINEERING (ENGINEERING TECHNOLOGY)
SIRINDHORN INTERNATIONAL INSTITUTE OF TECHNOLOGY
THAMMASAT UNIVERSITY
ACADEMIC YEAR 2016**



ELECTRODE MODIFICATION AND CHARACTERISATION
FOR MICROBIAL FUEL CELL APPLICATIONS

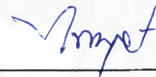
A Thesis Presented

By
SIRIRAT PHONSA

Submitted to
Sirindhorn International Institute of Technology
Thammasat University
In partial fulfillment of the requirements for the degree of
MASTER OF ENGINEERING (ENGINEERING TECHNOLOGY)

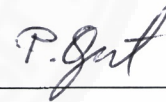
Approved as to style and content by

Advisor and Chairperson of Thesis Committee



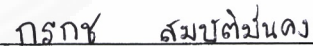
(Asst. Prof. Dr. Paiboon Sreearunothai)

Committee Member and
Chairperson of Examination Committee



(Assoc. Prof. Dr. Pakorn Opaprasit)

Committee Member



(Dr. Korakot Sombatmankhong)

Committee Member



(Prof. Dr. Kiyohiko Nakasaki)

DECEMBER 2016

Abstract

ELECTRODE MODIFICATION AND CHARACTERISATION FOR MICROBIAL FUEL CELL APPLICATIONS

by

SIRIRAT PHONSA

Bachelor of Science (Public Health),
Thammasat University, 2014

Microbial fuel cells (MFCs) have been considered as a promising technology for bioelectricity production and wastewater treatment in recent years. In order to gain a high power output in MFCs, electrode modification and characterisation were considered in this study. Granular activated carbon (GAC) and stainless steel (SS) were modified with heat treatment under N₂ flow and Polypyrrole (PPy) coating respectively. Subsequently, MnO₂ catalyst was precipitated and electrodeposited on the heated GAC and PPy-coated SS respectively to promote electrochemical activities of the MFC system. Heat treatment, PPy electropolymerisation and MnO₂ coatings affect the electrode morphology and improve electrochemical active surface area (EAS) of the electrode materials. Specifically, MnO₂/GAC (wood-based) under 600 °C and MnO₂/PPy-coated SS 304 at 100 mV s⁻¹ under 50 cycles exhibited highest EAS values of 10,080 (± 90) cm²/g and 3,962 (± 73) cm² of geometric surface area respectively. Also, the EIS results showed that the ohmic resistance of these electrode materials decreased with increasing EAS values. Moreover, FTIR, XRD and EDX results suggested that the EAS increased and the resistance decreased as a result of the presence of PPy and MnO₂ onto the electrode surface. This work has therefore established the modification processes to produce an efficient and low cost MnO₂/heated GAC and MnO₂/PPy-coated SS for enhancing electrochemical activities in MFCs.

Keywords: Microbial fuel cells, electrode materials, modification

Acknowledgements

I gratefully acknowledge National Metal and Materials Technology Center (MTEC), Sirindhorn International Institute of Technology (SIIT), Thammasat University and Thailand Advanced Institute of Science and Technology and Tokyo Institute of Technology (TAIST-Tokyo Tech), Thailand for the financial support of this research.

I would like to thank my advisor, Asst. Prof. Dr. Paiboon Sreearunothai, for his invaluable advice and his patient proofreading towards the completion of this thesis. I would also like to extend my gratitude to my committee member, Dr. Korakot Sombatmankhong, for her teaching, not only the research methodologies but also many other methodologies in life. This research would not have been completed without all the support that I have always received from them.

I would also like to thank my committee member, Assoc. Prof. Dr. Pakorn Opaprakasit, for providing knowledge and suggestions that greatly helped the research.

I would also like to acknowledge my committee member, Prof. Dr. Kiyohiko Nakasaki, for supporting as my committee member even at hardship. I would also like to thank for his guidance in the implementation of this research.

In addition, my sincere thanks go to Dr. Chinnatad Sinprasertchok who contributed an enormous intellectual and emotional support which caused the project's success.

Furthermore, I most gratefully acknowledge my family and my friends for all their support throughout the period of this research.

Finally, I would like to thank those whose names are not mentioned here but have greatly inspired and encouraged me until this research come to a perfect end.

TABLE OF CONTENTS

Chapter	Title	Page
	Signature Page	i
	Abstract	ii
	Acknowledgements	iii
	Table of Contents	iv
	List of Tables	viii
	List of Figures	ix
1	Introduction	1
	1.1 Concept and Significance	1
	1.2 Objective of the study	2
	1.3 Scopes of the study	2
2	Literature Review	3
	2.1 The concept of microbial fuel cell	3
	2.1.1 Design of MFCs	5
	2.1.1.1 Double chambered fuel cells	5
	2.1.1.2 Single chambered fuel cells	5
	2.1.1.3 Stacked MFCs	6
	2.1.2 Microorganisms used in MFCs	7
	2.1.3 Factors that affect performance of MFCs	9
	2.1.3.1 Polarisation losses	9
	2.1.3.2 Activation losses	9
	2.1.3.3 Ohmic losses	10
	2.1.3.4 Concentration losses	11

Chapter	Title	Page
	2.1.3.5 Losses due to fuel scavenging metabolic processes of microbes	11
	2.2 Electrode materials used in MFCs	12
	2.2.1 Anode materials	12
	2.2.1.1 Traditional carbon anode materials	12
	2.2.1.2 Carbon nanotubes (CNTs)	13
	2.2.1.3 Non-carbon anode materials	13
	2.2.2 Cathode materials	14
	2.3 Modification of electrode materials	14
	2.3.1 Heat treatment of AC	15
	2.3.2 Conductive polymer coating	17
	2.3.3 Electro-catalysts in MFCs	18
	2.4 Evaluation and measurement of electrode materials	19
	2.4.1 Cyclic voltammetry (CV)	19
	2.4.2 Electrochemical impedance spectroscopy (EIS)	21
	2.4.3 Fourier transform infrared spectroscopy (FTIR) analysis	21
	2.4.4 Brunauer Emmet and Teller (BET) measurement	21
	2.4.5 X-Ray Diffraction (XRD) analysis	21
	2.4.6 Scanning electron microscopy (SEM)	21
3	Materials and Methods	23
	3.1 Chemicals and materials	23
	3.1.1 Modification of granular activated carbon (GAC)	23
	3.1.2 Modification of stainless steel (SS) mesh	23
	3.2 Experimental	24
	3.2.1 Modification of GAC	24
	3.2.1.1 Preparation of GAC	24
	3.2.1.2 Heat treatment of GAC	24

Chapter	Title	Page
	3.2.1.3 Precipitation of MnO ₂ on GAC	24
	3.2.2 Modification of SS	25
	3.2.2.1 Preparation of SS mesh	25
	3.2.2.2 Electropolymerisation of PPy-coated SS mesh	25
	3.2.2.3 Electrodeposition of MnO ₂ on PPy-coated SS mesh	26
	3.3 Characterisation	27
	3.3.1 BET analysis	27
	3.3.2 FTIR analysis	27
	3.3.3 SEM analysis	27
	3.3.4 X-Ray Diffraction (XRD) analysis	27
	3.3.5 CV analysis	27
	3.3.6 EIS analysis	28
4	Results and Discussion	29
	4.1 Modification of GAC	29
	4.1.1 Effect of heat treatment on morphology	29
	4.1.2 Effect of MnO ₂ precipitation on morphology	35
	4.1.3 XRD and EDX results	37
	4.1.4 EAS of GAC electrodes	40
	4.1.5 Resistivity of GAC electrode materials	44
	4.2 Modification of SS	50
	4.2.1 Effect of the scan rate of electropolymerisation on morphology	50
	4.2.2 Effect of MnO ₂ precipitation on morphology	54
	4.2.3 XRD and EDX results	57
	4.2.4 Electropolymerisation of PPy	60
	4.2.5 Electrodeposition of MnO ₂	60
	4.2.6 Chemical properties	63
	4.2.7 EAS of SS electrode materials	64
	4.2.8 Resistivity of SS electrode materials	71

Chapter	Title	Page
5	Conclusions and Recommendations	77
	5.1 Conclusions	77
	5.2 Recommendations	78
	References	79
	Appendices	84
	Appendix A	85
	Appendix B	87
	Appendix C	89
	Appendix D	90

List of Tables

Tables	Page
2.1 Basic components of microbial fuel cells	7
2.2 Microbes used in MFCs	8
2.3 Comparison of the properties of traditional anode materials in MFCs	14
2.4 The advantages and disadvantages of existent modification methods	15
2.5 Summary of reviews on the heat treatment under inert atmosphere	16
4.1 Surface area and micropore structure parameters of GAC samples	34
4.2A Elemental composition of various GAC (coal-based) electrodes	39
4.2B Elemental composition of various GAC (wood-based) electrodes	39
4.3A The active electrode surface area of GAC (coal-based) electrodes	43
4.3B The active electrode surface area of GAC (wood-based) electrodes	43
4.4A The resistance of GAC (coal-based) electrodes in 0.1M KCl solutions	49
4.4B The resistance of GAC (wood-based) electrodes in 0.1M KCl solutions	49
4.5A Elemental composition of various SS304 electrodes	59
4.5B Elemental composition of various SS316 electrodes	59
4.6A The active electrode surface area of SS 304 electrodes	69
4.6B The active electrode surface area of SS 316 electrodes	69
4.7A The active electrode surface area of SS 304 electrodes (2)	70
4.7B The active electrode surface area of SS 316 electrodes (2)	70
4.8A The passive film resistance of SS 304 electrodes in 0.1M KCl solutions	76
4.8B The passive film resistance of SS 316 electrodes in 0.1M KCl solutions	76

List of Figures

Figures	Page
2.1 Operating principles of a double chambered microbial fuel cell	3
2.2 A schematic of electron transfer mechanisms of microbes	4
2.3A A simple design of double chambered microbial fuel cell	5
2.3B Schematic design of cylindrical membrane-less fuel cells	5
2.4 Schematic design of single chambered microbial fuel cell	6
2.5 Schematic design of stacked type microbial fuel cell	6
2.6 Typical conducting polymers	17
2.7 Electropolymerisation process of PPy	18
3.1 The set-up of electropolymerisation, electrodeposition and EAS analysis	25
3.2 Diagram of electropolymerisation	26
3.3 Diagram of electrodeposition	26
3.4 The set-up of EIS analysis	28
4.1 SEM images GAC (coal-based) at 500 magnification	30
4.2 SEM images GAC (coal-based) at 10,000 magnification	31
4.3 SEM images GAC (wood-based) at 500 magnification	32
4.4 SEM images GAC (wood-based) at 10,000 magnification	33
4.5 Change in specific surface area ($BET_{\text{singlepoint}}$) of GAC after heat treatment under N_2 flow	34
4.6 SEM images of MnO_2 /GAC (coal-based) at 500 and 20,000 magnification	35
4.7 SEM images of MnO_2 /GAC (wood-based) at 500 and 20,000 magnification	36
4.8 XRD spectra of MnO_2 sediment and uncoated GAC samples	37
4.9 EDX analysis of MnO_2 electrodeposited on different GAC electrodes	38
4.10 CV of various GAC (coal-based) and GAC (wood-based) electrodes at the same potential scan rate of 25 mV s^{-1}	41
4.11 Graphs plotted between the peak currents and square root of the scan rates according to the Randles-Sevcik equation.	42
4.12 Bode-phase plots of GAC (coal-based) and GAC (wood-based) electrode materials	45

Figures	Page
4.13 Nyquist plots of GAC (coal-based) and GAC (wood-based) electrode materials in 0.1 M KCl solutions	46
4.14 Overlaid experimental and fitted Nyquist plots and Bode-phase plots with equivalent circuit elements of GAC (coal-based) under 600 °C in 0.1M KCl solutions	47
4.15 The electrode material resistance GAC (coal-based) and GAC (wood-based) in 0.1 KCl solutions	48
4.16 Weight of PPy coated onto SS 304 and PPy coated onto SS 316 surface after electropolymerisation at various scan rates (50cycles and 100cycles)	51
4.17 SEM images of PPy-coated SS 304 using different scan rates and number of cycles of electropolymerisation at 3k magnification	52
4.18 SEM images of PPy-coated SS 316 using different scan rates and number of cycles of electropolymerisation at 3k magnification	53
4.19 SEM images of bare SS 316 and bare SS 304 mesh at 3k magnification	54
4.20 SEM images of MnO ₂ /bare SS 304 at 500 and 50,000 magnification	55
4.21 SEM images of MnO ₂ /bare SS 316 at 500 and 50,000 magnification	56
4.22 XRD spectra of MnO ₂ deposited on the SS surface	57
4.23 EDX analysis of MnO ₂ electrodeposited on different SS304 and SS316 electrode materials.	58
4.24 CV of PPy-coated SS recorded at various cycles of the same potential scan rate of 400 mV s ⁻¹ and various scan rates of the same of 100 th cycle	61
4.25 CV for electrodeposition of MnO ₂ on SS 304 and SS 316 substrates at potential scan rate of 200 mV s ⁻¹	62
4.26 FTIR spectrum of PPy coated on stainless steel substrate	63
4.27 CV of various SS 304 electrodes at the same potential scan rate of 25 mV s ⁻¹	65
4.28 CV of various SS 316 electrodes at the same potential scan rate of 25 mV s ⁻¹	66

Figures	Page
4.29 Graphs plotted between the peak currents and square root of the scan rates according with the Randles-Sevcik equation. The peak currents were recorded on various SS 304 electrodes	67
4.30 Graphs plotted between the peak currents and square root of the scan rates according with the Randles-Sevcik equation. The peak currents were recorded on various SS 316 electrodes	68
4.31 Bode-phase plots of SS 304 and SS 316 electrode materials	72
4.32 Nyquist plots of SS 304 and SS 316 electrode materials in 0.1 M KCl solutions	73
4.33 Overlaid experimental and fitted Nyquist plots and Bode-phase plots with equivalent circuit elements of the bare SS 304 in 0.1M KCl solutions	74
4.34 The electrode material resistance of SS 304 and SS 316 in 0.1 KCl solutions	75

Chapter 1

Introduction

1.1 Concept and Significance

Currently, Microbial fuel cells (MFCs) are a renewable energy technology which has gained wide attention of many researchers because of the broad range of applications, including biohydrogen production, electricity generation, wastewater treatment or bio-sensing [1]. The research in this field has been the comprehension over the energy climate and environmental pollution crises. MFCs exactly encounter the need to relieve the previous-mentioned problems as they can not only generate power output but also have a significant capability for wastewater treatment [2]. MFCs are bioreactors which use microbes as the catalysts to oxidise organic compounds and directly convert chemical energy into electrical energy. Electron generated by microbes from organic compounds are transferred to the anode electrode and flow to the cathode electrode linked by a resistor. The power output relies on the rate of substrate degradation, the rate of electron transfer from the microorganisms to the anode electrode, the circuit resistance, the proton mass transfer in the liquid, the performance of the electrode and the external operating conditions and so on. Various electrode materials differ in their physical and chemical characteristics (e.g., surface area, electrical conductivity, and chemical stability), therefore, they also differ in their effect on bacteria adhesion, electron transfer, electrode resistance and the rate of electrode surface reaction [2].

One of the most significant problems to MFCs is their low power production as a result of high internal resistance, especially from electrode materials. Increasing electrode surface area is one way of solutions to reduce the charge transfer resistance between electrode and electrolyte (or wastewater) in the MFC system. The majority of active electrode materials are carbon, conductive polymers and metal oxides [3]. Among the various types of electrode materials, stainless steel (SS) and Granular activated carbon (GAC) show high flexibility, low resistance, inexpensive, easy accessibility and more easily scaled to larger geometries. Some disadvantages of these materials are low surface area, biocompatibility issues and corrosion. Therefore, in

order to be appropriate materials of MFCs, SS and GAC should have a very high surface area, electrical conductivity and suitable for bacteria adhesion.

Polypyrrole (PPy) is one of the most promising conducting polymers that have been coated on the metal surface due to its high conductivity, environmental stability, biocompatibility, corrosion protection, economic advantages and ease of synthesis [4-6]. Wang and Northwood (2006) have reported that PPy coating, coated using a cyclic voltammetric (CV) method, can provide corrosion resistance for polymer exchange membrane fuel cells (PEMFCs). In this paper, they indicated that the polymer-deposited 316L stainless steel plates presented enhanced corrosion protection with an acceptable contact resistance.

In order to replace the costly platinum (Pt) catalyst, manganese oxide (MnO_2) has been used to have excellent performance for bioelectrochemical systems due to its low cost, abundance in nature, high surface area, mild oxidising properties and good stability in acidic condition [3, 7, 8].

Consequently, it is of great importance to choose and improve appropriate electrode materials to optimise and develop the performance of MFCs.

1.2 Objective of the study

The aim of this study is modification of electrode materials for electrochemical activity enhancements for microbial fuel cell applications.

1.3 Scopes of the study

The scopes of this study involve modification of two electrode materials as follows;

- (1) Granular activated carbon (coal-based) and granular activated carbon (wood-based) modified using
 - heat treatment
 - metal catalyst loading with MnO_2
- (2) Austenitic stainless steel (SS304 and SS316) modified using
 - conductive polymer coating with PPy
 - metal catalyst loading with MnO_2

Chapter 2

Literature Review

2.1 The concept of microbial fuel cell

Microbial fuel cells (MFCs) are bio-electrochemical system which produce a current using microbes as the catalysts to oxidise organic compounds and convert chemical energy into electrical energy [9]. The MFC applications consist of two electrodes, such as an anode and cathode electrode, in the existence of an electrolyte or wastewater (as shown in **Fig. 2.1**). Electroactive bacteria (anodophiles) resided in these substrates produce electrons, protons and carbon dioxide. In the nonexistence of oxygen, the electrons are flowed to the anode surface and transferred to the cathode electrode connected by an external circuit thus generating electricity. Electron transfer from the anodophiles to the anode surface may produce by direct electron transfer (DET), via either direct contact or nanowires, or by mediated electron transfer (MED), which involves the use of exogenous and/or endogenous mobile electron shuttles (**Fig. 2.2**) [10].

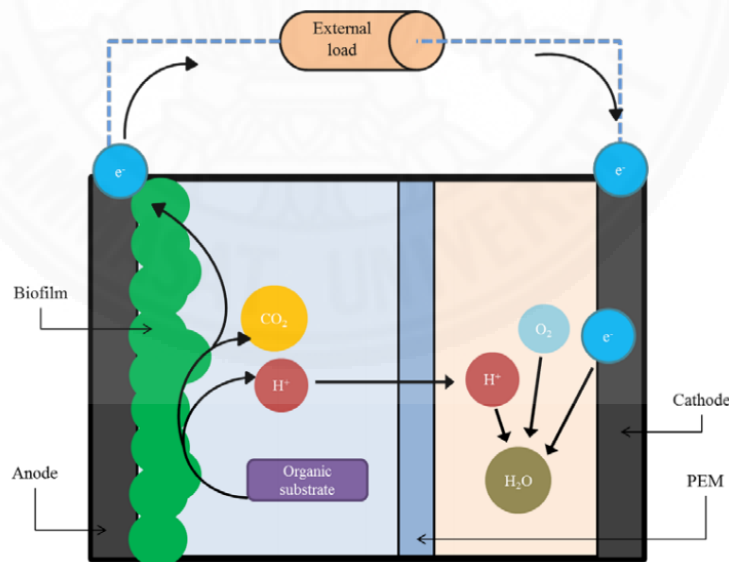


Fig. 2.1 Operating principles of a double chambered microbial fuel cell [10].

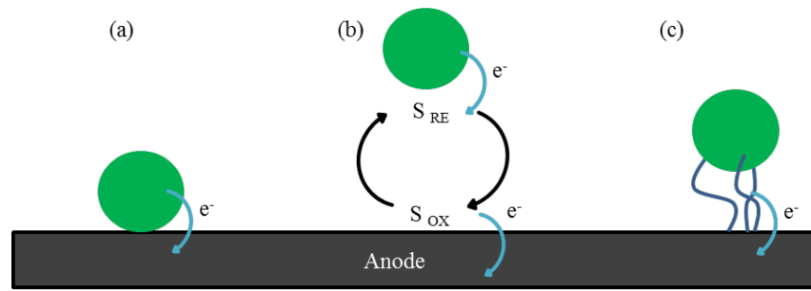
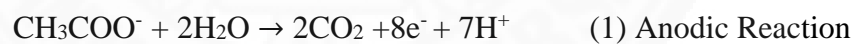


Fig. 2.2 A schematic of three electron transfer mechanisms of microbes at the anode surface: (a) direct transfer by contact; (b) indirect electron transfer by redox shuttles (S_{RE} = reduced electron shuttle, S_{OX} = oxidized electron shuttle); (c) electron transfer by conductive nanowire matrix [10].

Normally, carbon-based materials are used as the electrodes, such as carbon cloth, carbon paper, graphite rods, plates, granules, reticulated vitreous carbon and activated carbon [11]. The anode material must have a large surface area and pore volume to provide the bacteria growth. The catalysts, such as platinum (Pt), is usually coated on the cathode electrode, to improve the rate of oxygen reduction reactions at the cathode surface [10].

Typical electrode reactions are shown below using acetate as an example substrate [12].



Based on the above reaction, MFC systems can efficiently produce power [13]. The capability of the systems to oxidise substrate affects the extent of power production. The efficiency of the system depends on various factors. Optimisation of these factors can solve energy crisis in an efficient way to utilise the wastewater to generate electricity.

2.1.1 Design of MFCs

The common MFCs compose of the anodic chamber and cathodic chamber connected by a proton exchange membrane (PEM). Various types of MFC designs have been improved of which have 3 main forms [5]:

2.1.1.1 Double chambered fuel cells

The simplest type of MFC is the double chambered system. This fuel cell has both of cathode and anode compartments which are connected with a PEM (**Fig. 2.3A**). They are sometimes membrane-less (**Fig. 2.3B**). These configurations accomplish the reaction process and they can prevent oxygen to oxidise the anode electrode. These chambers can be used for generating higher power production and can be utilised to obtain power in various unreachable conditions. Moreover, they are suitable to scale up for large quantity of wastewater treatment and electricity generation.

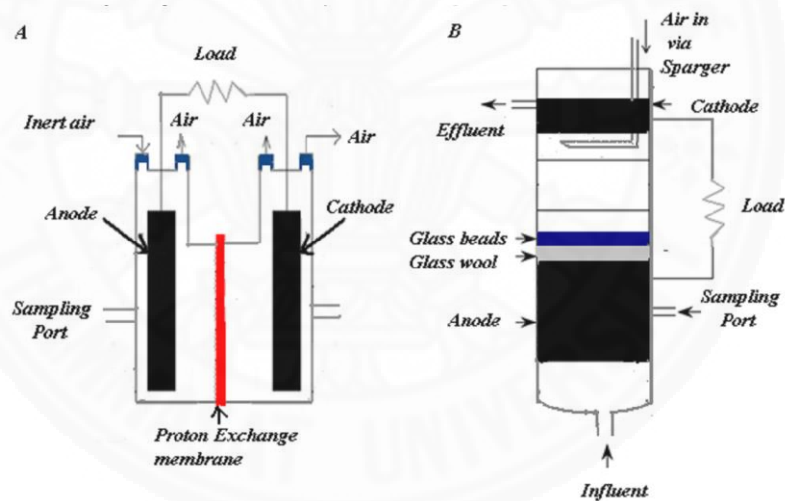


Fig 2.3 A) A simple design of double chambered microbial fuel cell B) schematic design of cylindrical membrane-less fuel cells [13].

2.1.1.2 Single chambered fuel cells

Single chambered system, which directly contacted to atmosphere as the oxygen source, has only the cathode chamber (**Fig. 2.4**). The air-cathode configurations are easier to compact than other systems. They are easier to scale up than the double chambered systems. Moreover, the costs of operation are decreased due to the absence of oxygen pumping [10]. Carbon electrodes used as the anodes are

common. The cathodes should be porous carbon electrodes. Porous cathode utilises oxygen from air and transfers proton disperse through cathode surface. Graphite is used as the cover onto cathodes for drying prevention of the membrane and cathode. Thus, the particular issue in these figurations is water management or better fluid management.

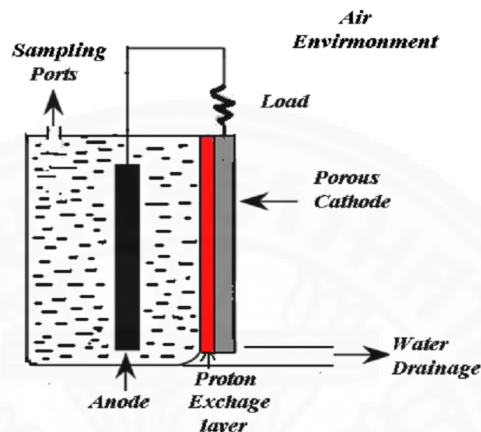


Fig. 2.4 Schematic design of single chambered microbial fuel cell [13].

2.1.1.3 Stacked MFCs

Another type of MFC configurations are stacked MFCs for battery formation as shown in **Fig. 2.5**. This configuration can improve the production of overall battery compared to typical power source. These can be stacked in series or in parallel which are higher in power output than other types.

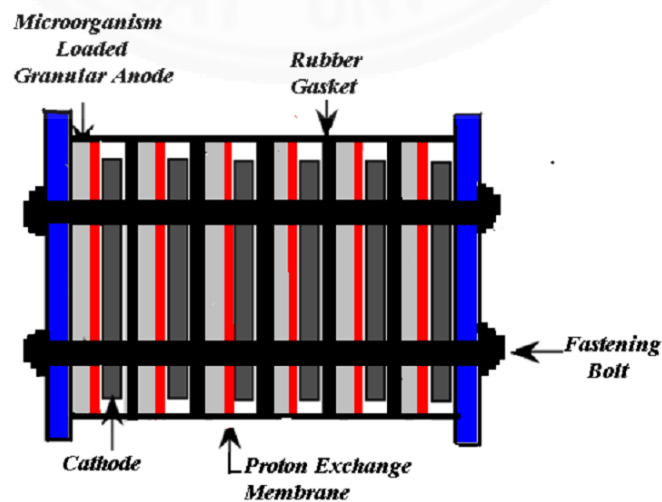


Fig. 2.5 Schematic design of stacked type microbial fuel cell [13].

Table 2.1 shows a summary of MFC components and the materials used to operate them.

Table 2.1 Basic components of microbial fuel cells [12].

Items	Materials	Remarks
Anode	Graphite, graphite felt, carbon paper, carbon-cloth, Pt, Pt black, reticulated vitreous carbon (RVC)	Necessary
Cathode	Graphite, graphite felt, carbon paper, carbon-cloth, Pt, Pt black, RVC	Necessary
Anodic chamber	Glass, polycarbonate, Plexiglas	Necessary
Cathodic chamber	Glass, polycarbonate, Plexiglas	Optional
Proton exchange system	Proton exchange membrane: Nafion, Ultrex, polyethylene.poly (styrene-co-divinylbenzene); salt bridge, porcelain septum, or solely electrolyte	Necessary
Electrode catalyst	Pt, Pt black, MnO ₂ , Fe ³⁺ , polyaniline, polypyrrole, electron mediator immobilized on anode	Optional

2.1.2 Microorganisms used in MFCs

Many microorganisms, which produce the electrons from oxidation of organic substrates, possess the capability to transfer the electrons to the anode electrode.

Table 2.2 shows a list of microorganisms with their substrates.

Table 2.2 Microbes used in MFCs [12].

Microbes	Substrate	Application
<i>Actinobacillus succinogenes</i>	Glucose	Neutral red or thionin as electron mediator
<i>Aeromonas hydrophila</i>	Acetate	Mediator-less MFC
<i>Alcaligenes faecalis</i> , <i>Enterococcus gallinarum</i> , <i>Pseudomonas aeruginosa</i>	Glucose	Self-mediate consortia isolated from MFC
<i>Clostridium beijerinckii</i> , <i>Clostridium butyricum</i>	Starch, glucose, lactate	Fermentative bacterium
<i>Desulfovibrio desulfuricans</i>	Sucrose	Sulphate/sulphide as mediator
<i>Erwinia dissolven</i>	Glucose	Ferric chelate complex as mediators
<i>Escherichia coli</i>	Glucose, sucrose	Mediators such as methylene blue needed.
<i>Geobacter metallireducens</i> , <i>Geobacter sulfurreducens</i>	Acetate	Mediator-less MFC
<i>Gluconobacter oxydans</i>	Glucose	Mediator (HNQ, resazurin or thionine) needed
<i>Klebsiella pneumoniae</i>	Glucose	HNQ as mediator biomineralised manganese as electron acceptor
<i>Lactobacillus plantarum</i>	Glucose	Ferric chelate complex as mediators
<i>Proteus mirabilis</i>	Glucose	Thionin as mediator
<i>Pseudomonas aeruginosa</i>	Glucose	Pyocyanin and phenazine-1-carboxamide as mediator
<i>Rhodoferax ferrireducens</i>	Glucose, xylose, sucrose	Mediator-less MFC
<i>Shewanella oneidensis</i>	Lactate	Anthraquinone-2,6-disulfonate (AQDS) as mediator
<i>Shewanella putrefaciens</i>	Lactate, pyruvate, acetate	Mediator-less MFC
<i>Streptococcus lactis</i>	Glucose	Ferric chelate complex as mediators

2.1.3 Factors that affect performance of MFCs

2.1.3.1 Polarisation losses

Under open circuit conditions, MFC can obtain a highest cell voltage of 1.1 V in ideal performance. However, in actual MFC performance it tolerates various forms of polarisation losses and can attain only 0.8 V under open circuit conditions and approximately 0.62 V during current production. The difference of overvoltage between ideal and measured cell voltage presents the electrode overpotentials which contributes to an overall ohmic loss of the system. Most of these overpotentials result from intracellular and extracellular potential losses that appear in biofilm coated on anode electrode. When the internal resistance is so high, there is an important loss of charge in the system, thus reducing the effective voltage available at the end terminal [14].

2.1.3.2 Activation losses

An energy obstacle must be solved in order to stimulate the charge transportation which released by oxidation to the anode electrode. The energy obstacle consists of the activation overpotential that is an auxiliary potential. This overpotential is needed for transport of electrons from fuel to shuttles of microbes and eventually to the anode electrode. Activation losses are noted as the extreme decrease in MFC voltage (low polarisation) at the primary low current density. However, ohmic and concentration losses, that normally appear at intermediate or high current density, can dominate activation loss. Obviously, activation losses appear at both anode and cathode electrode. It is significant to note that the cathodic overpotentials are much higher than anodic overpotentials. This overpotential can be decreased with the increased exchange current density [14].

Some steps that can be preferred to minimise the activation losses are:

- **Increasing anode surface area**

In order to reduce the activation potential, increasing the surface area is the reliable method because the current densities get decreased with increasing in the surface area. Increasing the surface porosity and roughness of electrode materials can improve it.

- **Improving anode-microbe interactions**

It is important to increase microbial interactions at the anode electrode for decreasing activation losses at the microorganisms. Raising electron transfer with the use of mediator would get rid of this problem. When the mediators are located within the cell membrane, the intracellular activation losses are reduced as well. MFC systems operating microbes that generate conducting pili have relatively low activation polarisation.

- **Increasing the operating temperature**

Increasing the temperature in the inorganic fuel cell would decrease the activation potential. However, in the MFC system, it is not probable to raise the temperature except when the bio-reaction compartment is divide from the anode chamber.

- **Decreasing the activation loss at the electrode surface**

Catalyst addition at the electrode can decrease the activation energy at the electrode surface. Pt, which is observed to get contaminated by bacteria suspensions, has been extensively used as the catalyst. It has been studied that some achievement has been completed by coating the electrode with the conductive film that yield microorganisms from direct contact with the catalyst material [15]. Neutral red and manganese oxide catalysts are reported as good alternative to Pt because of economic advantages. Furthermore, immobilisation of these catalysts onto the electrode surface have presented to improve MFC power generation [16, 17].

2.1.3.3 Ohmic losses

When the flow of charge is blocked as a result of anodic resistance, the medium polarisation such as ohmic losses are occurred. The potential drop can be clearly presented by ohms law as shown in **Eq. 1** where R_i represents the total internal resistance and I is the circuit current [12].

$$\Delta V = I \times R_i \quad (\text{Eq. 1})$$

These losses can be limited by increasing the anode conductivity, reducing contact resistance and decreasing the total travel distance of electrons inside the anode

electrode [14]. In order to overcome the ohmic losses, the use of extremely conductive anode materials has exhibited to generate higher current production.

2.1.3.4 Concentration losses

Increasing anode potential and decreasing cathode potential (or concentration losses) may result from imbalance in rate of mass transfer of substrate and products to and from the anode electrode respectively and the total current produced in the system. These losses occur most often at high current density because of diffusion-restricted mass transfer of fuel to the anode surface. In addition, the redox conditions and the metabolic activities of the microorganisms may be changed by the accumulation of oxidised products and cations within the biofilm. Barrier in cation transfer may lead to a pH gradient between the electrode materials causing an important decrease in the power generation [14]. Concentration losses can be solved with anode design and parameter operation.

2.1.3.5 Losses due to fuel scavenging metabolic processes of microbes

Catabolic activities of the bacteria while obtaining energy from fuel oxidation can cause the voltage loss. An efficient MFC, the anode potential should be as low as possible to permit achievement of high MFC voltage and sufficient catabolic energy attain for the existence of microbes. However, electron transfer, that causes fermentation during high energy production, can be hindered by very low anode potential resulting in electron loss. Moreover, this results in added electron losses by excessive buildup of anodophilic biomass. The microbial metabolic losses resulted from various factors such as microbial types, community composition, microbial interaction, fuel degradation rate by the microorganisms, number of active microbes and mix up of fuel through the electrolyte between the electrodes [14].

2.2 Electrode materials used in MFCs

One of the most important roles in the performance and cost of MFC systems is electrode materials. They can be mainly classified into two categories such as anode, and cathode electrode materials [2].

2.2.1 Anode materials

The anode materials should have a good properties such as good electrical and low resistance, good biocompatibility, chemical stability and corrosion resistance, large surface area and appropriate mechanical strength and toughness [18]. Anode materials can be divided into three categories, such as traditional carbon anode materials, carbon nanotubes (CNTs) and non-carbon anode materials. **Table 2.3** [2] shows comparison of the properties of traditional anode materials in MFC systems.

2.2.1.1 Traditional carbon anode materials

Carbon electrode materials are broad used in anode electrode as following: graphite fiber brush, carbon cloth, graphite rod, carbon paper, reticulated vitreous carbon (RVC) and carbon felt because they have a high electric conductivity and large surface area [2]. Furthermore, graphite granule (GG) and granular activated carbon (GAC) have been used in anode electrode due to their high degree of microporous surface area and catalytic activities. Also, they are inexpensive with higher conductivity [18].

GAC is normally used for material packing in wastewater treatment procedures because it is cheap and enduring material with a high surface area (approximately $1,000 \text{ m}^2 \text{ g}^{-1}$). Their stabilities could greatly increase microbial attachment and might be used as an appropriate anode materials in MFC systems [2]. Jiang, D. and B. Li (2009) [19] utilised GAC as the anode material, obtaining a power density which represented a great improve from 4.2 to 7.2 W m^{-3} with increasing the amount of GAC from 400 to 700 g . This result showed that the power output of MFC systems improved with increase in the amount of GAC because of a higher amount of bacteria adhesion.

2.2.1.2 Carbon nanotubes (CNTs)

One of the greatest potential electrodes is CNTs due to their high specific surface area, high mechanical strength and ductility, and excellent stability and conductivity [2]. Conductive polymer-modified CNTs have obtained great attention because they can result in an accompanying effect.

CNTs can enhance the performance of MFC systems due to their large specific surface area (normally a few hundred to 1300 m² g⁻¹). The channel gaps which are formed between CNTs bundles and the outside surface area of CNTs bundles are assumed to be approachable by large sorbate species such as microbes. Therefore, CNTs have an increased surface area that is efficient for microscale microbes and importantly higher than that of traditional microporous carbon electrodes [2]. On the other hand, clogging problems of these anode materials are still reported in MFC applications for wastewater treatment [20]. Also, an expensive production (\$80–100) of CNTs is a main factor. Moreover, the modification of CNTs is complicated and high-priced which also limits their larger scale development.

2.2.1.3 Non-carbon anode materials

Although various reports have attempted to use non-carbon materials, carbon-based materials are basically consider as the greatest versatile anode materials. Stainless steel (SS) electrodes were tested in MFC systems in place of the traditional carbon electrodes. Dumas et al. (2007) [21] attempted to use stainless steel (SS) as the electrode, but the maximum power density was only 4 mW m⁻² but Richter et al. (2008) [22] improved an MFC system using highly conductive gold as the anode with *Geobacter sulfurreducens*, and a steady current of 0.4 to 0.7 mA was generated. Although this MFC can attain a high power production, practical system limits its larger scale production [2]. SS was found to have lower performance than carbon but would be more easily scaled to larger geometries. Although not the focus of the paper, Manohar et al. (2009) [23] showed that addition of SS balls to a graphite electrode reduced the resistance of MFC system. This could be purely a result of increased surface area.

Table 2.3 Comparison of the properties of traditional anode materials in MFCs.

Anode materials	Advantages	Disadvantages
Graphite rod	Good electrical conductivity and chemical stability, relatively cheap, and easy to get	Difficult to increase the surface area
Graphite fiber brush	Higher specific surface areas, easy to produce	Clogging
Carbon cloth	Large relative porosity	Expensive
Carbon paper	Easy to connect wiring	Lack of durability, fragile
Carbon felt	Large aperture	Large resistance
RVC	Good electrical conductivity and plasticity	Large resistance, fragile
Stainless steel	High conductivity, cheap, easy accessibility	Low surface area, biocompatibility issues, corrosion
Activated carbon	High mechanical strength, specific surface areas and long-term durability	May Clogging

2.2.2 Cathode materials

The cathode materials also have a major influence on the power generation in MFC systems. The good cathode materials should be a high redox potential and easily to capture protons [2]. Recently, graphite, carbon cloth and carbon paper cathode materials are common.

2.3 Modification of electrode materials

An efficient method to enhance the performance of MFC systems is electrode modification because it improved the physical and chemical properties to provide for better electron transport and bacteria attachment. This part will concentrate on some conventional modification methods for activated carbon (AC) and SS.

Recently, modifying these properties have considered in several research. Modification of granular or powdered AC was studied in order to simplify a concentrated discussion. **Table 2.4** [24] present and compare the advantages and disadvantages of existent modification methods.

Table 2.4 The advantages and disadvantages of existent modification methods.

Modification	Treatment	Advantages	Disadvantages
Chemical properties	Acidic	Enhances acidic functional groups on AC surface. Enhances chelation ability with metal species	May decrease BET surface area and pore volume
	Basic	Improves uptake of organics	May, in some cases, decrease the uptake of metal ions
Physical properties	Heat	- Increases BET surface area and pore volume - Decreases oxygen surface functional groups	
Biological properties	Bioadsorption	Extends AC bed life by rapid oxidation of organics by microbes before the material can occupy adsorption sites	Thick biofilm encapsulating AC may impede diffusion of adsorbate species

2.3.1 Heat treatment of AC

Heat treatment under inert atmosphere (Nitrogen or helium) at high temperature approximately $>700\text{ }^{\circ}\text{C}$ might be modified to particularly remove some acidic functionalities from the AC surface. In addition, this treatment can enhance carbon hydrophobicity by deleting hydrophilic surface functionalities. The majority of oxygen functionalities on a carbon surface can be decomposed at $800\text{ to }1000\text{ }^{\circ}\text{C}$ [25].

Heat treatment is limited to 1000 °C resulting a low degree of activity for reacting with oxygen of chemical agents and a high degree of basicity of material.

Heat treatment of carbon mesh was studied by Wang et al. [2] using muffle furnace in order to heat this electrode at 450 °C for 30 minutes. It led to a maximum power density of 922 mW m⁻² (46 W m⁻³); this was 3% higher than that generated using a mesh anode which was only treated with acetone (893 mW m⁻²; 45 W m⁻³). These modification affected such a change in power density. The heat treatment method could modify the electrochemical activities by enhancing the electrochemically active surface area (EAS) and reducing the O/C ratio, which caused the EAS enhancing by 190% and the charge transfer coefficients enhancing by 44% compared to the untreated electrode. **Table 2.5** [25] shows the summary of research reviews on the heat treatment under inert atmosphere.

Table 2.5 Summary of reviews on the heat treatment under inert atmosphere.

Materials	Treatment	References
Granular activated carbons (GACs)	Under H ₂ flow at 900 °C	S.A. Dastgheib et al., 2004
	Under N ₂ flow at 900 °C	
Activated carbon fibers (ACFs)	Under H ₂ flow at 600, 800, 900 °C	J. Muniz et al., 1998
Norit ROX activated carbon	Under N ₂ flow at 700 °C	M.F.R. Pereira et al., 2003
	Under H ₂ flow at 700, 900 °C	
Commercial activated carbon (AC)	Under N ₂ flow at 1000 °C	M. Koh et al., 2000
Norit C-Granular (Nc) activated carbon	Under N ₂ flow at 500, 950 °C	J.A. Menéndez et al., 1995
	Under H ₂ flow at 600, 650, 800, 950 °C	J.A. Menéndez et al., 1996
Carbon black	Under N ₂ flow at 800 °C	A. Dandekar et al., 1998

2.3.2 Conductive polymer coating

For the corrosion protection of SS, the conductive polymer such as polyaniline (PAni), polypyrrole (PPy), and polythiophen (Pthio) as in **Fig. 2.6** [26] have been prepared by electrochemical oxidation in liquid phase. Wessling, B. (1994) [27] indicated that the conductive polymer coating of PAni and PPy possibly controlled self-healing properties, in which oxidative ability of conductive polymer can improve a flawed site on the passive oxide between the metal substrate and the conductive polymer.

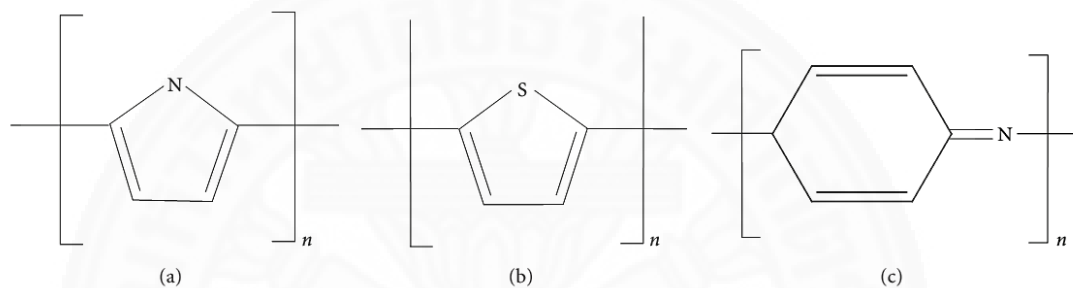


Fig. 2.6 Typical conducting polymers: (a) polypyrrole (PPy), (b) polythiophen (PThio), and (c) polyaniline (PAni) [26].

In order to enhance the electrochemical conductivity, oxidative polymerisation and the doping of anions into polymer have been studied by many research [26]. **Fig. 2.7** shows the electropolymerisation process of PPy using cyclic voltammetry (CV) method. When the electrode material is anodically applied in a pyrrole (Py) solution, the metal substrates are oxidised to shift to the passive state. And then, the steels are coated by the passive oxide formed beneath the conductive polymer. Therefore, the black polymer film can be seen onto the electrode material. The electrolyte solution should be deoxygenated by inert gas bubbling because Py monomer can be oxidised by oxygen in the atmosphere.

The conductive polymer could not only enhance a protective effect for the bacteria but also provide the electro-catalytic activities of the catalyst [2]. Zou, Y., et al. (2008) [28] used PPy-coated CNTs as the anode material and the results presented that the modification of carbon paper had better electrochemical activities. Tsai, H.-Y., et al. (2009) [29] concerned that the performance of MFC systems could be improved

using the modified carbon paper. The power density and cell voltage of this modified electrode improved by approximately 148% and 147% respectively, compared to the unmodified electrode.

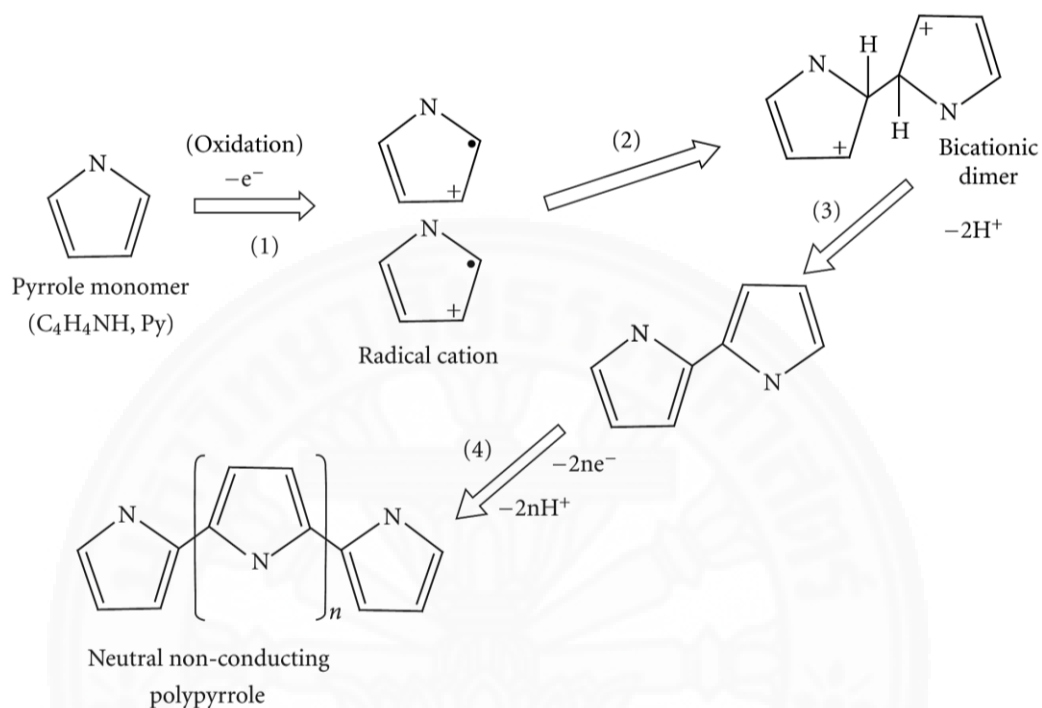


Fig. 2.7 Electropolymerisation process of PPy [26].

2.3.3 Electro-catalysts in MFCs

In the MFC system, the rate of mass and electron transfer at the interfaces of electro-catalytic solution have an influence on the catalytic reaction. [7]. Thus, the consideration of the structures, surface characteristics, and conductivities of electrode catalysts is significant.

One of the important roles of most potential losses in MFC systems is oxygen reduction reactions (ORR). The main prosperous catalyst for ORR is Pt due to its large specific surface area, high reaction rate and low over potential for ORR [30]. The procedure to decrease the over potential of ORR and to substitute the typical expensive Pt catalyst in MFC system has been considered in the recent years.

In order to replace this costly catalyst, noble metal (such as Pt and Pd), non-noble metal (such as Ni, SS and MnO₂) and carbon-based (such as AC, CNT, graphene and graphite) catalysts are applied for bioelectrochemical systems [7]. From the electrocatalysts reviews [2] Non-Pt catalysts of electrode such as CoTMPP and iron phthalocyanine (FePc) based oxygen reduction catalysts were used more often, and they were proved to be cheap and effective options for MFC systems. Manganese oxides and rutile were also applied. From the results, the fibrous MnO₂ electrode materials are better to deposited on electrode materials due to the following: (a) high catalytic activities; (b) better contact between MnO₂ and the electrical conductive materials; (c) high charge-transfer rate due to a smaller diameter (thus it is expected that the specific surface area would be higher) and (d) a low overpotential [31, 32]. From Suhasini (2013) study, the results showed that CV method was a good procedure to electrodeposit MnO₂ on SS substrate compared to galvanostatic, potentiostatic and potentiodynamic methods [3]. Deposition of the oxide layer on the SS substrate prepared using the CV method between 1 and 1.6 V could have led to a large porous oxides resulting in high capacitance.

2.4 Evaluation and measurement of electrode materials

It is significant to select suitable methods to analyse and evaluate the performance of electrode materials used in MFC systems. These methods are discussed in the following section.

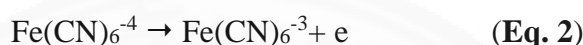
2.4.1 Cyclic voltammetry (CV)

A regular method in electrochemistry that has been extensively used in MFC systems is CV. It is designated as electroanalytical procedure to study electrochemical active species by observing the mechanisms of electrode reactions and evaluating the performance of electrode materials and catalysts [2]. It measures redox behavior of chemical species within a wide potential range. A triangular excitation potential is shown as the resulting current at the working electrode. Thus, basic information regarding the redox reaction can be analysed from the resulting CV. CV procedures basically use a three-electrode system to gain precise the experimental results. The anode and cathode is used as the working electrode, another electrode is

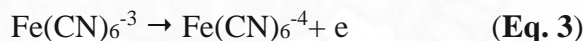
indicated as a counter electrode and the other electrode is connected to a reference electrode such as Ag/AgCl or saturated calomel electrode: SCE.

➤ **Study of electrochemical active surface area (EAS) by ferrocyanide and ferricyanide redox using CV**

At the forward scan of CV, the potential is swept positively and ferrocyanide ($\text{Fe}(\text{CN})_6^{-4}$) is oxidised. The anodic current is presented as the electrode process in **Eq. 2**.



The electrode material forms as an oxidant, and the oxidation current increases to a peak. When ferrocyanide concentration at the electrode surface is consumed, the current will decay. At the scan control is changed to negative, the potential is still enough positive to oxidise ferrocyanide, so anodic current proceeds even though the potential is now scanning in the negative direction. When the electrode comes to be an enough strong reductant, ferricyanide, which has been forming adjoining to the electrode surface will be decreased by the electrode process in **Eq. 3**,



leading to a cathodic current peak and then it decays as ferricyanide in the solution adjoining to the electrode is depleted. The significant parameters attained from CV are the anodic and cathodic peak currents (i_{pa} and i_{pc}) and the anodic and cathodic peak potentials (E_{pa} and E_{pc}); all of these parameters can be obtained automatically by the CV. In order to study the electrochemical active surface area (EAS) of the electrode materials, the experimental EAS was calculated using the Randles-Sevcik equation as shown in **Eq. 4** [33].

$$i_p = (2.69 \times 10^5) n^{3/2} A D^{1/2} C v^{1/2} \quad (\text{Eq. 4})$$

where A is the electrode surface area (cm^2), D is the diffusion coefficient (cm^2/s), C is the concentration of the electroactive species in the bulk solution (mol/cm^3), v is the scan rate (V) and n is the number of electrons transfer in the half-cell reaction.

Therefore, i_p is proportional to C and proportional to $v^{1/2}$. In this work, the experimental EAS was calculated based on $n = 1$, $D = 0.667 \times 10^{-5} \text{ cm}^2/\text{s}$ [34] and $C = 1 \times 10^{-5} \text{ mol}/\text{cm}^3$.

2.4.2 Electrochemical impedance spectroscopy (EIS)

EIS is an advanced technique to identify various electrochemical activities, such as internal resistance and conductive layers of electrode materials used in MFC systems. A potentiostat instrument is used to conduct the simple EIS technique. The impedance spectra from EIS results can be programmed using this instrument in a wide frequency range, such as from 100 kHz to 1 mHz. For MFC studies 1 or 5 mHz should be enough as the lower frequency is limited in providing accurate information [2].

2.4.3 Fourier transform infrared spectroscopy (FTIR) analysis

FTIR is a dependable analytical technique in order to identify and study polymer and chemicals of electrode materials. When polymer material absorbs infrared light, regularly in the mid-infrared area, the resulting spectrum will be shown.

2.4.4 Brunauer Emmet and Teller (BET) measurement

The BET measurement is based on adsorption of gas on a surface. In determining the surface area and pore structure, adsorption of N_2 gas at -196°C is used and the isothermal equilibrium data is fitted using either Langmuir or BET equations [35, 36].

2.4.5 X-Ray Diffraction (XRD) analysis

XRD is a rapid analytical measurement primarily used for phase identification of a crystalline material or compound and can provide information on unit cell dimensions. The analysed material is finely ground, homogenised, and average bulk composition is determined.

2.4.6 Scanning electron microscopy (SEM)

SEM is a typical measurement for observing and studying the morphology of electrode materials. Scott et al. [37] used the SEM images of modified carbon anode materials to directly indicate properties such as roughness and porosity. Moreover,

Energy-Dispersive X-ray (EDX) spectroscopy, XRD and BET are also applied to study the surface and element composition [2].



Chapter 3

Materials and Methods

3.1 Chemicals and materials

3.1.1 Modification of granular activated carbon (GAC)

Manganese (II) sulfate monohydrate ($\text{MnSO}_4 \cdot \text{H}_2\text{O}$) was purchased from LOBA Chemie Pvt. Ltd. (Mumbai, India). 2-Propanol was procured from Fisher Scientific (UK). Potassium permanganate (KMnO_4) was obtained from Ajax Finechem Pty. Ltd. (Sydney, Australia). Coal and wood (coconut shell)-based Granular activated carbon (GAC) mesh size 8x30 were obtained from C. Gigantic Carbon Co., Ltd (Thailand) and used as the carbon substrate for heat treatment and precipitation.

3.1.2 Modification of stainless steel (SS) mesh

Pyrrrole was purchased from Acros Organics (Geel, Belgium). Potassium ferrocyanide ($\text{K}_4\text{Fe}(\text{CN})_6$) and Potassium nitrate (KNO_3) were obtained from Ajax Finechem Pty. Ltd. (Sydney, Australia). Manganese (II) sulfate monohydrate ($\text{MnSO}_4 \cdot \text{H}_2\text{O}$) and Sodium sulfate (Na_2SO_4), were procured from LOBA Chemie Pvt. Ltd. (Mumbai, India). Acetone and Sulfuric acid (H_2SO_4) were purchased from Merck KGaA (Darmstadt, Germany). Ethanol was procured from Liquor Distillery Organization (Excise Department, Thailand). All the other reagents were of AR grade. All solutions were prepared using deionised water. Stainless steel gauze (20 mesh plain-woven from 0.27mm dia wire), type 316 and stainless steel gauze (20 mesh plain-woven from 0.30mm dia wire), type 304 were used as the metal substrate and auxiliary for electropolymerisation and electrodeposition.

3.2 Experimental

3.2.1 Modification of GAC

3.2.1.1 Preparation of GAC

GAC (wood-based) and GAC (coal-based) samples were cleaned ultrasonically with deionised water to remove all dust and fines, oven-dried for 6 hours at 80 °C and stored in sealed containers.

3.2.1.2 Heat treatment of GAC

Approximately 0.1 g of GAC sample was placed in pulse sample cell within chemisorption analyzer-BEL CAT-B (BET single point measurement). For as-received of GAC; first, sample was heated from the room temperature (25 °C) to 100 °C for 20 minutes, and kept sample at this temperature for 20 minutes under helium flow with flow rate of 50 sccm and then sample was performed using BET measurement for surface area analysis. For as-prepared GAC, the same sample was used for heat treatment under nitrogen flow in reactor tube within Nabertherm high temperature tube furnace (controller P320) at higher temperature of 200 °C, 400 °C, 600 °C, 800 °C and 1,000 °C by heat from the room temperature (25 °C) to each temperature for 20 minutes, and sample kept at each temperature for 20 minutes with a flow rate of 100 sccm and then performed BET measurement for surface area analysis. Both of GAC samples were weighed before and after heat treatment.

3.2.1.3 Precipitation of MnO₂ on GAC

MnO₂ was precipitated onto GAC, GAC under 600 °C and GAC under 800 °C substrates following Pan, N., et al. method [8]. 1 g GAC and 0.5911 g MnSO₄·H₂O were added into 60 ml 2-propanol and sonicated for 10 min. Aqueous solution of KMnO₄ (0.3909 g KMnO₄/12 ml H₂O) was rapidly poured into the mixture immediately and refluxed at 87 °C under stirring 30 min. After that, the sample was cleaned repeatedly with deionised water and dried in oven at 105 °C for 1 hour.

3.2.2 Modification of SS

3.2.2.1 Preparation of SS mesh

SS mesh was polished with the 300 grade sand paper, cleaned ultrasonically, degreased in acetone and ethanol successively (each for 2 hours). After that, pretreated SS mesh was rinsed with deionised water for several times and dried at the room temperature (25 °C) for 24 hours. All electrodes were weighed before and after polymerisation.

3.2.2.2 Electropolymerisation of PPy-coated SS mesh

PPy was coated on 15x20-mm SS mesh via electropolymerisation using an autolab PGSTAT 204 potentiostat/galvanostat (Metrohm) with three-electrode electrochemical system. Ag/AgCl electrode was used as a reference electrode, Both of SS types were used as a working electrode, and another type was used as a counter electrode.

PPy films were synthesised in a N₂-saturated solution containing 0.1 M Pyrrole and 5 mM Na₂SO₄ by CV using an autolab PGSTAT 204 potentiostat/galvanostat (Metrohm). The potential range was swept between -0.75 to 1.5 V for 50 cycles (thinner layer) and 100 cycles (thicker layer) using various scan rates of 50, 100, 200, and 400 mV s⁻¹. And then the PPy-coated SS electrodes were rinsed with deionised water several times and dried at the room temperature for 24 hours.

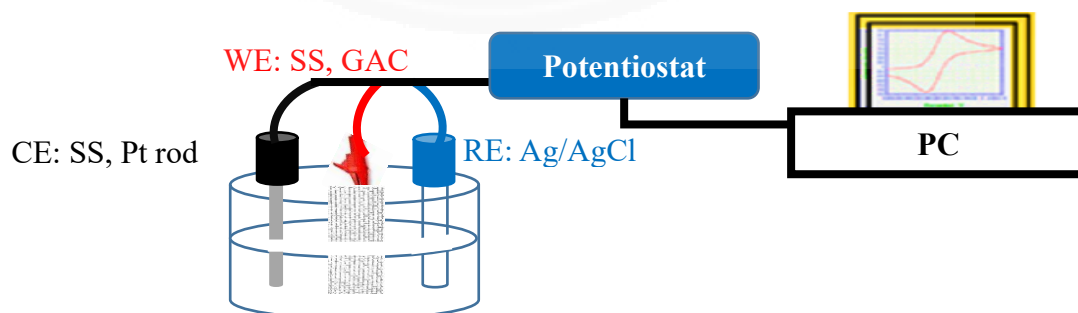


Fig. 3.1 The set-up of electropolymerisation, electrodeposition and EAS analysis.

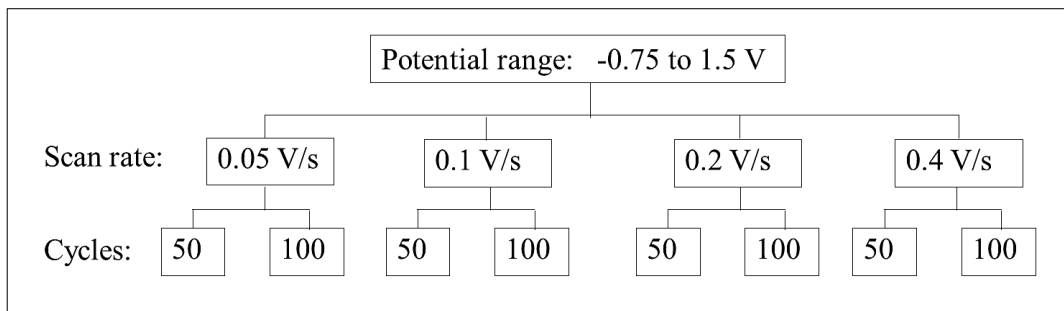


Fig. 3.2 Diagram of electropolymerisation.

3.2.2.3 Electrodeposition of MnO₂ on PPy-coated SS mesh

The MnO₂ nanostructured film was electrodeposited under the room temperature following Suhasini's method [3] CV method was used to electrodeposit MnO₂ on electrode materials using an autolab PGSTAT 204 potentiostat/galvanostat (Metrohm) with three electrode system. CV was applying two different potential regions. The potential range was swept between 0 to 1.6 V for 240 cycles using a scan rate of 200 mV s⁻¹. The bare SS mesh, PPy-coated SS 304 at 50 and 100 mV s⁻¹ under 50 cycles and PPy-coated SS 316 at 100 and 200 mV s⁻¹ under 50 cycles were used working electrodes. Ag/AgCl electrode was used as reference electrode. Another type of SS working electrode was used as a counter electrode. The electrolyte was 1 M MnSO₄ in 0.1 M H₂SO₄ prepared using deionised water. After electrodeposition, the electrode material was separated from the cell, rinsed with deionised water and dried at the room temperature before being stored in the desiccator.

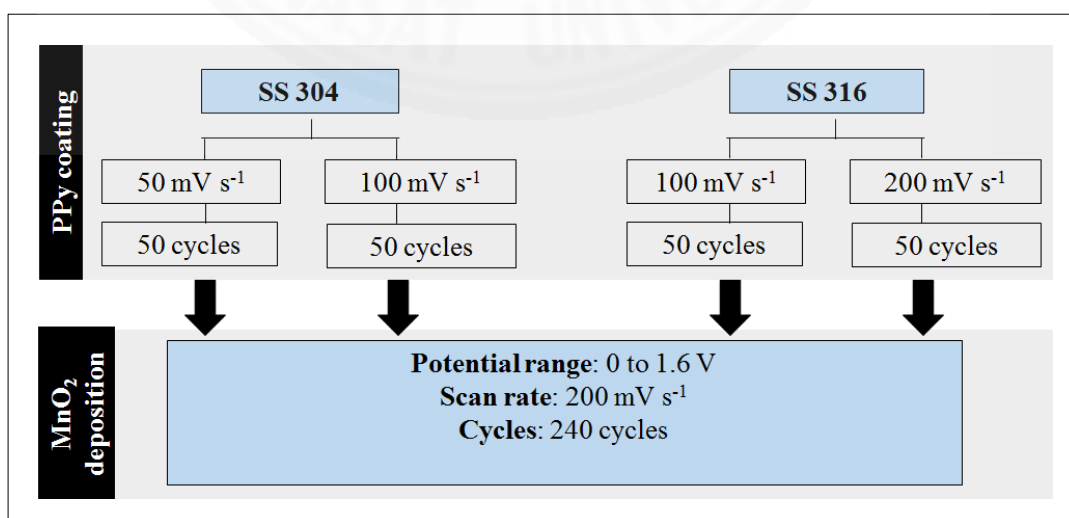


Fig. 3.3 Diagram of electrodeposition.

3.3 Characterisation

3.3.1 BET analysis

Both of GAC samples were measured by multipoint surface area analyser (Quantachrome Instruments, Model Nova1000e series). The specific surface (S_{BET}) and micropore volume were measured using the traditional method of Brunauer Emmet and Teller or BET [35].

3.3.2 FTIR analysis

The PPy film was scraped out from SS mesh to determine its functional groups. Infrared spectrum was recorded as a function of wavenumber on a Nicolet iS5 FTIR spectrometer. The sample was analysed in the transmittance mode within the wavenumber range of 4,000–400 cm^{-1} at resolution of 4 cm^{-1} and 32 cycles.

3.3.3 SEM analysis

The surfaces of bare SS, MnO_2/SS , PPy-coated SS, MnO_2/PPy -coated SS, GAC and MnO_2/GAC were investigated using FE.SEM (Hitachi SU5000) and FE.SEM (Hitachi SU8030). Vibration control measures for the stage and chamber, and optimisation of the optical system contribute to the high resolution system performance of 6.5 nm at secondary electron (SE) Image and high acceleration voltage (V_{acc}) of 5kV for GAC and 15kV for SS. The average elemental composition of electrode materials was measured by means of an EDX attached to the FE.SEM (Hitachi S3400).

3.3.4 X-Ray Diffraction (XRD) analysis

XRD analysis of the electrode materials was carried out using PANalytical (Model X'Pert PRO). After MnO_2 precipitation onto GAC sample, a dried sample of MnO_2 sediment and both of untreated GAC samples were grinded and tested at 40kV and 30mA. The spectra were analysed using MDI Jade 6.5 diffraction software.

3.3.5 CV analysis

To study the electrochemical active surface area (EAS) of electrode materials, CV was measured by an autolab PGSTAT 302N potentiostat/galvanostat (Metrohm) in an electrochemical cell. For electrochemical activities, the

electrochemical cell contained samples on SS, MnO₂/SS, PPy-coated SS, MnO₂/PPy-coated SS, GAC and MnO₂/GAC as working electrode, a platinum rod as counter electrode and a Ag/AgCl as reference electrode. SS 304 (80×40 mesh) basket was used as the holder for CV testing of GAC. In a mixture of 10 mM K₄Fe(CN)₆ and 1 M KNO₃, the potential range was swept between -0.2 to 0.85 V (for SS) and 0 to 1.3 V (for GAC) for 5 cycles using the scan rates of 25, 50, 100, 200 mV s⁻¹. And then, the electrode materials were rinsed with deionised water several times and dried at the room temperature before being stored into the desiccator.

3.3.6 EIS analysis

EIS was measured by an autolab PGSTAT 302N potentiostat/galvanostat (Metrohm) in an electrochemical cell. The EIS measurements were carried out using SS, MnO₂/SS, PPy-coated SS MnO₂/PPy-coated SS, GAC and MnO₂/GAC electrode materials. SS 304 (80×40 mesh) basket was used as the holder for EIS testing of GAC. Impedance results were reported in the frequency range of 100 kHz - 100 mHz for SS and 50 kHz–1 Hz for GAC. The voltage amplitude was 10 mV with regard to the open circuit potential. The impedance spectra was analysed using Nova 2.0.2 software. The electrical equivalent circuit simulated to the experimental data was observed.

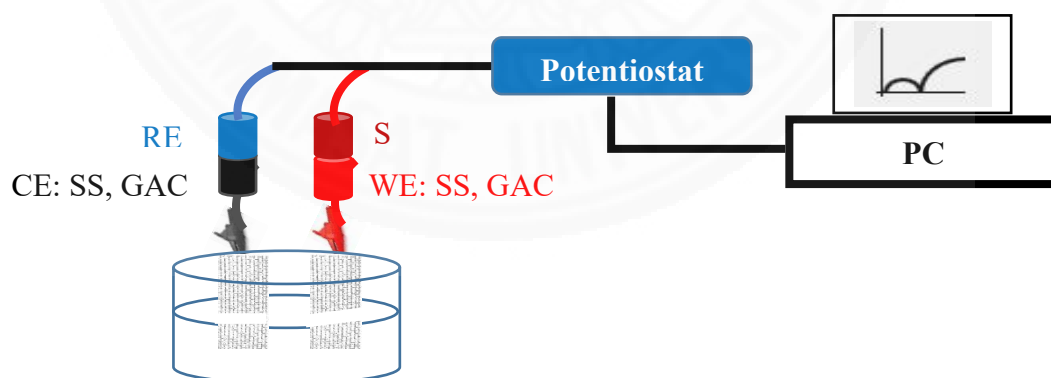


Fig. 3.4 The set-up of EIS analysis.

Chapter 4

Results and Discussion

4.1 Modification of GAC

4.1.1 Effect of heat treatment on morphology

The SEM images of GAC and heated GAC under the 500 and 10k magnifications were shown in **Fig 4.1-4.4**. As can be seen, GAC has an irregular porous surfaces [38, 39]. BET results from **Table 4.1** show that after heat treatment, the surface area and pore volume of GAC had been changed. The micropore volume of GAC increased with increasing temperatures. They exhibited a maximum value at 600 °C for GAC (coal-based) and 800 °C for GAC (wood-based). It indicated that heated GAC represents a better micropore volume of electrode materials.

Fig. 4.5 shows the effect of heat treatment under N₂ flow on the change in the specific area of GAC. Heat treatment at various temperature of 200 °C, 400 °C, 600 °C, 800 °C and 1000 °C affected specific surface area, when compared to the untreated GAC. For heat treatment of GAC (wood-based); when temperatures increased step by step, the surface area is also enhanced gradually by 12.47 m²/g at 200 °C, 17.16 m²/g at 400 °C, 17.30 m²/g at 600 °C, and 16.98 m²/g at 800 °C. After that the specific surface area at 1,000 °C decreased to the value that was less than the specific area of the untreated GAC. For GAC (coal-based); when temperatures increased, first, the specific surface area at 200 °C was less than the untreated GAC, then improved continuously by increased approximately 3.30 m²/g at 400 °C, 16.45 m²/g at 600 °C and reached to 18.19 m²/g at 800 °C before decreased to 3.06 m²/g at 1000 °C.

These results presented that heat treatment plays an important role in increasing of the specific surface area and pore volume of GAC electrode materials. The best performances of heat treatment of GAC electrode materials was 600 °C and 800 °C. Therefore, the electrode modification to prepare large quantity of BET and Langmuir surface area and pore volume of GAC could be achieved using heat treatment at 600 °C and 800 °C for MnO₂ precipitation method.

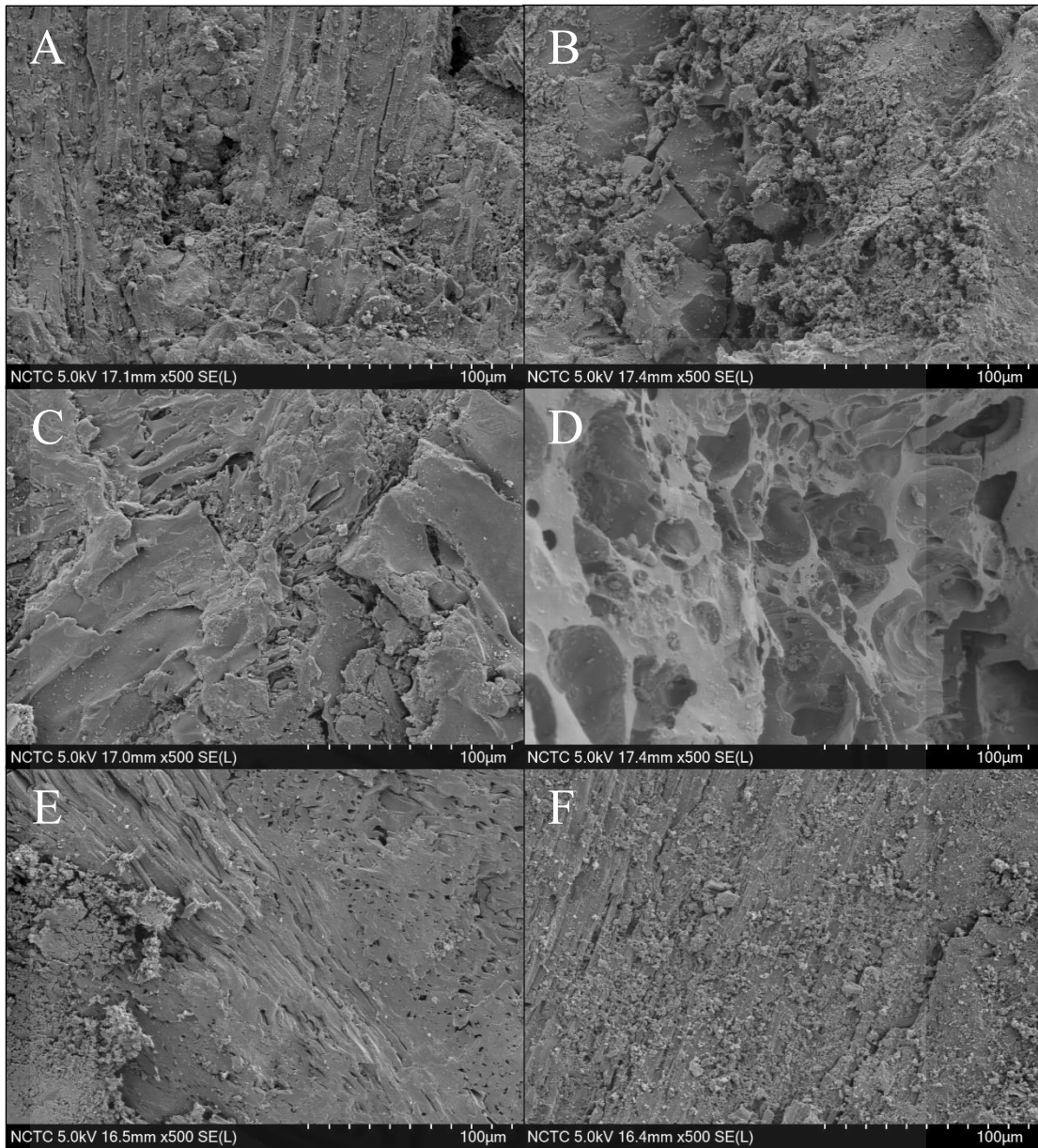


Fig. 4.1 SEM images GAC (coal-based) at 500 magnification at (A) as-received GAC (B) 200 °C (C) 400 °C (D) 600 °C (E) 800 °C and (F) 1,000 °C of heat treatment.

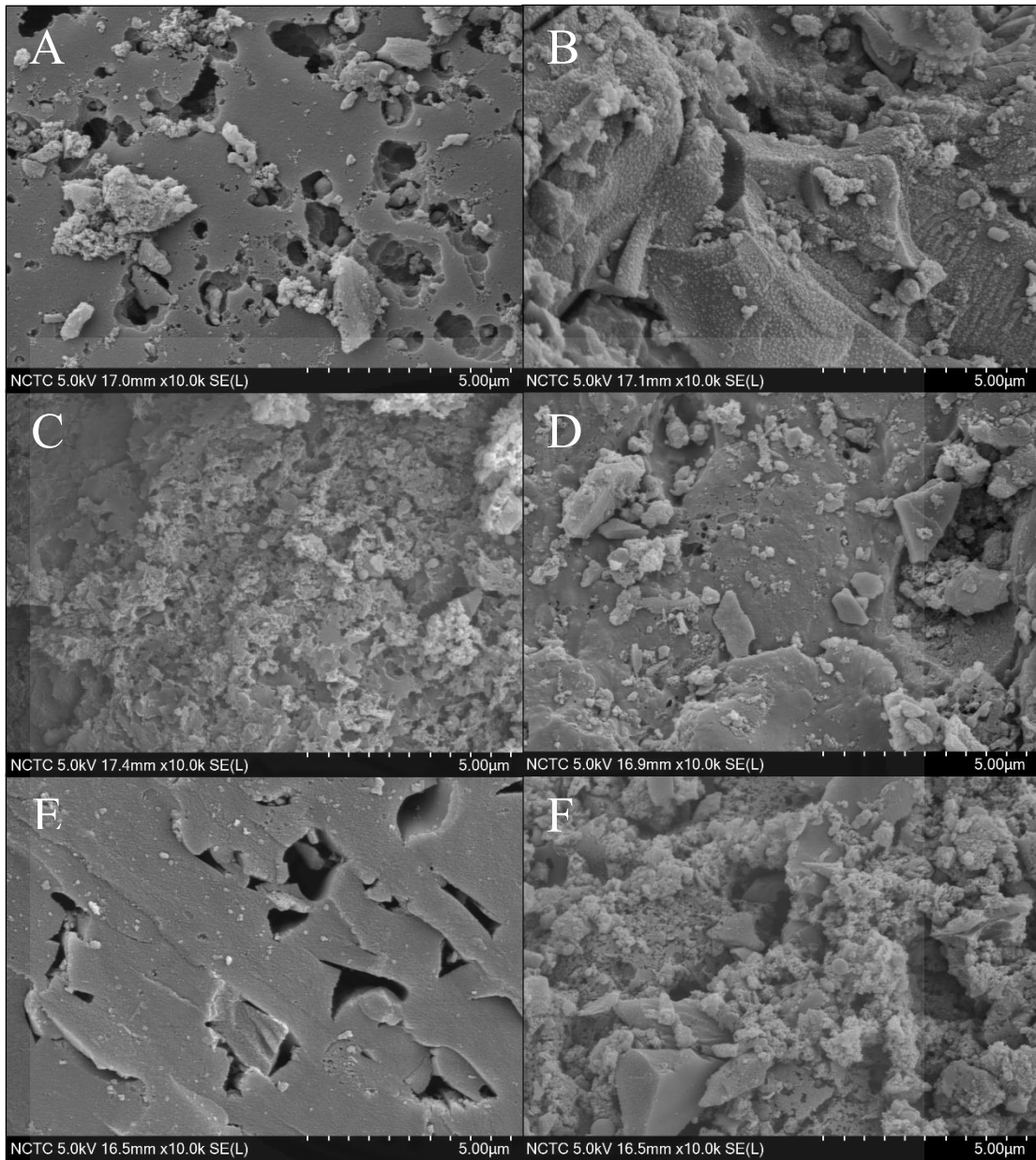


Fig. 4.2 SEM images GAC (coal-based) at 10k magnification at (A) as-received GAC (B) 200 °C (C) 400 °C (D) 600 °C (E) 800 °C and (F) 1,000 °C of heat treatment.

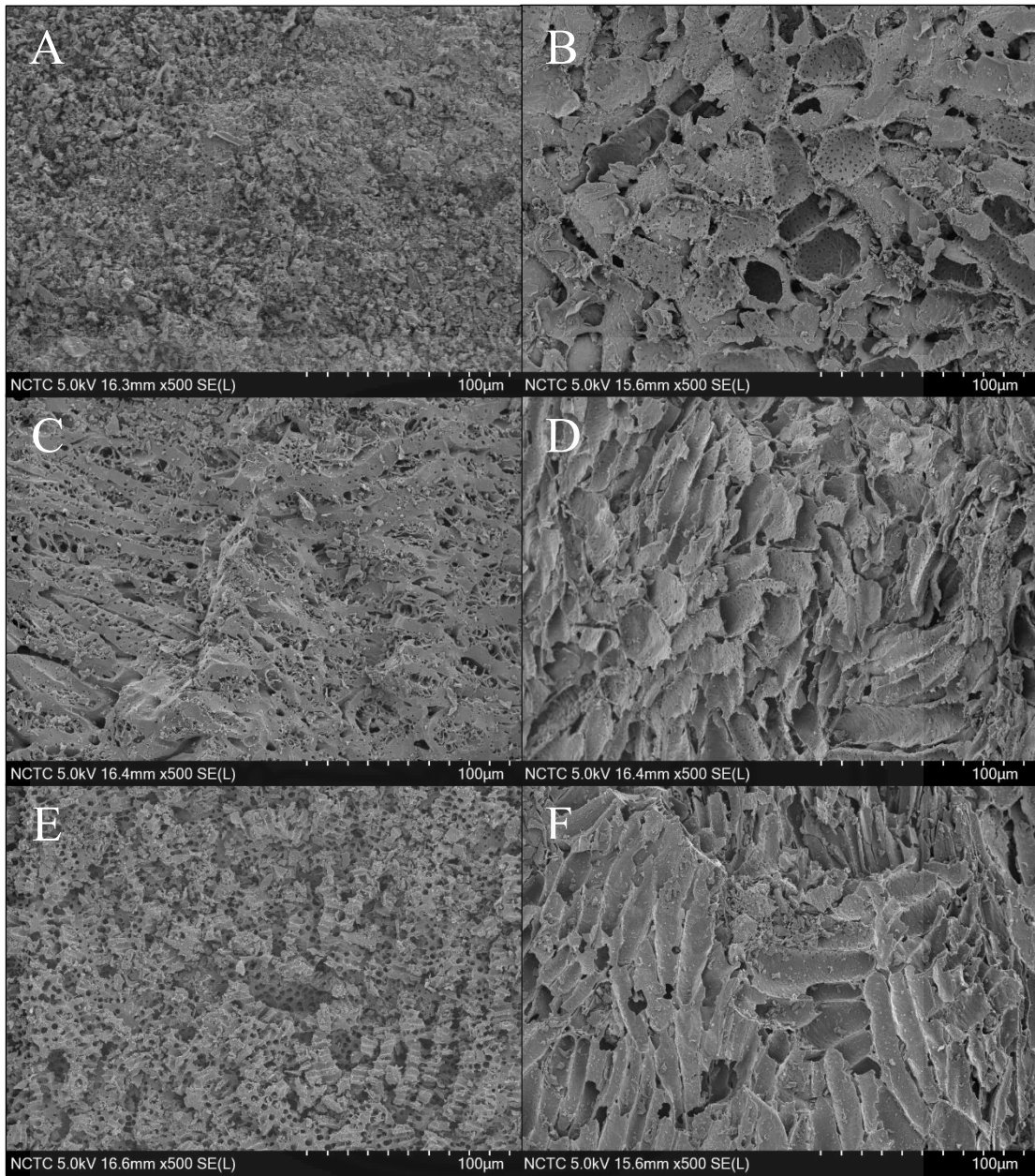


Fig. 4.3 SEM images GAC (wood-based) at 500 magnification at (A) as-received GAC (B) 200 °C (C) 400 °C (D) 600 °C (E) 800 °C and (F) 1,000 °C of heat treatment.

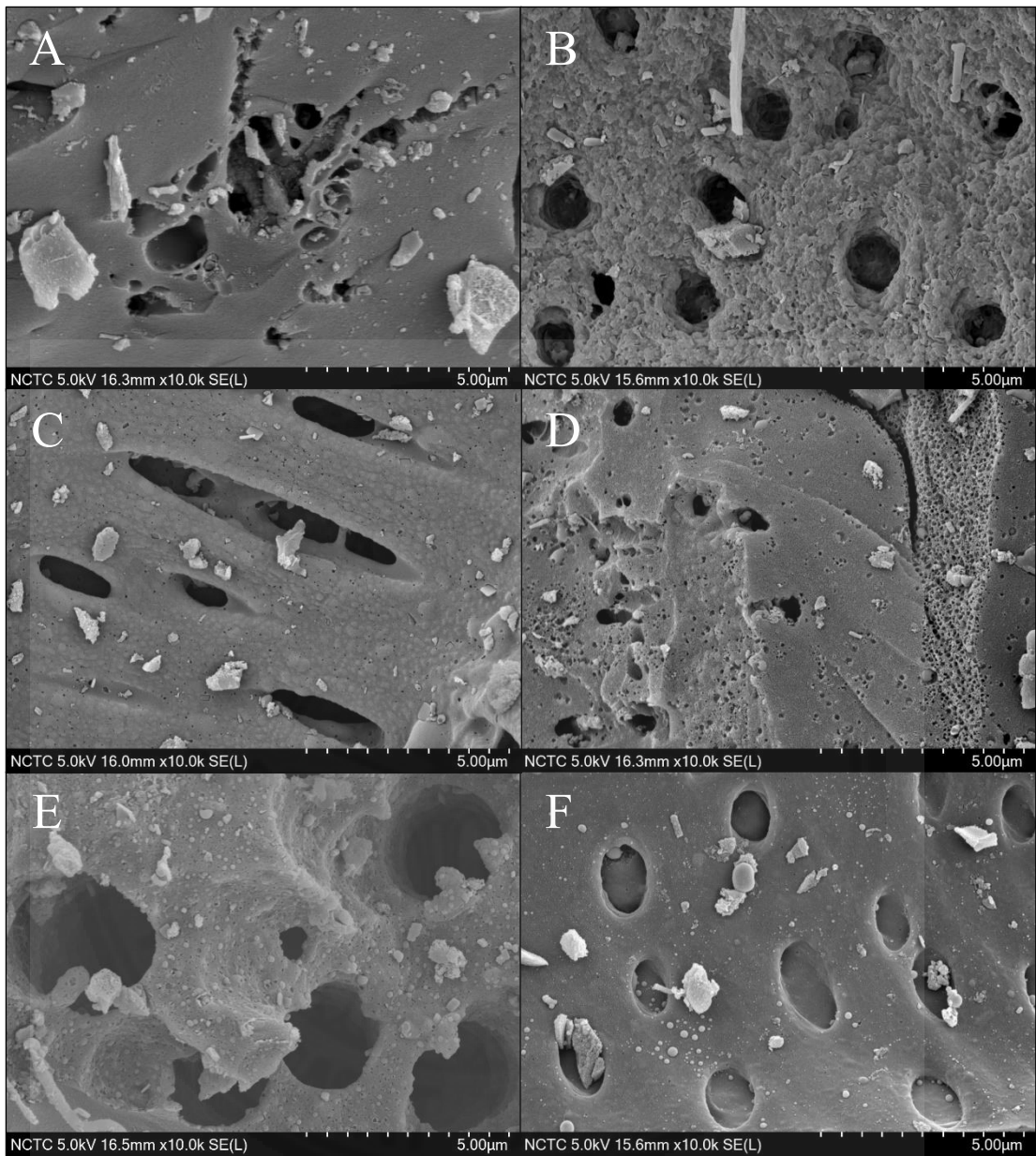


Fig. 4.4 SEM images GAC (wood-based) at 10k magnification at (A) as-received GAC (B) 200 °C (C) 400 °C (D) 600 °C (E) 800 °C and (F) 1,000 °C of heat treatment.

Table 4.1 Surface area and micropore structure parameters of GAC samples.

Heat treatment of GAC samples		Surface area (m ² /g)			Micropore volume (cc/g)	Pore width (Å)
		BET _{singlepoint} before heat	BET _{singlepoint} after heat	Langmuir		
GAC (coal-based)	200 °C	611.88	608.02	1,421	0.485	5.732
	400 °C	559.81	563.12	1,415	0.506	5.480
	600 °C	548.75	565.19	1,064	0.557	5.480
	800 °C	592.20	610.39	1,969	0.547	5.732
	1,000 °C	530.39	533.44	1,054	0.359	5.480
GAC (wood-based)	200 °C	788.80	801.27	1,652	0.506	5.732
	400 °C	779.89	797.05	1,394	0.471	5.732
	600 °C	709.06	726.37	1,437	0.550	5.480
	800 °C	717.78	734.75	1,744	0.587	5.480
	1,000 °C	758.53	744.64	1,679	0.581	5.480

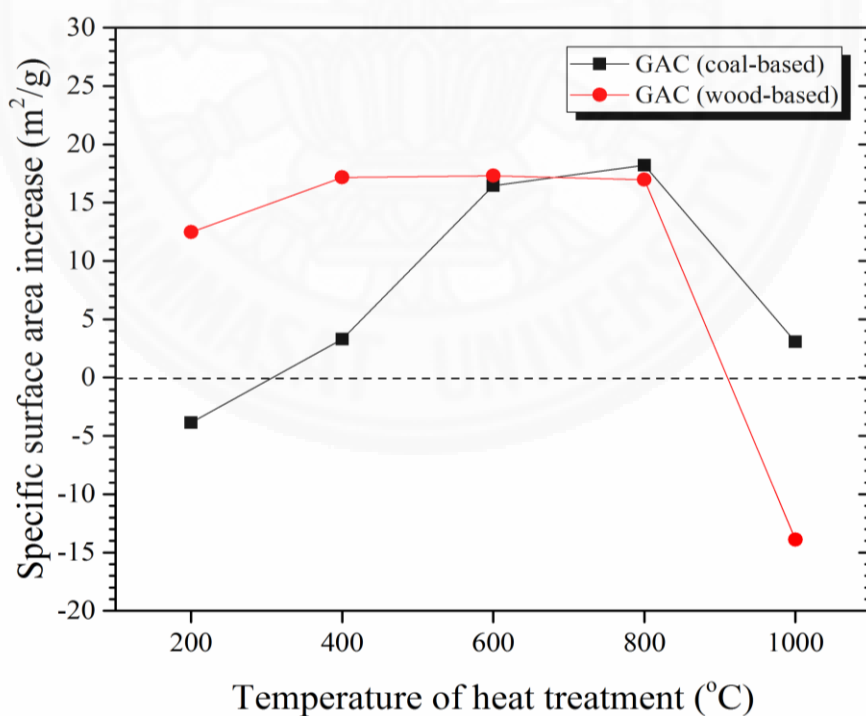


Fig. 4.5 Change in specific surface area (BET_{single point}) of GAC after heat treatment under N₂ flow.

4.1.2 Effect of MnO₂ precipitation on morphology

Fig. 4.6 and **4.7** shows the SEM images of various MnO₂/GAC electrodes. The MnO₂ images (as shown in **Fig. 4.6B, 4.6D, 4.6F, 4.7D** and **4.7F**) revealed needle-like morphologies [8], implying that MnO₂ were coated onto the GAC surfaces in GAC(coal-based), heated GAC (coal-based) and heated GAC (wood-based). **Fig. 4.7B** shows a granular-like MnO₂ was attached to the surfaces of GAC (wood-based).

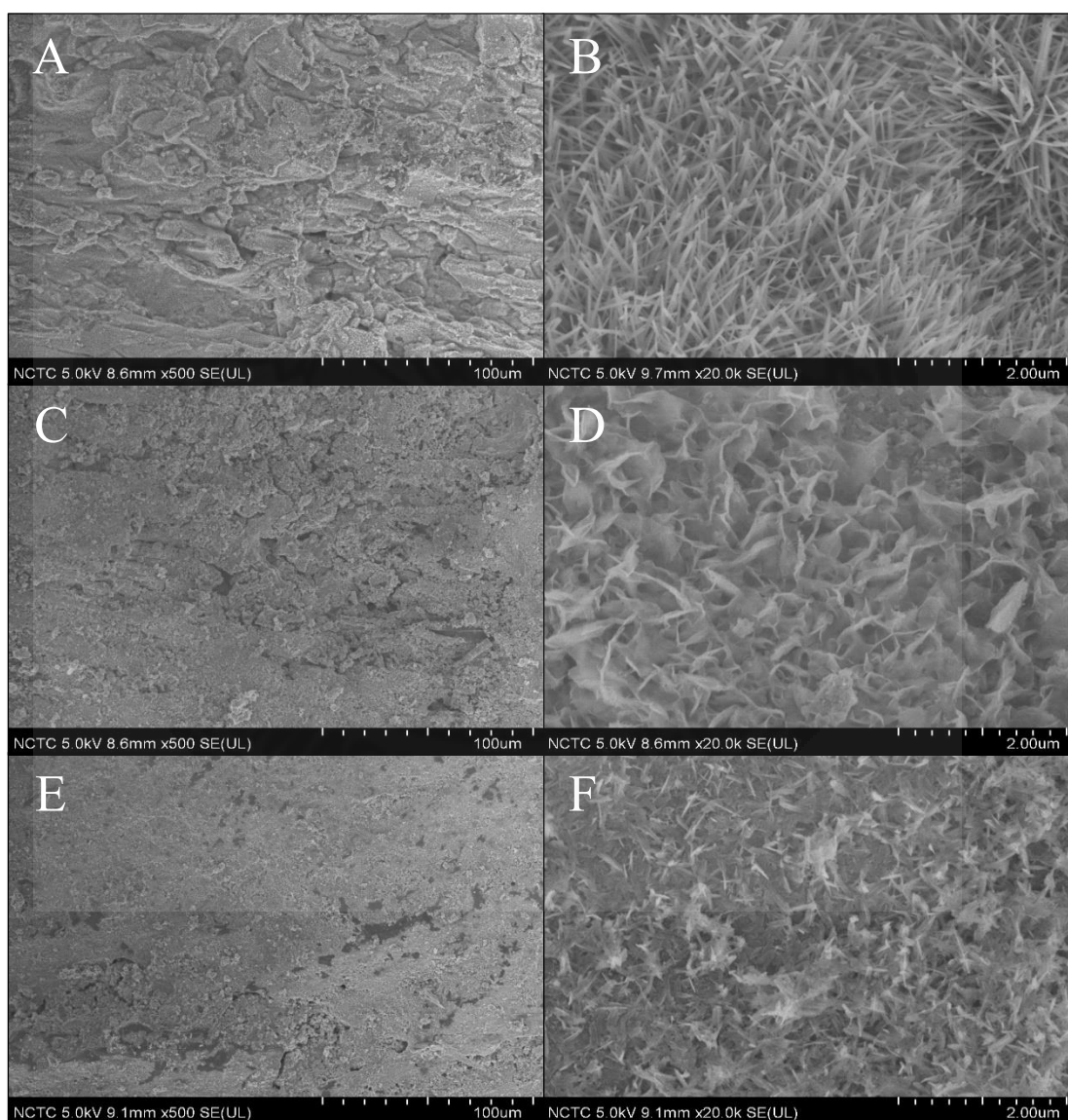


Fig. 4.6 SEM images of MnO₂/GAC (coal-based) at (A) 500 and (B) 20k magnification, MnO₂/GAC (coal-based) under 600 °C at (C) 500 and (D) 20k magnification, and MnO₂/GAC (coal-based) under 800 °C at (E) 500 and (F) 20k magnification.

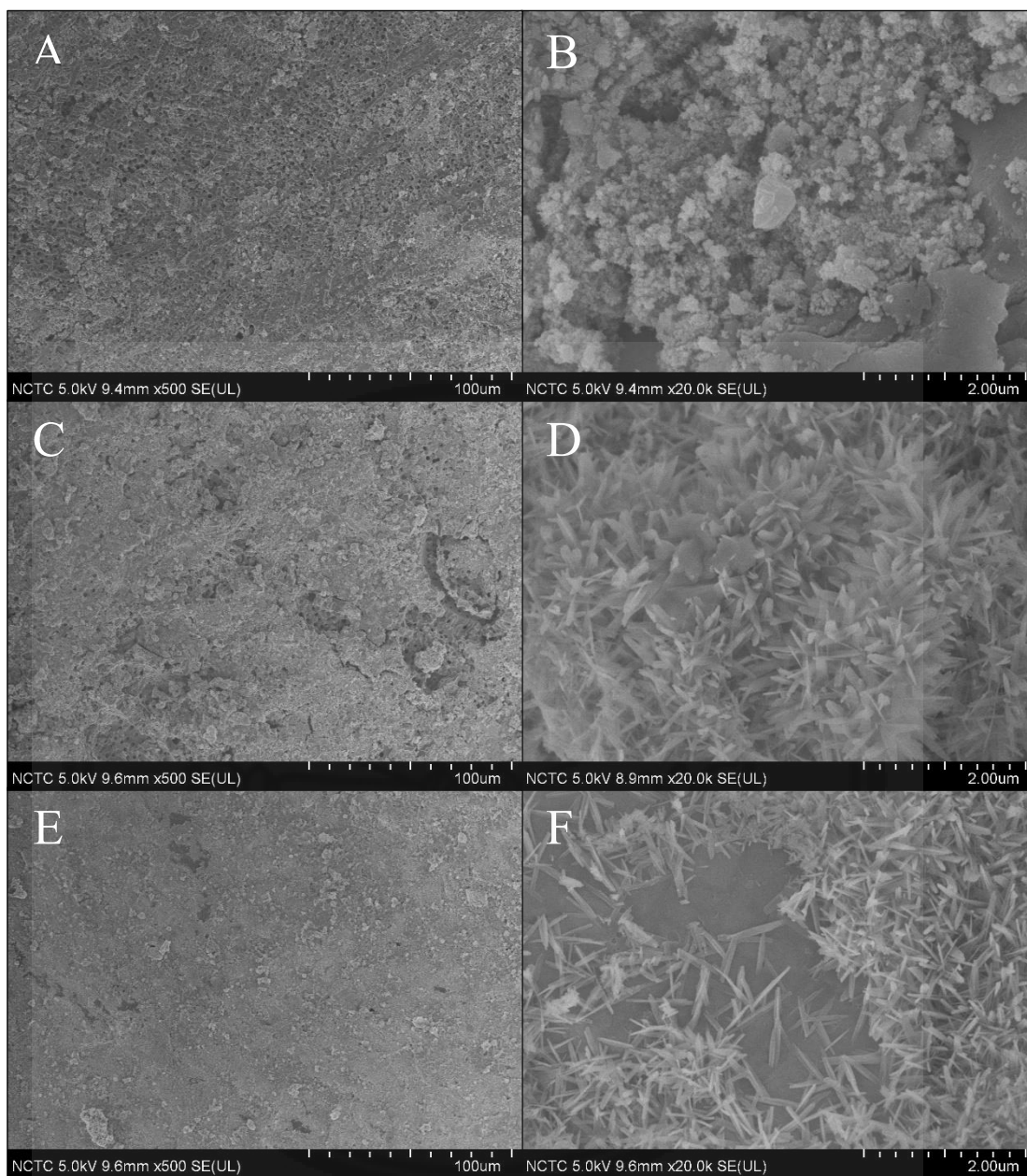


Fig. 4.7 SEM images of MnO₂/GAC (wood-based) at (A) 500 and (B) 20k magnification, MnO₂/GAC(wood-based) under 600 °C at (C) 500 and (D) 20k magnification, and MnO₂/GAC(wood-based) under 800 °C at (E) 500 and (F) 20k magnification.

4.1.3 XRD and EDX results

The X-ray diffraction of MnO₂ sediment is shown in **Fig. 4.8**. It confirms that there is the precipitation of MnO₂ on both GAC and heated GAC. The local elemental composition of various MnO₂ precipitated on GAC and heated GAC surfaces was analysed (**Fig. 4.9**) by EDX. This confirms the existence of MnO₂ on the coated electrode surface by precipitation. **Table 4.2A** and **4.2B** show percentage of MnO₂ coating at different electrode materials. They show that Mn elemental decreased with increasing temperatures.

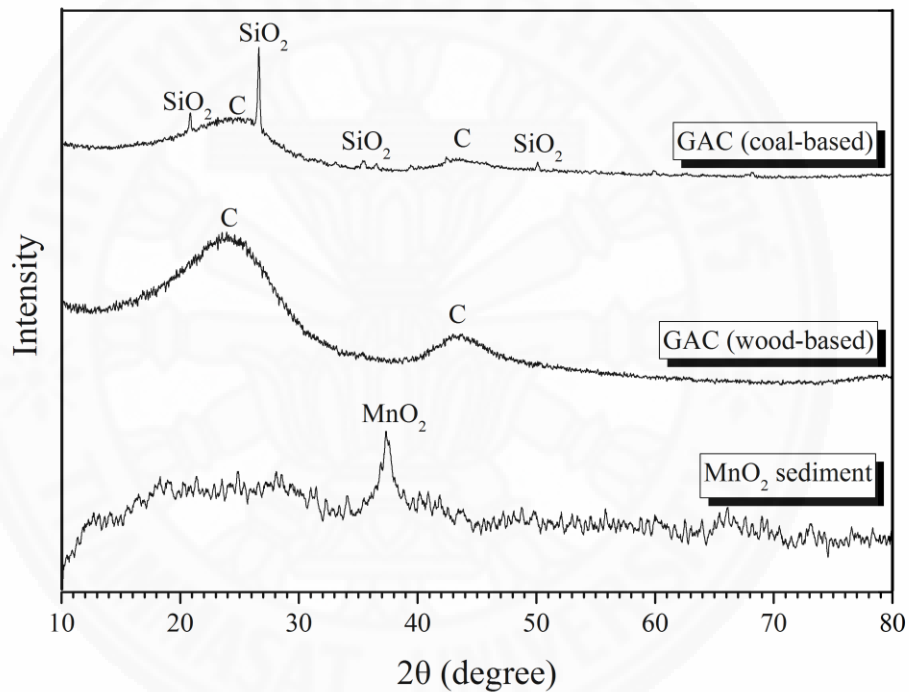


Fig. 4.8 XRD spectra of MnO₂ sediment and uncoated GAC samples.

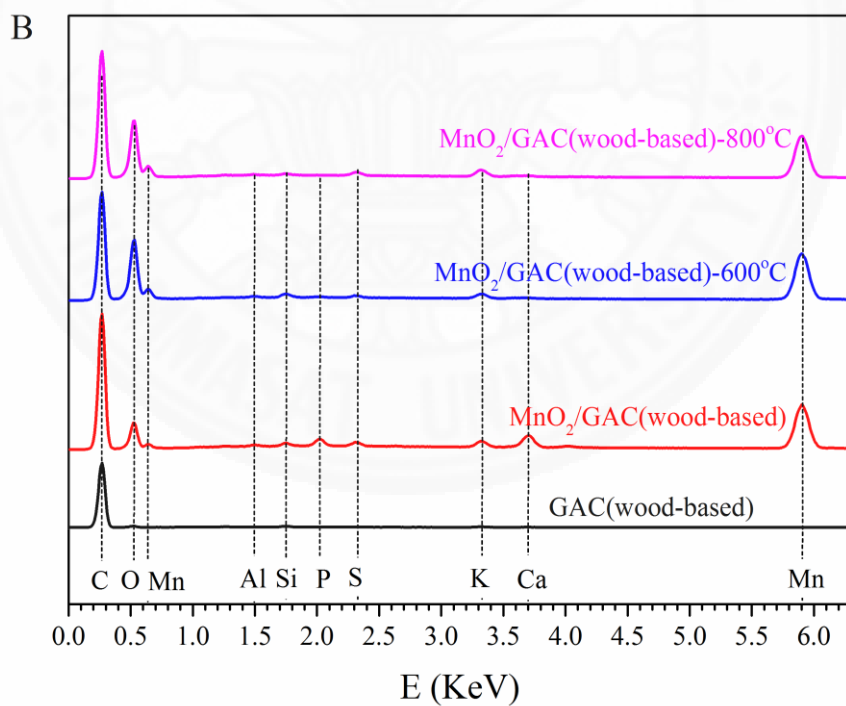
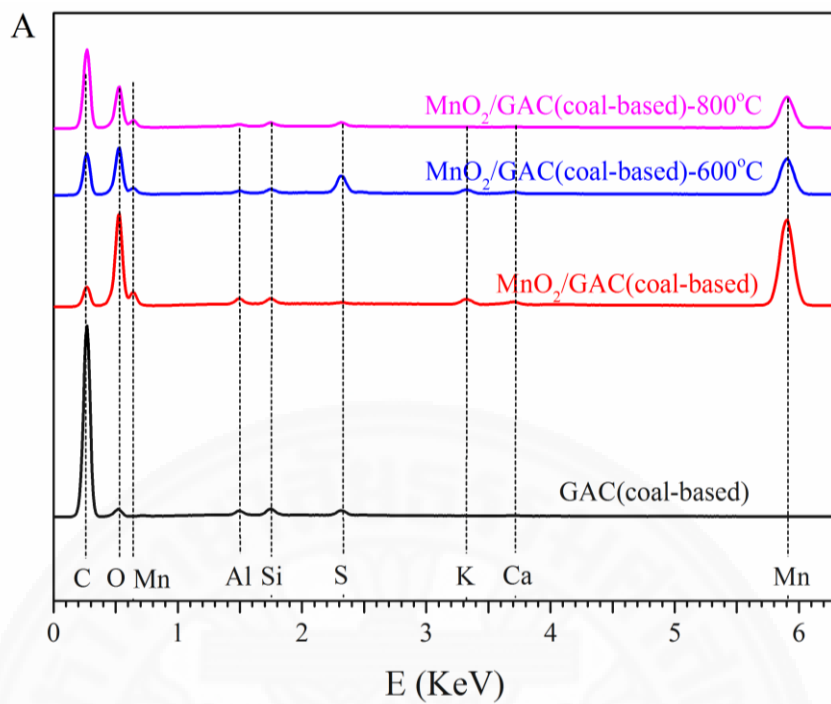


Fig. 4.9 EDX analysis of MnO₂ electrodeposited on different (A) GAC (coal-based) and (B) GAC (wood-based) electrode materials.

Table 4.2A Elemental composition of various GAC (coal-based) electrode materials corresponding to EDX spectrum.

Electrode materials	Average elemental composition (% wt)								
	C	O	Al	Si	P	S	K	Ca	Mn
GAC (coal-based)	87.32	9.93	0.69	1.04	0	1.04	0	0	0
GAC (coal-based) - 600°C	76.72	10.34	5.90	6.02	0	0.44	0	0.58	0
GAC (coal-based) - 800°C	68.15	15.21	5.86	9.86	0	0.34	0	0.58	0
MnO ₂ /GAC (coal-based)	16.64	31.79	1.29	1.19	0	0	1.08	0.62	47.40
MnO ₂ /GAC (coal-based) - 600°C	25.81	35.07	2.09	5.95	0	3.45	0.87	0.47	26.33
MnO ₂ /GAC (coal-based) - 800°C	47.21	31.93	0.37	0.67	0	1.48	0.33	0.11	17.93

Table 4.2B Elemental composition of various GAC (wood-based) electrode materials corresponding to EDX spectrum.

Electrode materials	Average elemental composition (%wt)								
	C	O	Al	Si	P	S	K	Ca	Mn
GAC (wood-based)	92.35	7.65	0	0	0	0	0	0	0
GAC (wood-based) - 600°C	85.60	13.47	0	0.44	0	0	0.48	0	0
GAC (wood-based) - 800°C	85.78	13.31	0	0.53	0	0	0.37	0	0
MnO ₂ /GAC (wood-based)	50.16	23.09	0.28	0.33	1.18	0.48	0.89	2.37	21.24
MnO ₂ /GAC (wood-based) - 600°C	53.47	26.88	0.19	0.47	0.15	0.23	0.56	0.15	17.93
MnO ₂ /GAC (wood-based) - 800°C	50.49	30.60	0	0.21	0	1.75	0.91	0.22	15.84

4.1.4 EAS of GAC electrodes

The experimental electrochemical active surface area (EAS) was calculated using the Randles-Sevcik equation (**Eq. 4**) in chapter 2 [40]. The value $i_p/v^{1/2}$ was the slope obtained from the graph plotted between the peak currents (extracted from **Fig. 4.10**) and the square root of the scan rates as shown in **Fig. 4.11**. The linear relationship observed between the peak current and the square root of the potential scan rate illustrates that the electrochemical system had not been adversely affected by the existence of MnO₂ metal oxide.

The peak currents gained from CV ranged from 0.06 to 0.12 A with the K₄Fe(CN)₆ solution. The EAS values varied from 1,609.79 to 10,079.16 cm²/g (as shown in **Table 4.3A** and **4.3B**). The untreated GAC showed that without treatment the surface of this material had little activity toward electron transfer with the K₄Fe(CN)₆ solution. Following modification with heat treatment, the EAS of heated GAC increased to 65 – 282%. Moreover, modifying with heat treatment and MnO₂ precipitation resulted in the active surface area increasing by 78 – 526% compared to the untreated GAC. Specifically, MnO₂/GAC (wood-based) under 600 °C and MnO₂/GAC (coal-based) exhibited highest EAS values of 10,080 (± 90) and 9,740 (± 3,030) cm²/g respectively. The heating method could reduce O/C ratio in carbon which caused the active surface area increasing [25]. However, the majority of oxygen functionalities on a carbon surface can be decomposed at 800 - 1000 °C of heat treatment [25] so the EAS value of MnO₂/GAC (coal-based) and MnO₂/GAC (wood-based) at 800 °C decreased with decreasing Mn composition at 800 °C as in EDX results because MnO₂ particles cannot attached on the GAC surfaces due to the lack of oxygen.

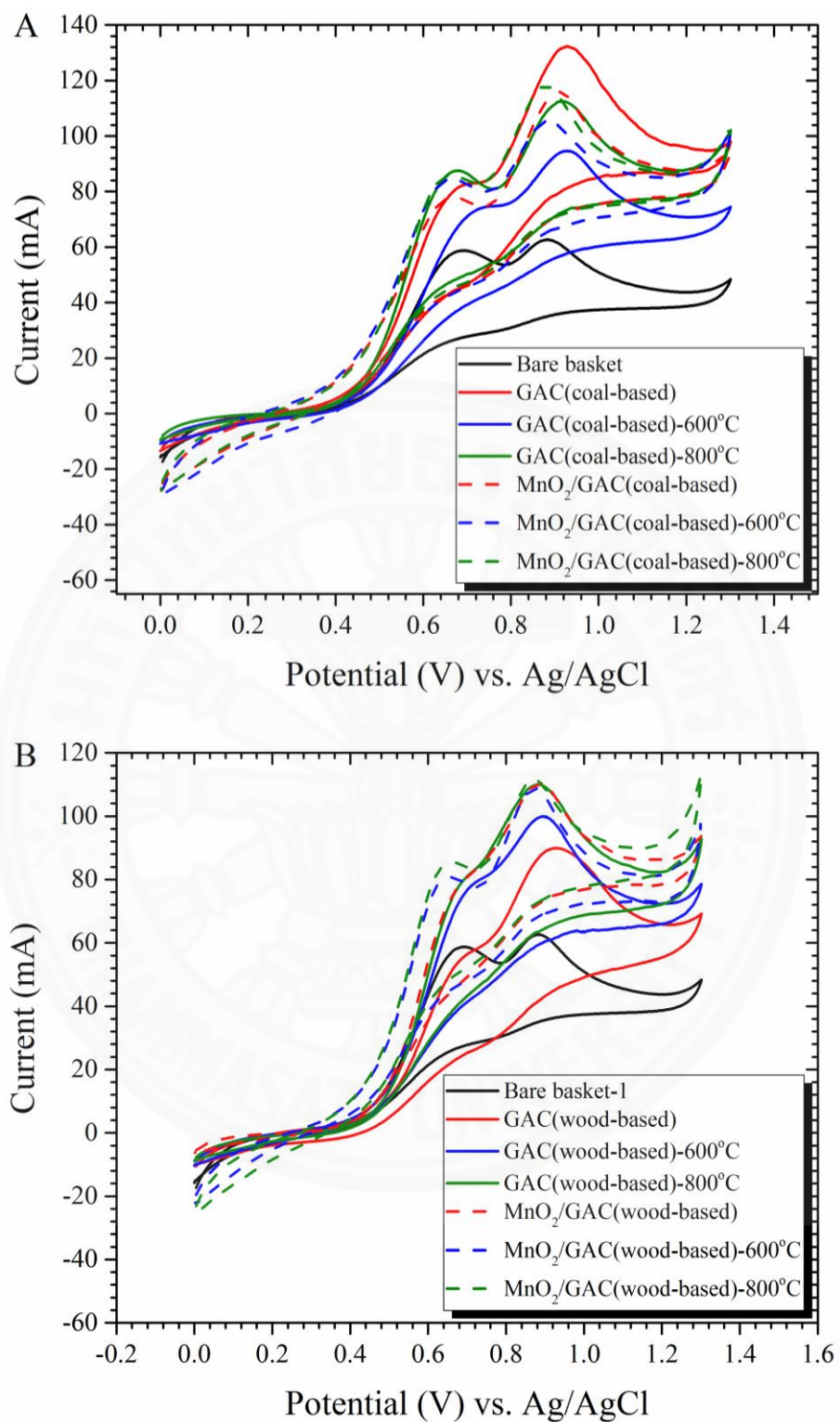


Fig. 4.10 CV of 10 mM $K_4Fe(CN)_6$ in 1.0 M KNO_3 solution recorded at various (A) GAC (coal-based) and (B) GAC (wood-based) electrode materials at the same potential scan rate of 25 $mV s^{-1}$.

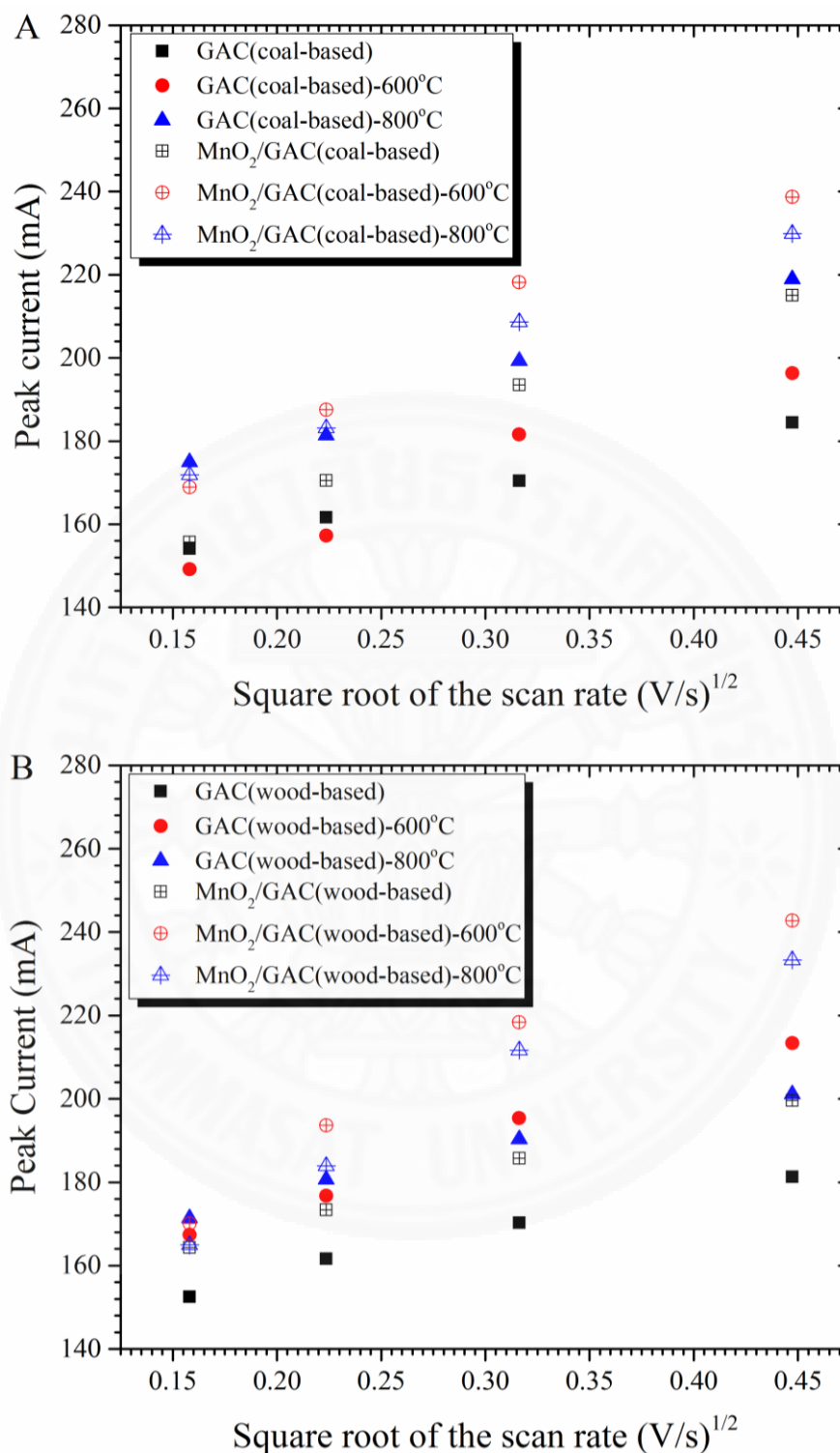


Fig. 4.11 Graphs plotted between the peak currents and square root of the scan rates according to the Randles-Sevcik equation. The peak currents were recorded on various (A) GAC (coal-based) and (B) GAC (wood-based) electrode materials.

Table 4.3A The active electrode surface area (A) of GAC (coal-based) electrode materials calculated from the Randle-Sevcik equation.

Electrode materials	Active surface area (cm²) per 1 g of geometric surface area
GAC (coal-based)	2,270 ± 878
GAC (coal-based) under 600 °C	3,810 ± 1,731
GAC (coal-based) under 800 °C	5,151 ± 2,977
MnO ₂ /GAC (coal-based)	9,740 ± 3,030
MnO ₂ /GAC (coal-based) under 600 °C	8,521 ± 1,779
MnO ₂ /GAC (coal-based) under 800 °C	6,521 ± 960

Table 4.3B The active electrode surface area (A) GAC (wood-based) electrode materials calculated from the Randle-Sevcik equation.

Electrode materials	Active surface area (cm²) per 1 g of geometric surface area
GAC (wood-based)	1,610 ± 13
GAC (wood-based) under 600 °C	6,150 ± 932
GAC (wood-based) under 800 °C	2,661 ± 614
MnO ₂ /GAC (wood-based)	2,877 ± 87
MnO ₂ /GAC (wood-based) under 600 °C	10,080 ± 90
MnO ₂ /GAC (wood-based) under 800 °C	8,632 ± 2,092

4.1.5 Resistivity of GAC electrode materials

EIS was used to test the ohmic resistances of the various GAC electrode materials. The internal resistance of electrode materials in MFCs has been studied by many researchers using EIS [41]. The electrical equivalent circuit shown in **Fig. 4.14** was used to analyse the resulted impedance spectra of electrode materials in 0.1 M KCl solutions. This electrical equivalent circuit consists of the element: R electrode resistance, C electrode capacitance, and W Warburg element which represents the simple diffusion of electrolyte solutions [41]. For GAC electrode materials, the Nyquist and Bode-phase plots (as shown in **Fig. 4.12** and **4.13**) show a resistive behavior at low frequencies. This evolution revealed the growth of a passive film on electrode materials. Also, there was a decrease in low frequency impedance with increasing EAS values of GAC electrode materials.

The electrode resistance are shown in **Fig 4.15**, **Table 4.4A** and **4.4B**. The resistance of untreated GAC (coal-based) and GAC (wood-based) were 265.41 and 460.91 Ω respectively. After heat treatment, the resistance of GAC (coal-based) under 600 °C decreased to 165.53 Ω . In contrast, the resistance of GAC (coal-based) under 800 °C increased slightly to 271.72 Ω because of increasing in the amount of oxygen as shown in the EDX results. For heated GAC (wood-based), the resistance of GAC (wood-based) under 600 °C and GAC (wood-based) under 800 °C decreased to 316.72 and 290.16 Ω respectively. When coating MnO₂ onto GAC and heated GAC electrodes, the resistance of these materials were around 38 – 60% lower than that of GAC and heated GAC electrode materials, especially from MnO₂/GAC (coal-based) under 600 °C and MnO₂/GAC (wood-based) under 800 °C.

Normally, the heating method could reduce O/C ratio in carbon which caused the active surface area increasing so the resistance will be decreased. However, the oxygen functionalities on the GAC (coal-based) surface could potentially be increased at 800 °C of heat treatment. The EDX is carried out to test this hypothesis and showed that the oxygen content actually increase again in the GAC (coal-based) under 800 °C (as shown in **Table 4.2A**).

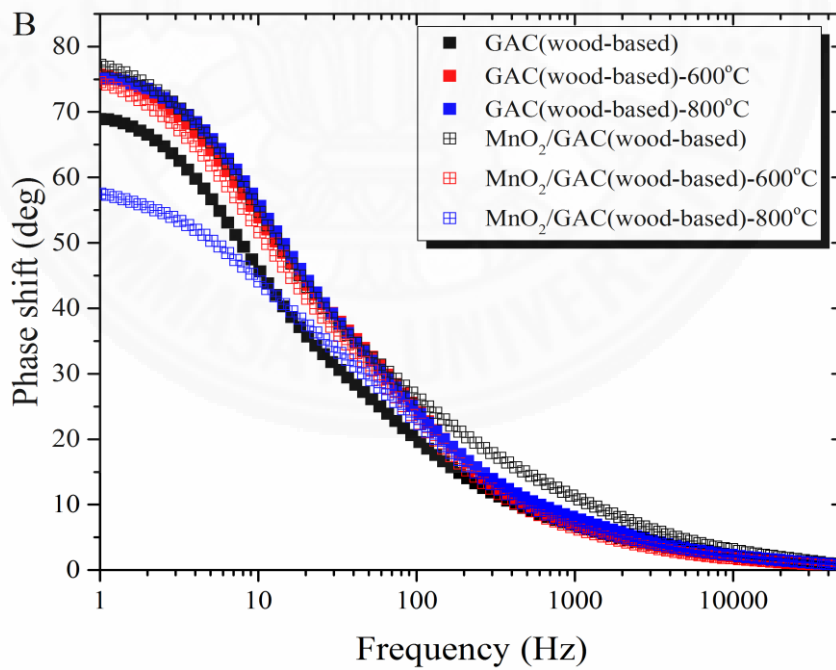
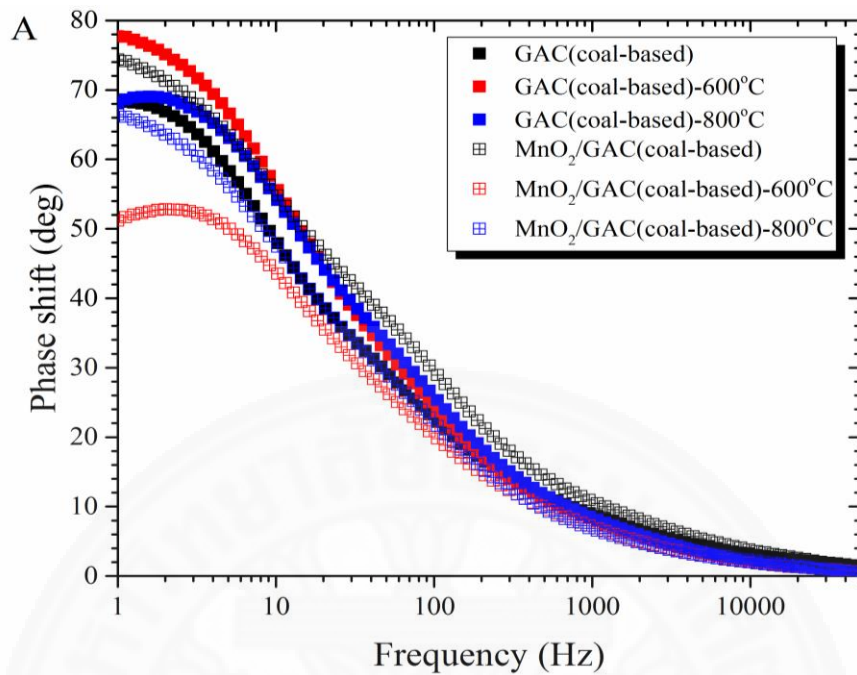


Fig. 4.12 Bode-phase plots of (A) GAC (coal-based) and (B) GAC (wood-based) electrode materials.

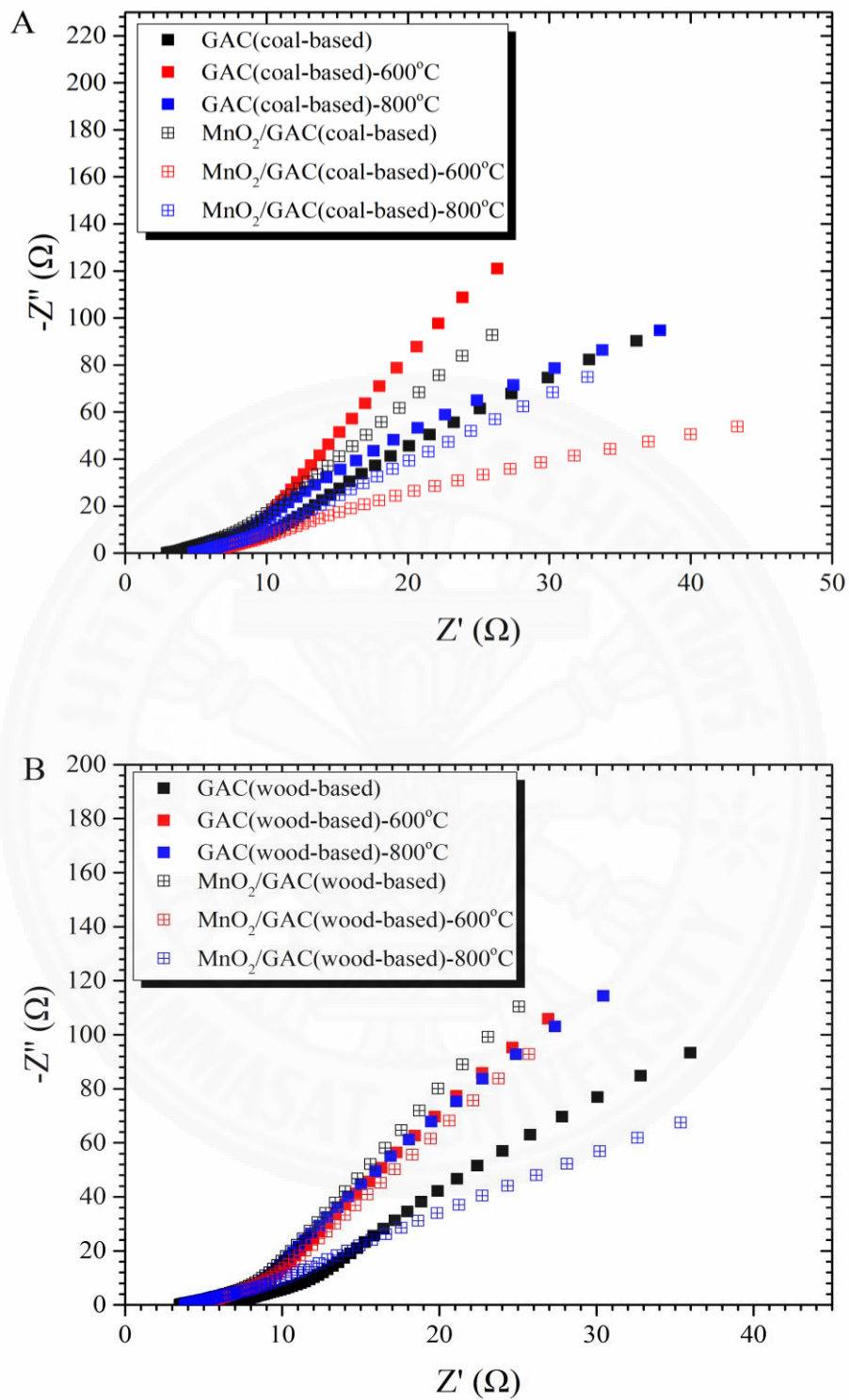


Fig. 4.13 Nyquist plots of (A) GAC (coal-based) and (B) GAC (wood-based) electrode materials in 0.1 M KCl solutions.

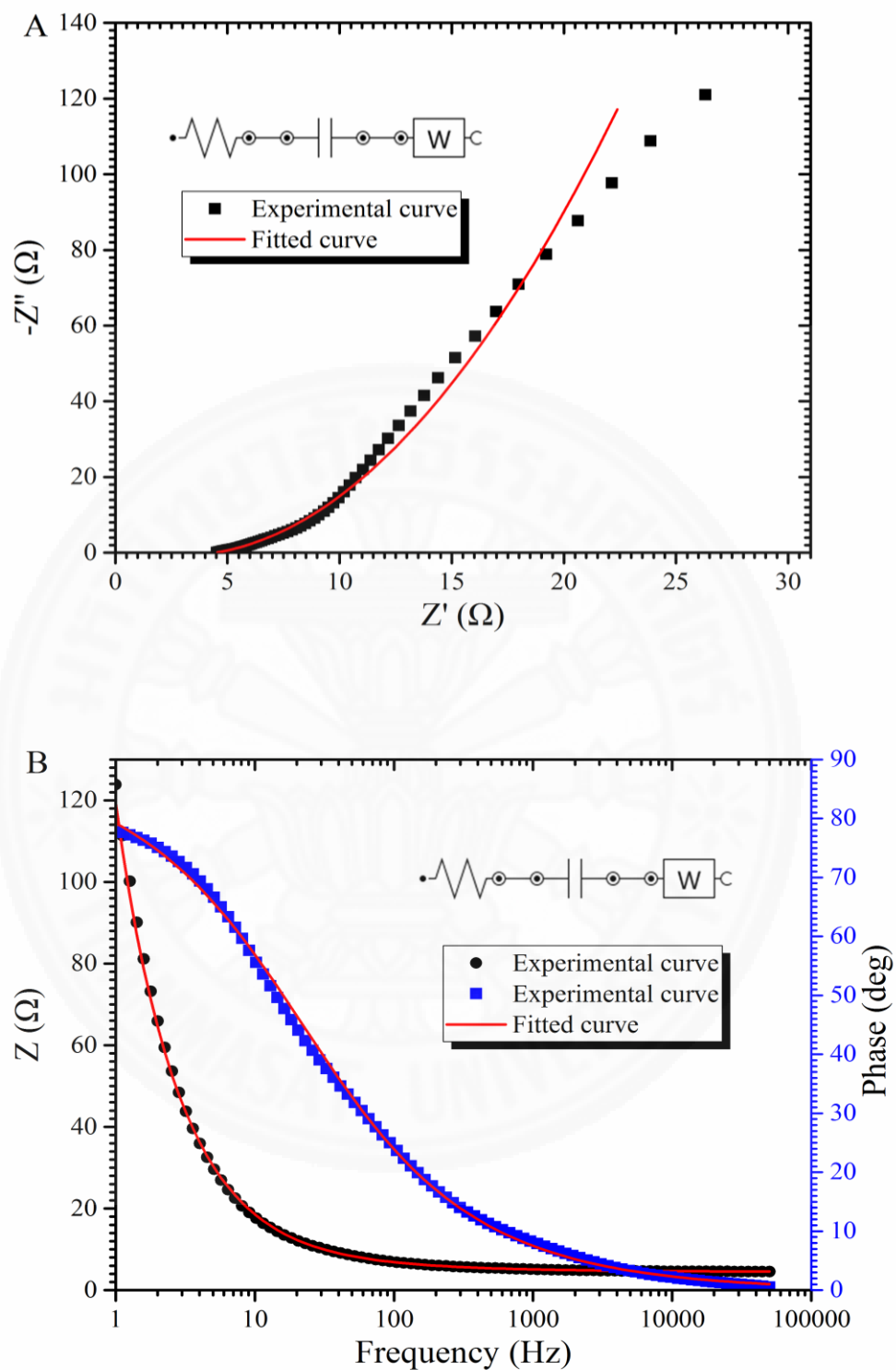


Fig. 4.14 Overlaid experimental and fitted (A) Nyquist plots and (B) Bode-phase plots with equivalent circuit elements of GAC (coal-based) under 600 °C in 0.1M KCl solutions.

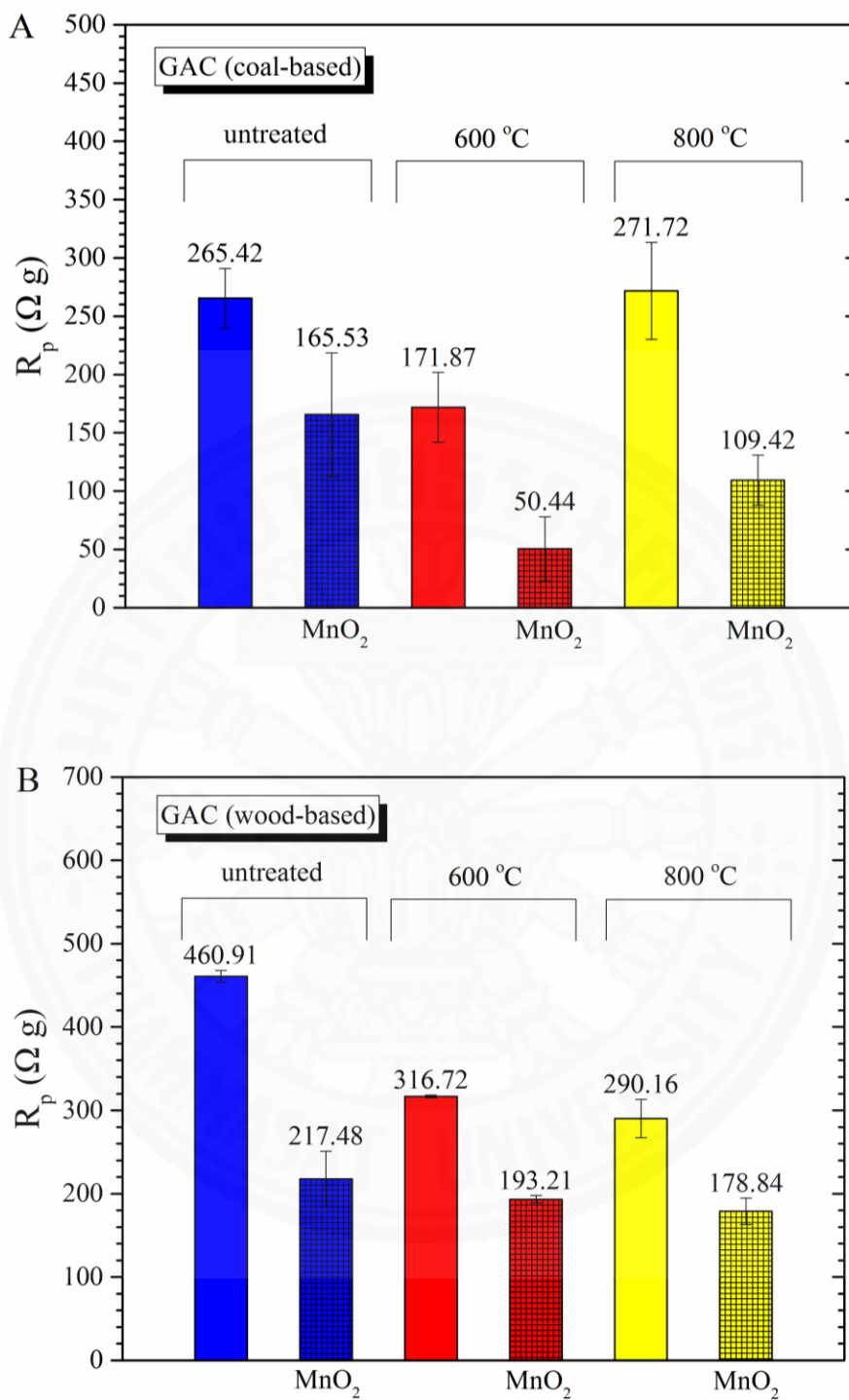


Fig. 4.15 The electrode material resistance (A) GAC (coal-based) and (B) GAC (wood-based) in 0.1 KCl solutions.

Table 4.4A The resistance of GAC (coal-based) electrodes in 0.1M KCl solutions.

Electrode materials	Resistance of the passive film ($\Omega \text{ cm}^2$)		
	Experimental	Fitted	Estimated Error (%)
GAC (coal-based)	265.4 ± 25.5	0.8 ± 0.1	0.5 ± 0
GAC (coal-based) under 600 °C	171.9 ± 29.9	0.5 ± 0.3	0.7 ± 0.3
GAC (coal-based) under 800 °C	271.7 ± 41.7	0.7 ± 0.3	0.5 ± 0
MnO ₂ /GAC (coal-based)	165.5 ± 53.1	0.4 ± 0.1	0.4 ± 0.2
MnO ₂ /GAC (coal-based) under 600 °C	50.4 ± 27.6	0.8 ± 0.3	0.8 ± 0.1
MnO ₂ /GAC (coal-based) under 800 °C	109.4 ± 21.4	0.6 ± 0.2	0.4 ± 0

Table 4.4B The resistance of GAC (wood-based) in 0.1M KCl solutions.

Electrode materials	Resistance of the passive film ($\Omega \text{ cm}^2$)		
	Experimental	Fitted	Estimated Error (%)
GAC (wood-based)	460.9 ± 7.0	1.2 ± 0.3	0.6 ± 0.3
GAC (wood-based) under 600 °C	316.7 ± 1.5	0.5 ± 0.2	0.5 ± 0.2
GAC (wood-based) under 800 °C	290.2 ± 23.1	0.4 ± 0.3	0.4 ± 0.1
MnO ₂ /GAC (wood-based)	217.5 ± 33.4	0.5 ± 0.2	0.6 ± 0.1
MnO ₂ /GAC (wood-based) under 600 °C	193.2 ± 4.6	0.5 ± 0.3	0.3 ± 0
MnO ₂ /GAC (wood-based) under 800 °C	178.8 ± 15.8	0.5 ± 0.1	0.6 ± 0.1

4.2 Modification of SS

4.2.1 Effect of the scan rate of electropolymerisation on morphology

The rate at which the potential was scanned was found to affect the quality of PPy film coated on SS significantly. The weight of synthesised PPy film using different scan rates during electropolymerisation is shown in **Fig. 4.16**. At slow scan rate of 50 mVs^{-1} , the weight of PPy coated onto SS was higher than that of the fast scan rates of 100, 200 and 400 mVs^{-1} . The prolonged polymerisation period occurring at lower scan rate resulted in higher amount of PPy deposition on SS substrates [42].

SEM images of PPy-coated SS compared with the bare SS were demonstrated in **Fig 4.17, 4.18 and 4.19**. The influence of the 300 grade sand paper can be seen in the surface morphology of the bare SS. A uniform globular particle morphology was observable all over the surface of PPy-coated SS electrodes [5]. The PPy film was dense and very homogeneous. For comparison, the surface of PPy-coated SS 304 at 50, 100 and 200 mV s^{-1} films showed typical globular morphology and they presented less smooth compared to the bare SS and PPy-coated SS 304 at 400 mV s^{-1} . The granules in PPy-coated SS 304 at 50, 100, 200 and 400 mV s^{-1} films ranged from $0.1 \mu\text{m}$ to 8, 5, 4 and $2 \mu\text{m}$ respectively. From SEM micrographs of PPy-coated SS316, when the applied scan rates was increased to 400 mV s^{-1} , pore of PPy film and PPy particles were seen on the SS316 surface and the polishing marks from the 300 grade sand paper was still visible. Most of the PPy particles ranged from 1-4 μm for a scan rate of 400 mV s^{-1} . The PPy particle size increased to 2-14 μm for the scan rates of 200 and 100 mV s^{-1} . When the applied scan rate was decreased to 50 mV s^{-1} , the globular particle morphology can be seen in the PPy-coated SS316 and the PPy particles ranged from 4-18 μm .

The surface morphology of PPy film was affected by the scan rate of coating and also provided a large surface area for the electropolymerisation process. Moreover, homogeneous and regular polymer surface became more and more granular as the scan rate decreased.

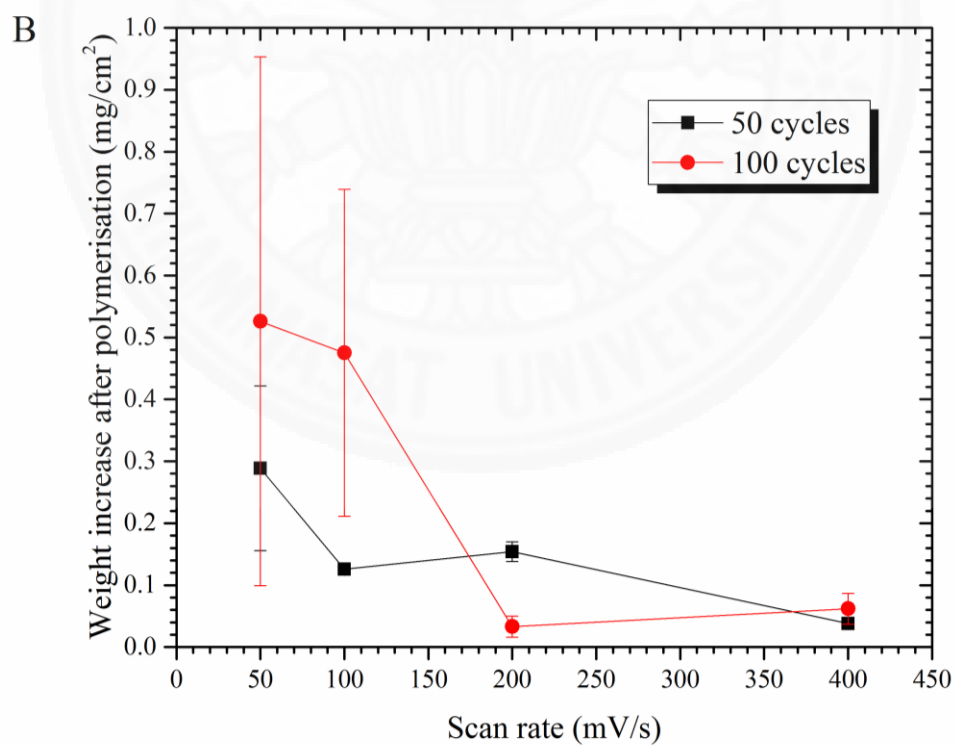
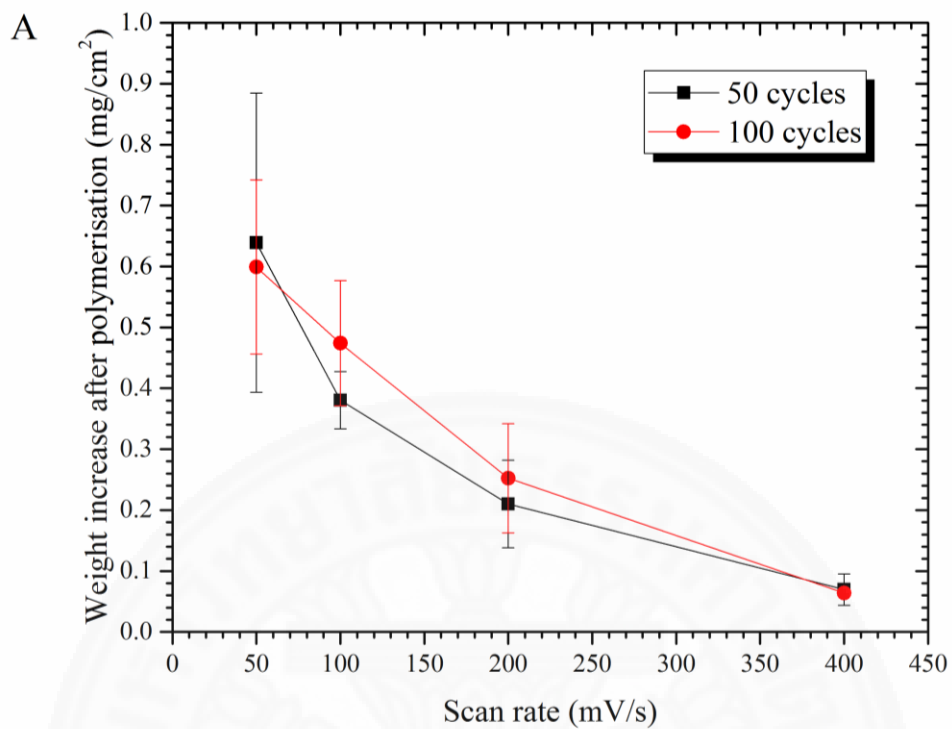


Fig. 4.16 Weight of (A) PPy coated onto SS 304 and (B) PPy coated onto SS 316 surface after electropolymerisation at various scan rates (50cycles and 100cycles).

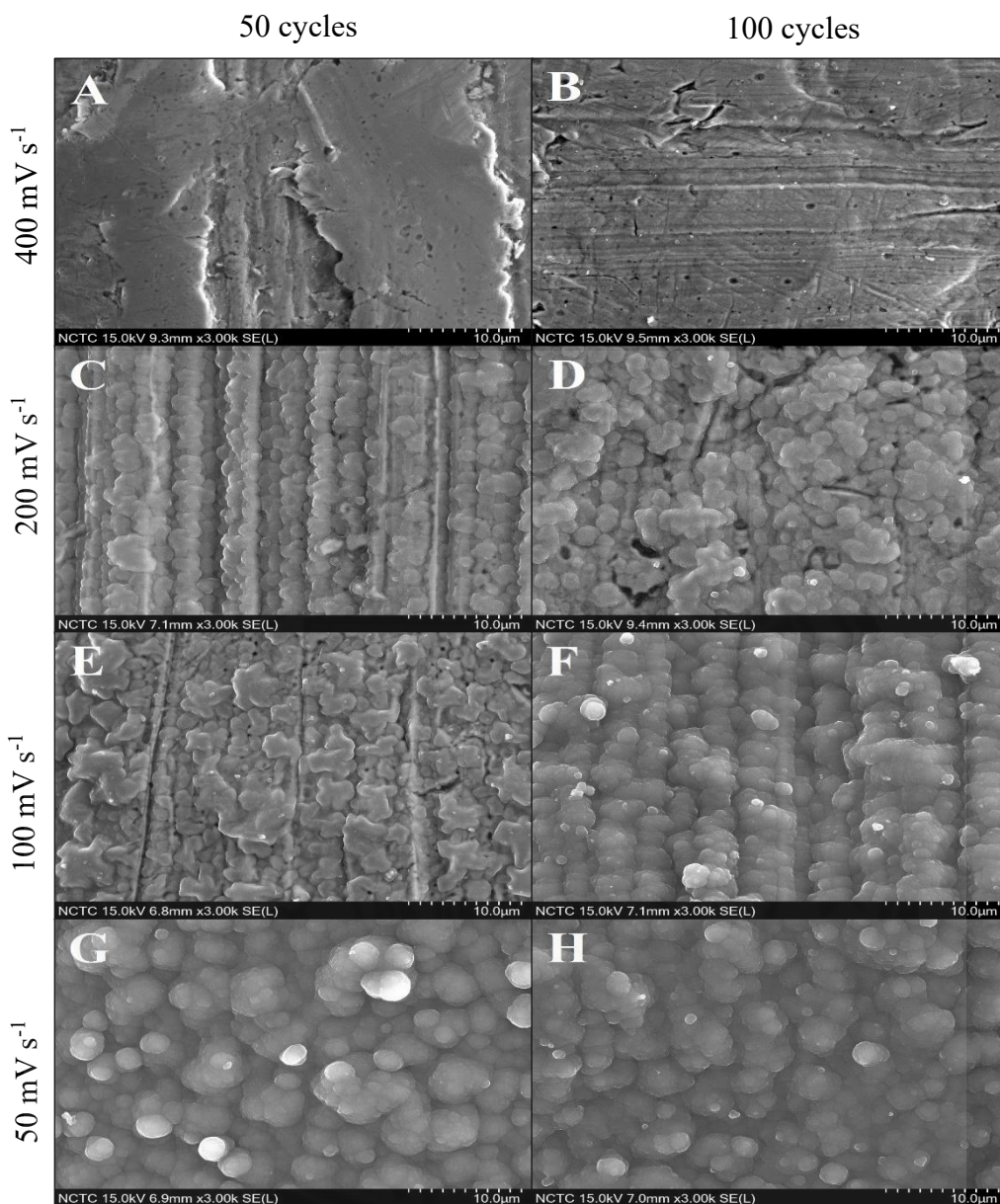


Fig. 4.17 SEM images of PPy-coated SS 304 using different scan rates and number of cycles of electropolymerisation at 3k magnification: (A) PPy-coated SS 304 at 400 mV s^{-1} and 50 cycles, (B) PPy-coated SS 304 at 400 mV s^{-1} and 100 cycles, (C) PPy-coated SS 304 at 200 mV s^{-1} and 50 cycles, (D) PPy-coated SS 304 at 200 mV s^{-1} and 100 cycles, (E) PPy-coated SS 304 at 100 mV s^{-1} and 50 cycles, (F) PPy-coated SS 304 at 100 mV s^{-1} and 100 cycles, (G) PPy-coated SS 304 at 50 mV s^{-1} and 50 cycles and (H) PPy-coated SS 304 at 50 mV s^{-1} and 100 cycles.

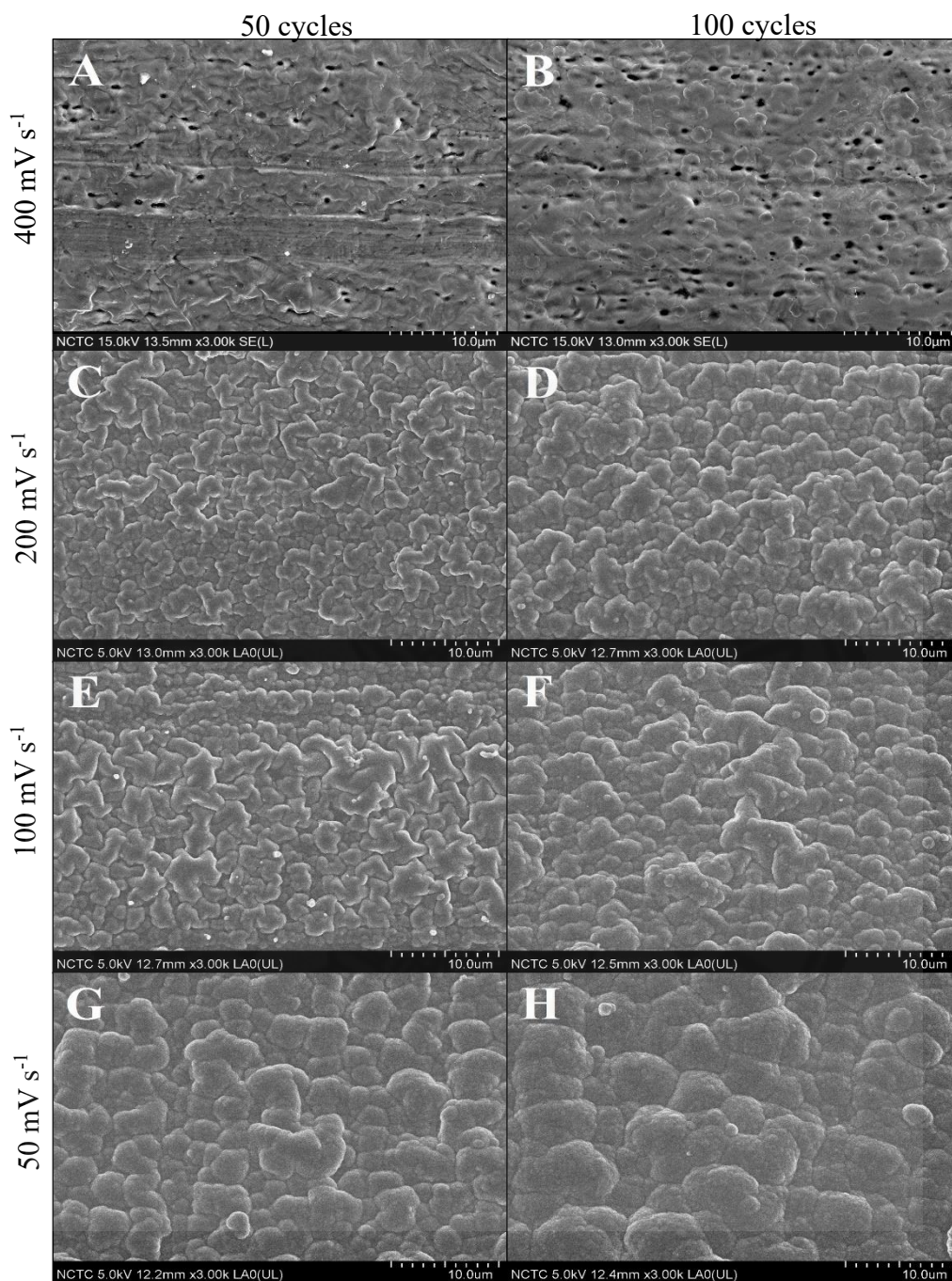


Fig. 4.18 SEM images of PPy-coated SS 316 using different scan rates and number of cycles of electropolymerisation at 3k magnification: (A) PPy-coated SS 316 at 400 mV s^{-1} and 50 cycles, (B) PPy-coated SS 316 at 400 mV s^{-1} and 100 cycles, (C) PPy-coated SS 316 at 200 mV s^{-1} and 50 cycles, (D) PPy-coated SS 316 at 200 mV s^{-1} and 100 cycles, (E) PPy-coated SS 316 at 100 mV s^{-1} and 50 cycles, (F) PPy-coated SS 316 at 100 mV s^{-1} and 100 cycles, (G) PPy-coated SS 316 at 50 mV s^{-1} and 50 cycles and (H) PPy-coated SS 316 at 50 mV s^{-1} and 100 cycles.

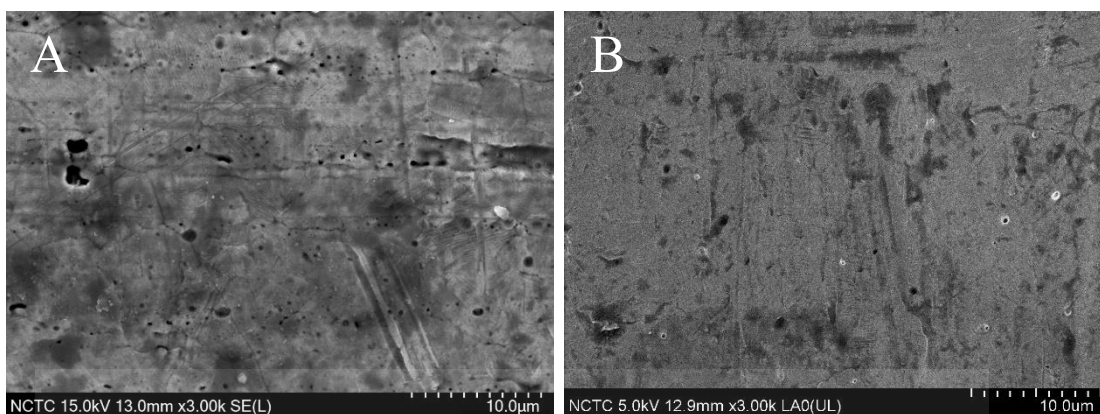


Fig. 4.19 SEM images of (A) bare SS 316 and (B) bare SS 304 mesh at 3k magnification

4.2.2 The morphology of MnO₂ nanostructure

SEM micrographs of MnO₂/bare SS and MnO₂/PPy-coated SS produced at different applied scan rates are shown in **Fig. 4.20** and **4.21**. It has been known that MnO₂ exists in several crystallographic forms, and an oxide prepared by electrochemical oxidation in acidic electrolytes, which is generally called the EMD, has either γ structure or amorphous in nature [3]. From SEM micrographs, the considerable aspect seen in these images is the “cracked film” presence as differently observed in **Fig. 4.20A, 4.20C, 4.21A** and **4.21C**. The cracked films were seen on electrode surface, especially from MnO₂/SS 304, MnO₂/SS 316, MnO₂/PPy-coated SS 304 at 100 mV s⁻¹ under 50 cycles and MnO₂/PPy-coated SS 316 at 200 mV s⁻¹ under 50 cycles. The cracking is the significant factor, which improves the cycle lives by facilitating the expansion and compression process [3, 43].

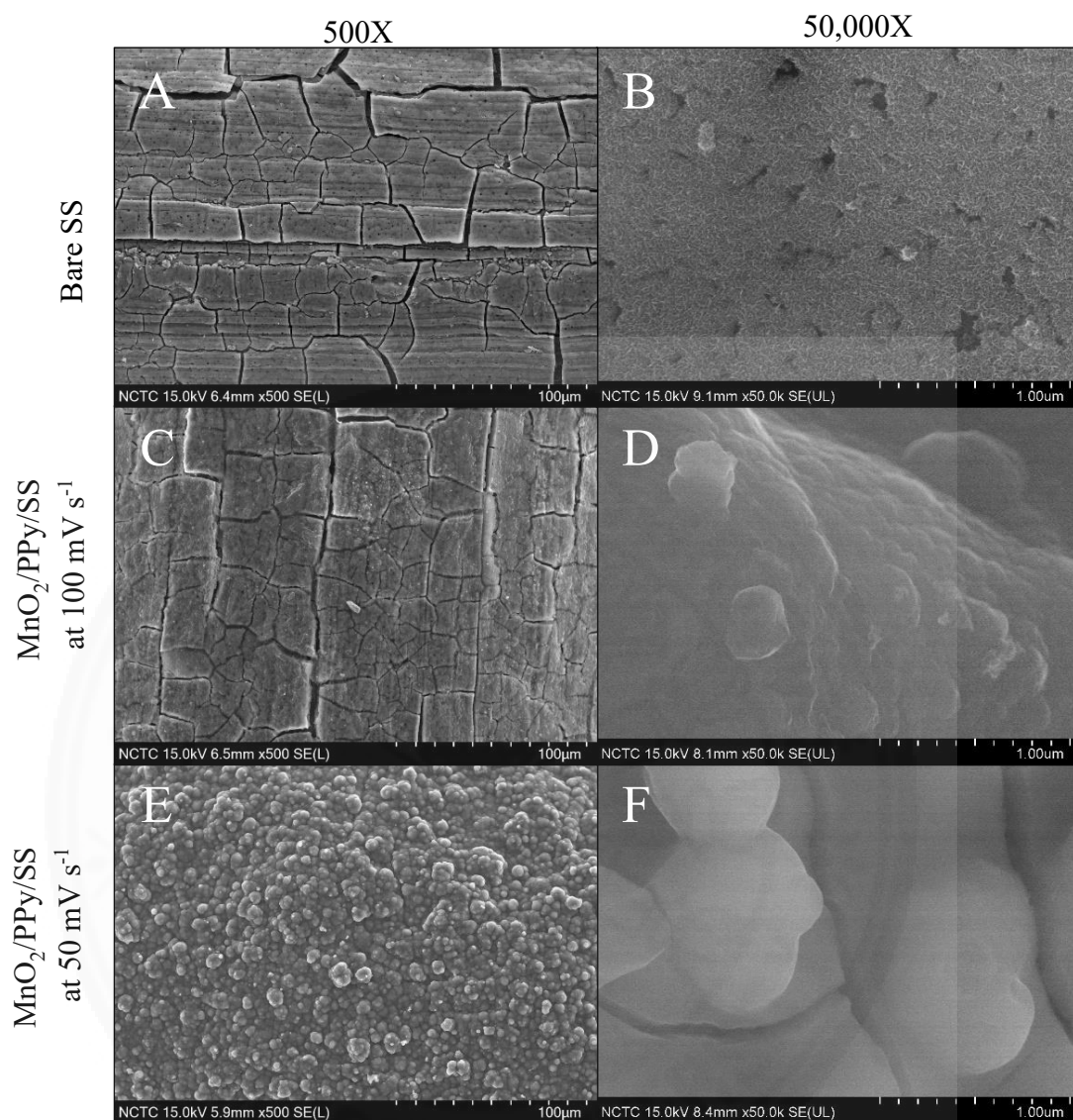


Fig. 4.20 SEM images of MnO₂/bare SS 304 at (A) 500 and (B) 50k magnification, MnO₂/PPy-coated SS 304 at 100 mV s⁻¹ and 50 cycles at (C) 500 and (D) 50k magnification, and MnO₂/PPy-coated SS 304 at 50 mV s⁻¹ and 50 cycles at (E) 500 and (F) 50k magnification.

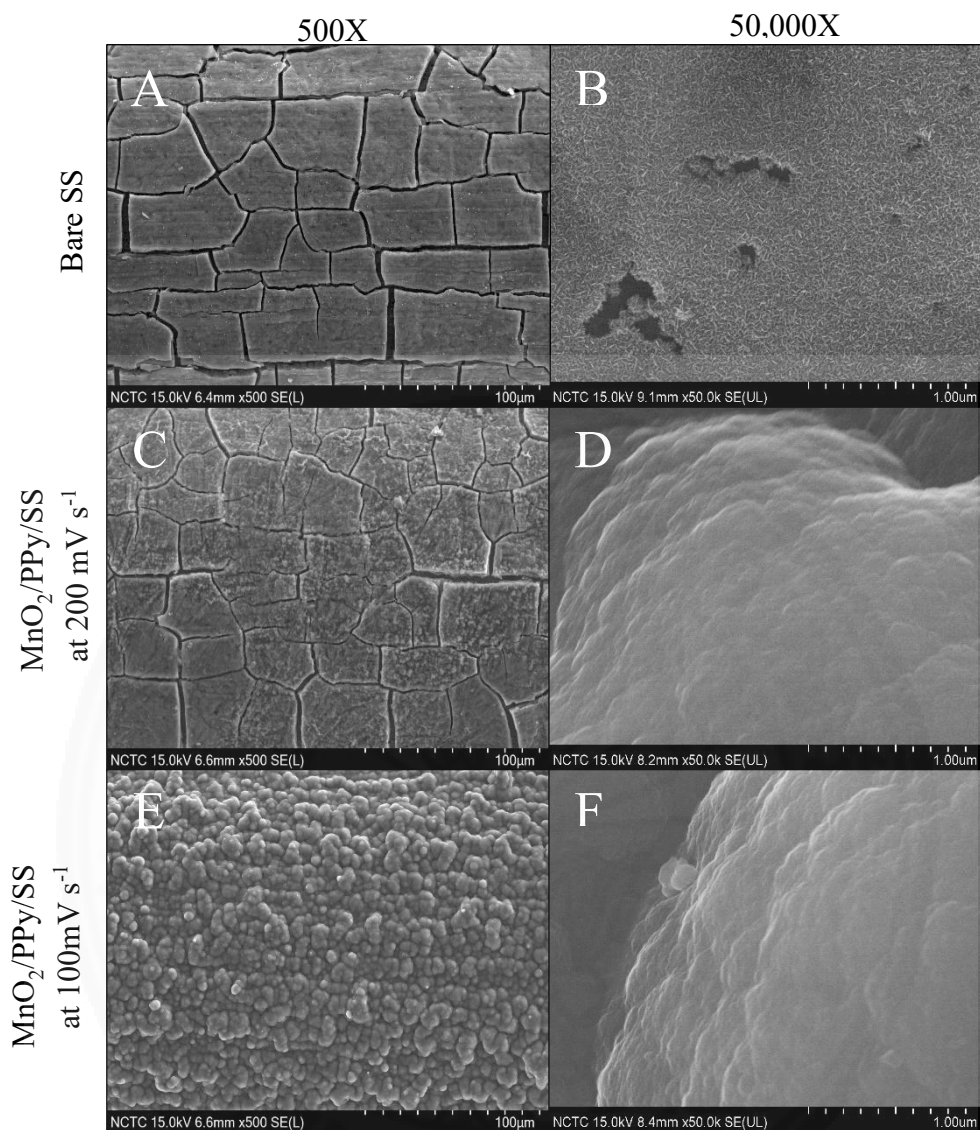


Fig. 4.21 SEM images of MnO₂/bare SS 316 at (A) 500 and (B) 50k magnification, MnO₂/PPy-coated SS 316 at 200 mV s⁻¹ and 50 cycles at (C) 500 and (D) 50k magnification, and MnO₂/PPy-coated SS 316 at 100 mV s⁻¹ and 50 cycles at (E) 500 and (F) 50k magnification.

4.2.3 XRD and EDX results

The X-ray diffraction of electrodeposited MnO_2 is shown in **Fig. 4.22**. It confirms that there is the electrodeposition of $\gamma\text{-MnO}_2$ on SS and PPy-coated SS surfaces. The average elemental composition of various MnO_2 deposited on the bare SS and PPy-coated SS surfaces was analysed by EDX as shown in **Fig. 4.23**. It confirms the existence of MnO_2 on the surface of deposited electrode materials by electrodeposition. **Table 4.5** shows percentage of MnO_2 deposited at different electrode materials. It shows that the amount of Mn on bare SS and PPy-coated SS 304 at 100 mV s^{-1} and PPy-coated SS 316 at 200 mV s^{-1} were higher than that of PPy-coated SS at slow scan rate. A little amount of nitrogen and sulfur occurred PPy-coated SS and MnO_2/PPy -coated SS may be due to the transformation of pyrrole to PPy in electropolymerisation and manganese (II) sulfate to manganese dioxide under CV process.

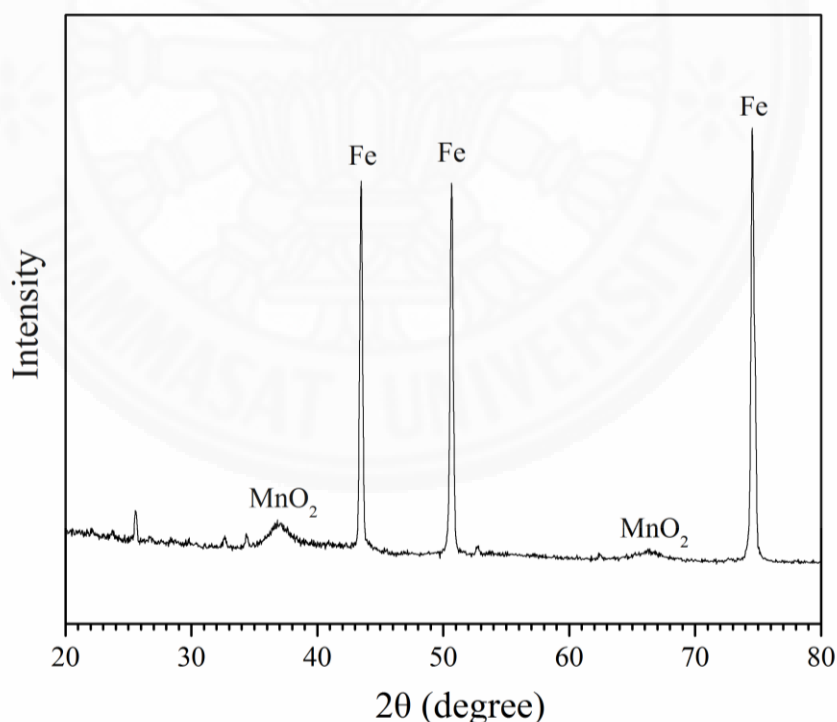


Fig. 4.22 XRD spectrum of MnO_2 deposited on the SS surface.

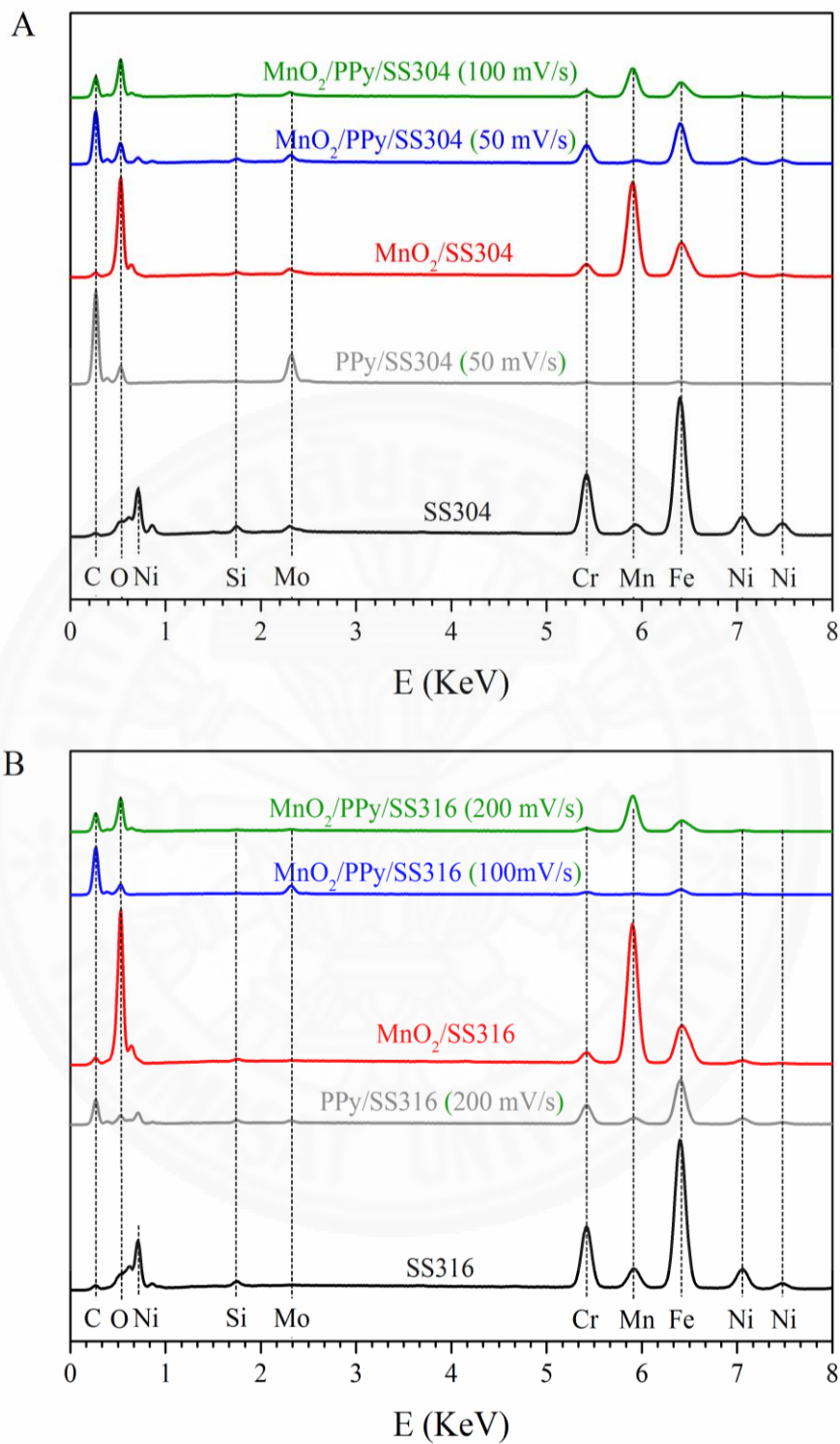


Fig. 4.23 EDX analysis of MnO₂ electrodeposited on different (A) SS304 and (B) SS316 electrode materials.

Table 4.5A Elemental composition of various SS304 electrode materials corresponding to EDX spectrum.

Electrode materials	Average elemental composition (% wt)									
	C	N	O	Si	Mo	S	Cr	Mn	Fe	Ni
Bare SS304	2.64	0	4.62	1.33	2.32	0	16.67	1.00	62.26	9.12
PPy/SS304 (50 mV s ⁻¹)	58.50	15.14	19.69	0	0	4.65	0.55	0	1.48	0
MnO ₂ /SS304	4.03	0	29.50	0.53	2.18	0	3.91	43.03	15.46	1.45
MnO ₂ /PPy/SS304 (50 mV s ⁻¹)	38.81	7.47	12.66	0.56	0	1.21	7.75	0.43	27.33	3.78
MnO ₂ /PPy/SS304 (100 mV s ⁻¹)	22.57	4.84	27.38	0.48	0	1.00	3.52	25.84	13.11	1.29

Table 4.5B Elemental composition of various SS 316 electrode materials corresponding to EDX spectrum.

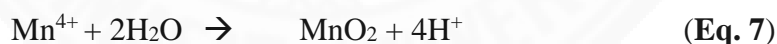
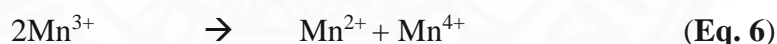
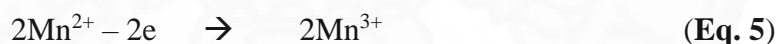
Electrode materials	Average elemental composition (%wt)									
	C	N	O	Si	Mo	S	Cr	Mn	Fe	Ni
Bare SS316	3.03	0	3.99	1.09	0.32	0	16.60	4.98	66.62	3.40
PPy/SS316 (200 mV s ⁻¹)	29.06	5.69	6.77	0.74	0	0.70	10.67	3.06	41.22	2.13
MnO ₂ /SS316	4.01	0	28.01	0.29	0.26	0	2.72	51.21	13.24	0.28
MnO ₂ /PPy/SS316 (100 mV s ⁻¹)	55.13	13.53	20.24	0	0	2.93	1.82	0.45	5.91	0
MnO ₂ /PPy/SS316 (200 mV s ⁻¹)	21.54	4.60	27.19	0.35	0	0.44	2.41	31.77	11.49	0

4.2.4 Electropolymerisation of PPy

To investigate the effect of incorporation of PPy in the SS substrate, the CV curves were measured as in **Fig. 4.24**. At the first cycle, the current was very low from -0.01 to 0.02 V. With increasing number of cycles, the incorporation of PPy significantly improved the current output over a potential range, compared with uncoated SS at first cycle. They also suggested the enhanced current of subsequent cycles because of the increased EAS value of the electrode materials. The reason for current improvement is the oxygen reduction of PPy on the electrodes. In general, the globular morphology of the resulting PPy film varied with scan rate; at slow scan rate and the thinner layer, the surface of SS was more granular than the fast scan with the thicker layer.

4.2.5 Electrodeposition of MnO₂

From the kinetic study by CV method, based on the results of analysis of original data [3], the accepted, more substantiated scheme of the mechanism of Mn²⁺ ions electrooxidation in the acidic medium of the product of irreversible electrode reaction and hydrolysis, is as follows:



CV recorded during preparation of MnO₂ on SS are shown in **Fig. 4.25**. Although the voltammograms in the absence and in the presence of PPy are similar in shape, the current of MnO₂ on the bare SS is higher than other electrode materials. The anodic peaks at about 1.28 – 1.42 V correspond to the oxidation of Mn²⁺ to MnO₂ and the cathodic peaks at about 0.8 – 0.4 V corresponding to the reduction of MnO₂ to MnOOH. The reason could be the partial reduction of MnO₂, which starts occurring at about 1.1 V during cathodic half-cycle. During repeated cycling, the partial reduction

and then further oxidation or deposition of the fresh oxide layer on the previous layer could have resulted in a high porosity of the oxides [3].

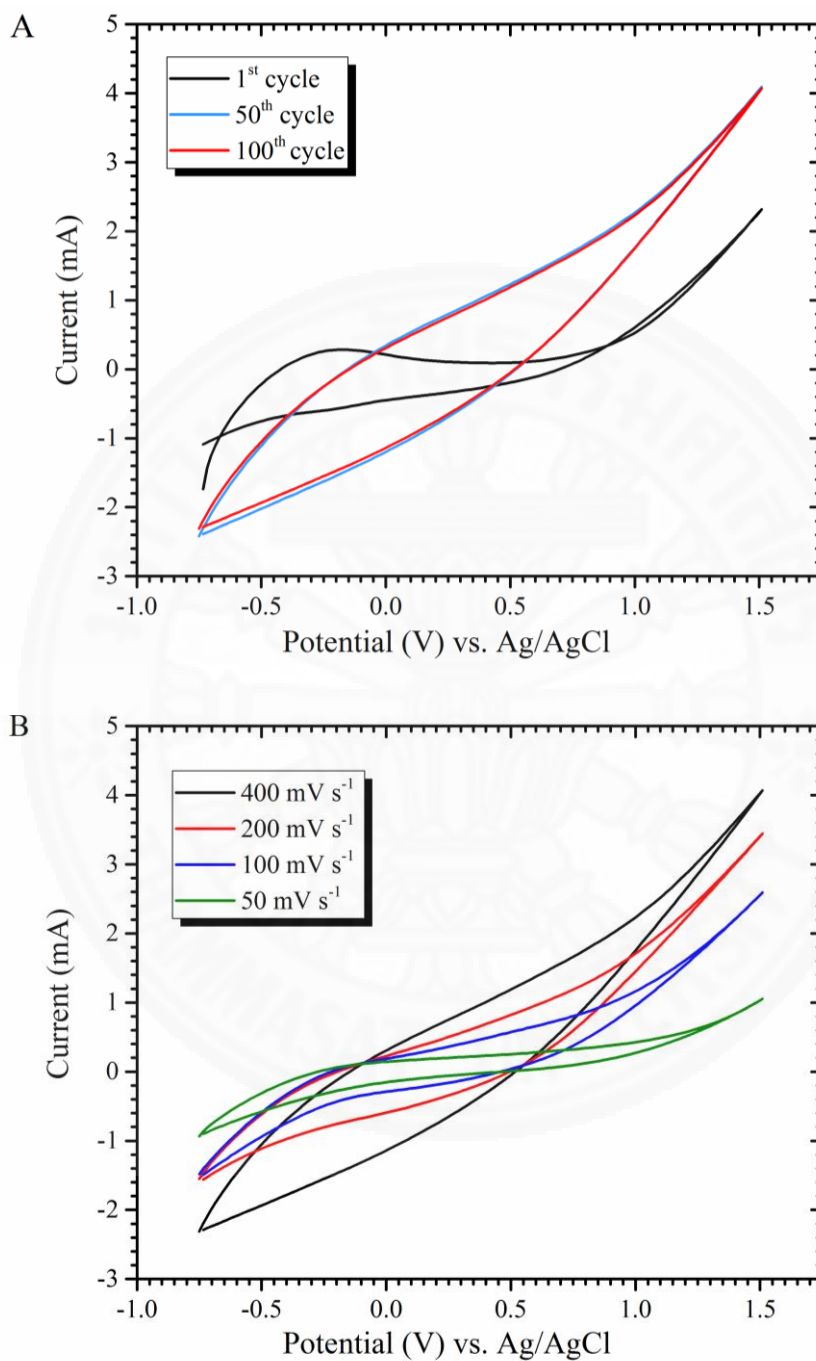


Fig. 4.24 CV of PPy-coated SS recorded at (A) various cycles of the same potential scan rate of 400 mV s⁻¹ and (B) various scan rates of the same of 100th cycle.

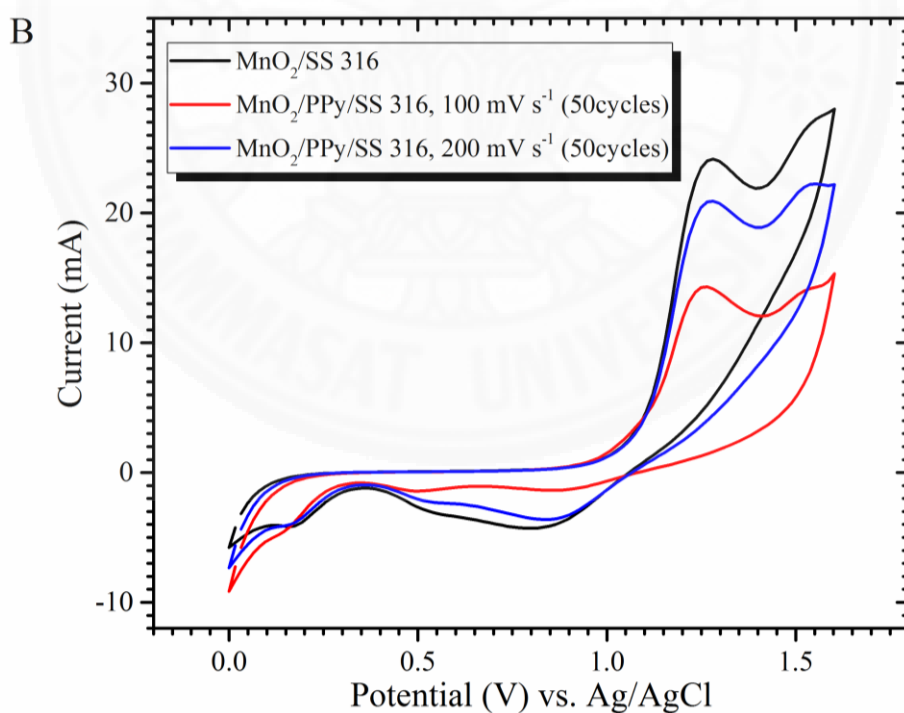
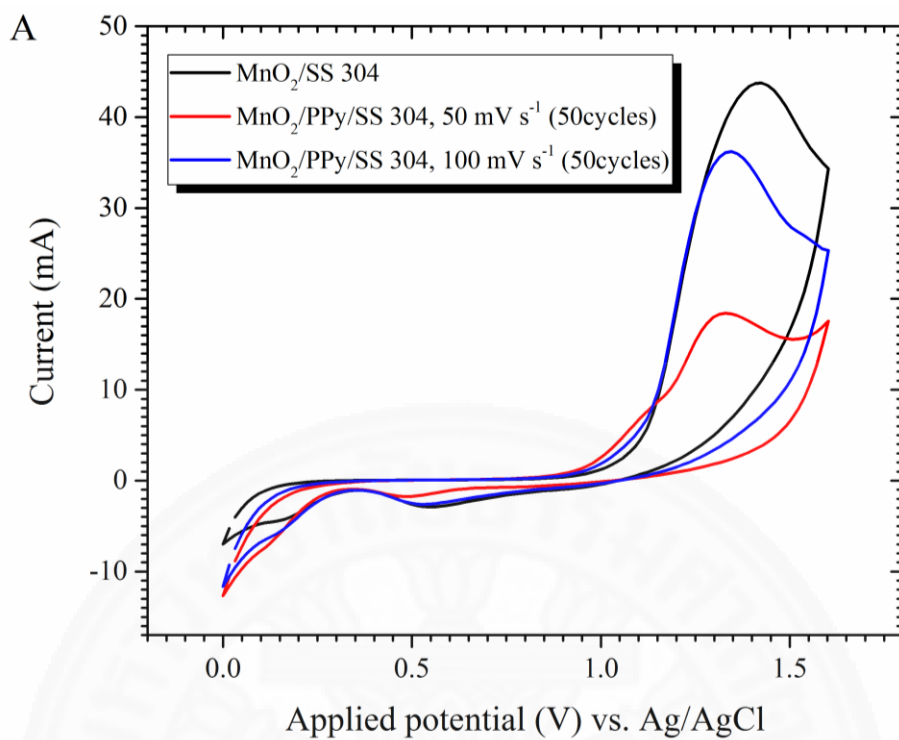


Fig. 4.25 CV for electrodeposition of MnO₂ on (A) SS 304 and (B) SS 316 substrates in the mixture of 1 M MnSO₄ and 0.1 M H₂SO₄ solutions at potential scan rate of 200 mV s⁻¹.

4.2.6 Chemical properties

Fig. 4.26 shows FTIR spectrum of the synthesised PPy coating. It was found that the absorption bands at $1,412\text{ cm}^{-1}$ and $1,257\text{ cm}^{-1}$ were associated with the C–N stretching vibration of PPy [44, 45]. The absorption band at $2,961\text{ cm}^{-1}$ was assigned to the aromatic stretching vibration of C–H bond [44]. The absorption band at $1,559\text{ cm}^{-1}$ could be attributed to typical PPy ring vibrations [44]. The peak at $1,014\text{ cm}^{-1}$ was referred to N–H stretching vibration [44, 45]. Transmittance peak 792 cm^{-1} band was associated with C–C and C–H out of plane ring deformation vibrations [44]. From these absorption bands, they indicated that the black film which was coated on SS substrate was PPy.

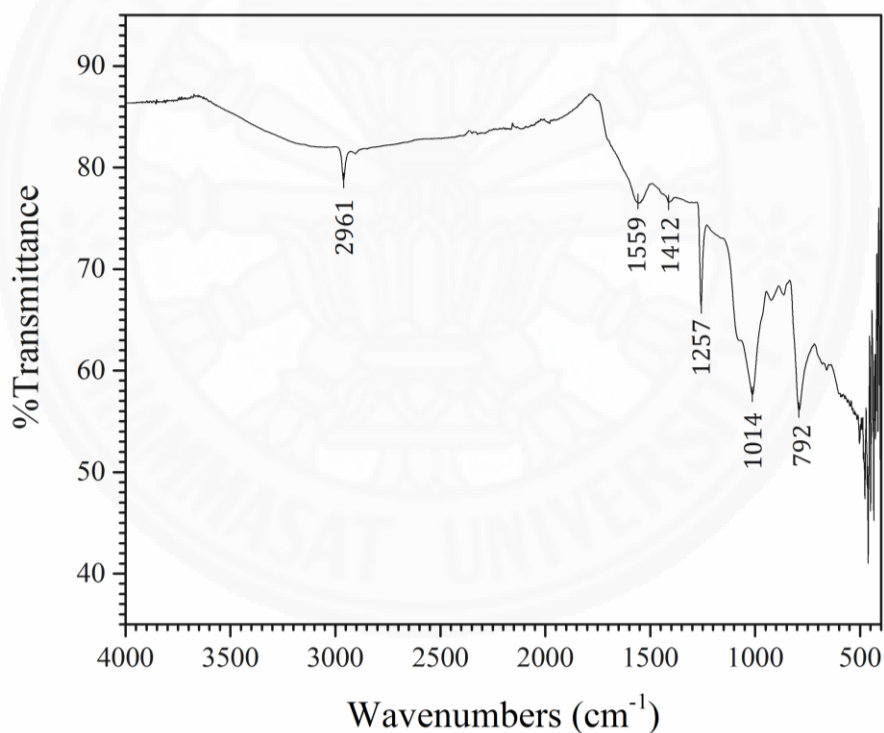


Fig. 4.26 FTIR spectrum of PPy coated on stainless steel substrate.

4.2.7 EAS of SS electrode materials

The experimental EAS value was calculated using the Randles-Sevcik equation as in **Eq. 4** in chapter 2 [40]. The value $i_p/v^{1/2}$ was the slope obtained from the graph plotted between the peak currents (extracted from **Fig.4.27** and **4.28**) and the square root of the scan rates as shown in **Fig. 4.29** and **4.30**. The linear relationship observed between the peak current and the square root of the potential scan rate illustrates that the electrochemical system had not been adversely affected by the existence of PPy film.

The peak currents gained from CV ranged from 0.003 to 0.083 A with the $K_4Fe(CN)_6$ solution. The EAS values varied from 100 to 3962 cm^2 per 1 cm^2 of the geometric surface area (as shown in **Table 4.6** and **4.7**). The bare SS showed that without surface modification, this material had little activity toward electron transfer with the $K_4Fe(CN)_6$ solution. Following modification with PPy coating, the EAS of PPy-coated SS increased to 165 - 558% compared to the bare SS. Moreover, modification with PPy coating and MnO_2 electrodeposition caused the EAS increasing by 1,192 – 3,594% compared to the bare SS.

For electropolymerisation of SS 304, at slow scan rates and the thinner layer of 100 and 50 $mV s^{-1}$, PPy-coated SS exhibited highest EAS values of 552 (± 121) and 550 (± 75) cm^2 respectively. For SS 316, at slow scan rates and the thinner layer of 100 and 200 $mV s^{-1}$, PPy-coated SS exhibited highest EAS values of 240 (± 845) and 156 (± 26) cm^2 respectively. Therefore, the electrode modification to prepare large quantity and high quality of PPy film could be achieved using the slower scan rates [42] of 50 and 100 $mV s^{-1}$ (for SS 304) and 100 and 200 $mV s^{-1}$ (for SS 316) under 50 cycles of electropolymerisation for MnO_2 electrodeposition.

After MnO_2 electrodeposition, all of the MnO_2 electrodeposited on PPy-coated SS samples exhibited an increased EAS when compared to the bare steels and PPy-coated SS electrodes. Specifically, MnO_2 /PPy-coated SS 304 at 100 $mV s^{-1}$ under 50 cycles and MnO_2 /PPy-coated SS 316 at 200 $mV s^{-1}$ under 50 cycles had the maximum EAS values of 3,962 (± 73) and 3,727 (± 150) cm^2 respectively.

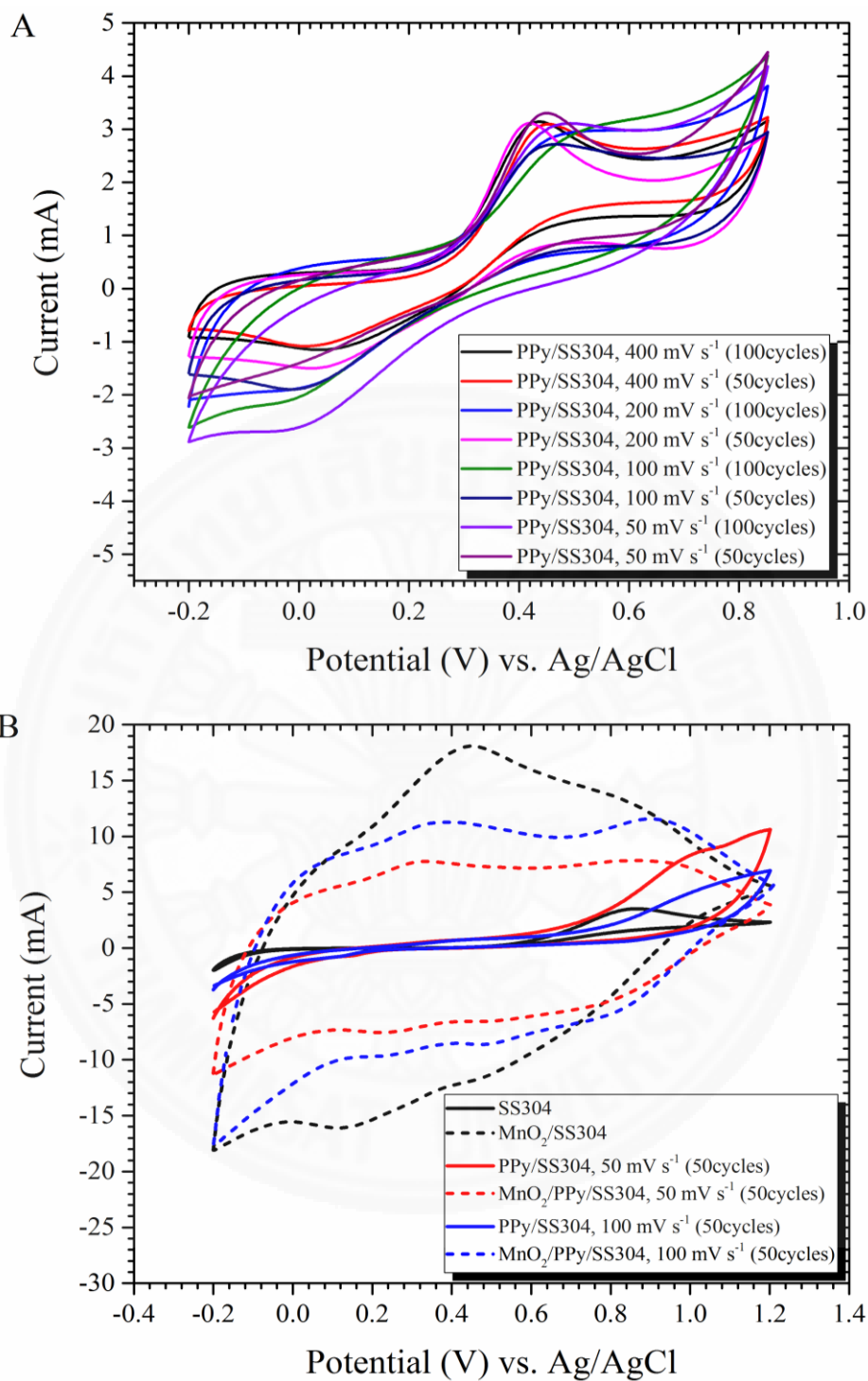


Fig. 4.27 CV of 10 mM $K_4Fe(CN)_6$ in 1.0 M KNO_3 solution recorded at various SS 304 electrodes at the same potential scan rate of 25 mV s^{-1} .

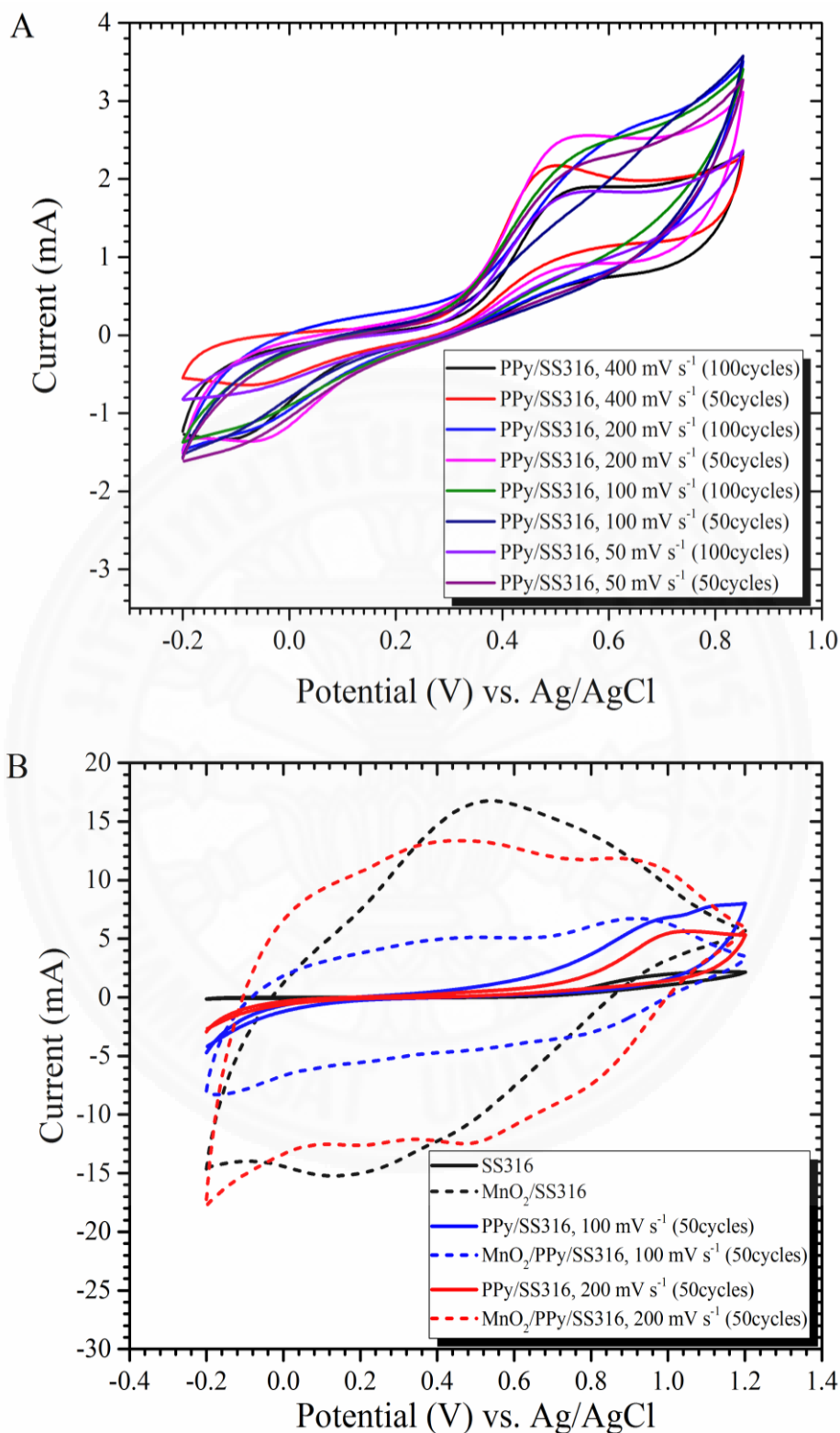


Fig. 4.28 CV of 10 mM $K_4Fe(CN)_6$ in 1.0 M KNO_3 solution recorded at various SS 316 electrodes at the same potential scan rate of 25 mV s^{-1} .

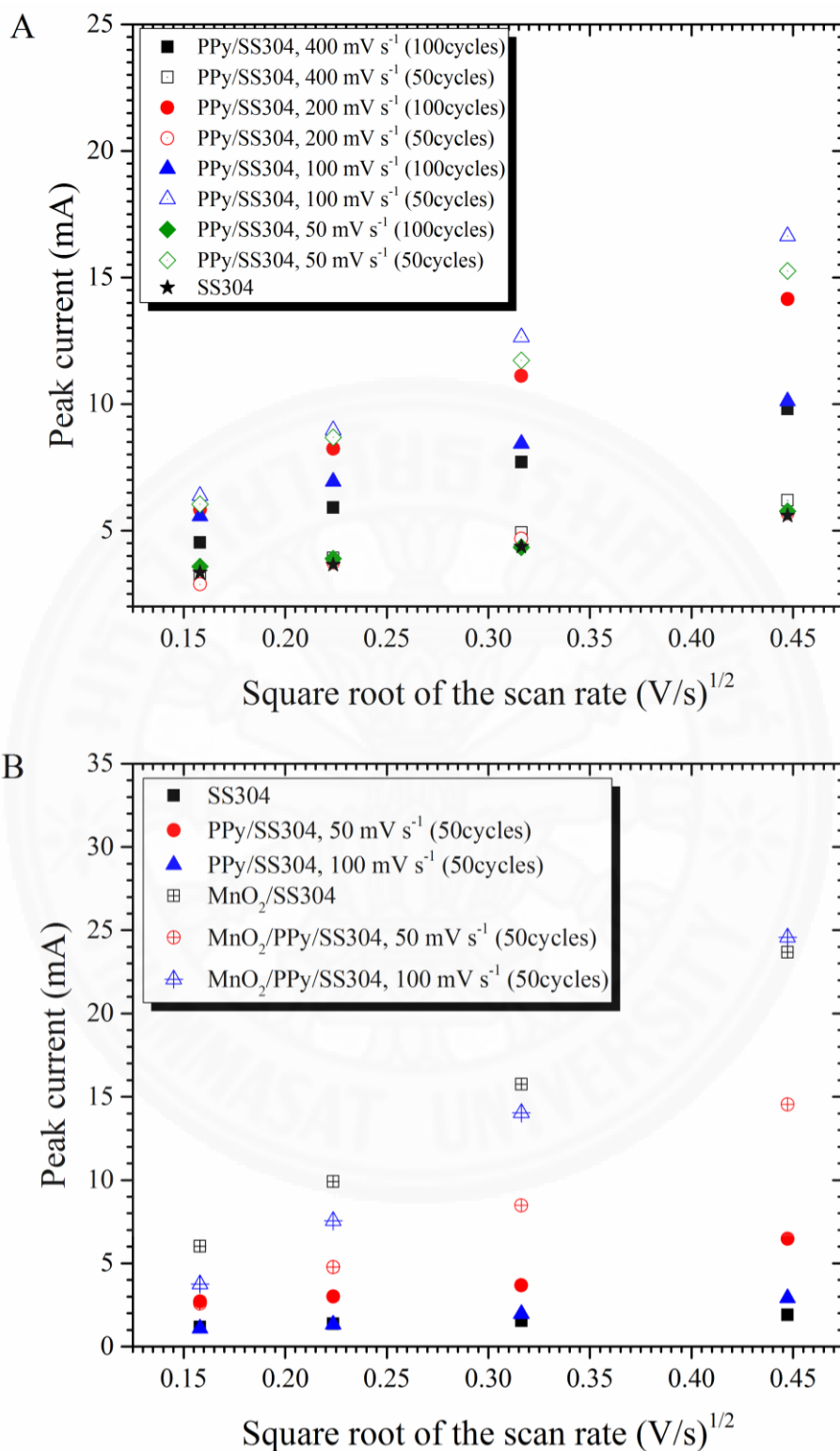


Fig. 4.29 Graphs plotted between the peak currents and square root of the scan rates according to the Randles-Sevcik equation. The peak currents were recorded on various SS 304 electrodes.

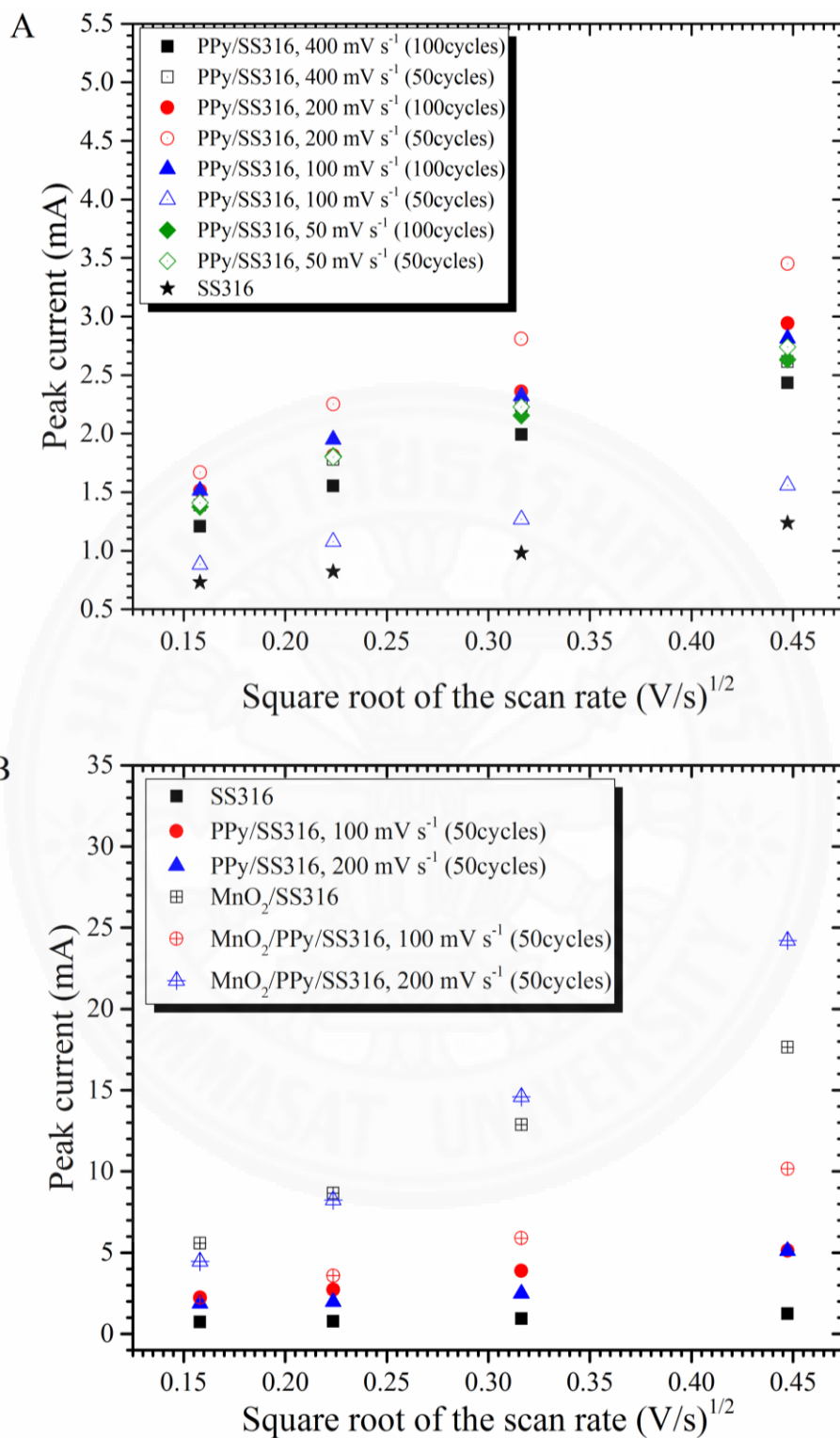


Fig. 4.30 Graphs plotted between the peak currents and square root of the scan rates according with the Randles-Sevcik equation. The peak currents were recorded on various SS 316 electrodes.

Table 4.6A The active electrode surface area (A) of SS 304 electrodes calculated from the Randle-Sevcik equation.

Electrode materials	Active surface area (cm²) per 1 cm² of geometric surface area
Bare SS 304	148 ± 17
PPy-coated SS 304, 50mV s ⁻¹ , 50cycles	550 ± 75
PPy-coated SS 304, 50mV s ⁻¹ , 100cycles	309 ± 140
PPy-coated SS 304, 100mV s ⁻¹ , 50cycles	552 ± 121
PPy-coated SS 304, 100mV s ⁻¹ , 100cycles	262 ± 21
PPy-coated SS 304, 200mV s ⁻¹ , 50cycles	359 ± 138
PPy-coated SS 304, 200mV s ⁻¹ , 100cycles	532 ± 85
PPy-coated SS 304, 400mV s ⁻¹ , 50cycles	167 ± 56
PPy-coated SS 304, 400mV s ⁻¹ , 100cycles	283 ± 52

Table 4.6B The active electrode surface area (A) of SS 316 electrodes calculated from the Randle-Sevcik equation.

Electrode materials	Active surface area (cm²) per 1 cm² of geometric surface area
Bare SS 316	99 ± 2
PPy-coated SS 316, 50mV s ⁻¹ , 50cycles	111 ± 100
PPy-coated SS 316, 50mV s ⁻¹ , 100cycles	112 ± 87
PPy-coated SS 316, 100mV s ⁻¹ , 50cycles	156 ± 26
PPy-coated SS 316, 100mV s ⁻¹ , 100cycles	143 ± 71
PPy-coated SS 316, 200mV s ⁻¹ , 50cycles	240 ± 85
PPy-coated SS 316, 200mV s ⁻¹ , 100cycles	265 ± 74
PPy-coated SS 316, 400mV s ⁻¹ , 50cycles	126 ± 79
PPy-coated SS 316, 400mV s ⁻¹ , 100cycles	120 ± 15

Table 4.7A The active electrode surface area (A) of SS 304 electrodes calculated from the Randle-Sevcik equation (2).

Electrode materials	Active surface area (cm²) per 1 cm² of geometric surface area
Bare SS 304	161 ± 17
PPy-coated SS 304, 50mV s ⁻¹ , 50cycles	521 ± 157
PPy-coated SS 304, 100mV s ⁻¹ , 50cycles	425 ± 52
MnO ₂ / Bare SS 304	3,788 ± 275
MnO ₂ / PPy-coated SS 304, 50mV s ⁻¹ , 50cycles	2,164 ± 377
MnO ₂ / PPy-coated SS 304, 100mV s ⁻¹ , 50cycles	3,962 ± 73

Table 4.7B The active electrode surface area (A) of SS 316 electrodes calculated from the Randle-Sevcik equation (2).

Electrode materials	Active surface area (cm²) per 1 cm² of geometric surface area
Bare SS 316	100 ± 2
PPy-coated SS 316, 100mV s ⁻¹ , 50cycles	664 ± 63
PPy-coated SS 316, 200mV s ⁻¹ , 50cycles	304 ± 237
MnO ₂ / Bare SS 316	3,045 ± 521
MnO ₂ / PPy-coated SS 316, 100mV s ⁻¹ , 50cycles	1,303 ± 323
MnO ₂ / PPy-coated SS 316, 200mV s ⁻¹ , 50cycles	3,727 ± 150

4.2.8 Resistivity of SS electrode materials

The EIS response of the bare SS, MnO₂/SS, PPy-coated SS and MnO₂/PPy-coated SS in 0.1 KCl solutions was carried out and the results are showed as Nyquist plots in **Fig. 4.32**. For stainless steel mesh, the Nyquist and Bode-phase plots (as shown in **Fig. 4.31**) show a resistive behavior at low frequencies, but in the middle to high frequency range there was a marked capacitive response. The Bode-phase curves show one time constant (only one maximum phase lag at the high frequency range). This evolution revealed the growth of a PPy and MnO₂ film on electrode materials. Also, there was a decrease in low frequency impedance with increasing EAS values of electrode materials.

The electrical equivalent circuit shown in **Fig. 4.33** was used to analyse the resulted impedance spectra of the electrode materials in 0.1 M KCl solutions. This electrical equivalent circuit is composed of: R_s – solution resistance; Q_{pf} – constant phase element corresponding to the capacitance of the passive film; and R_{pf} – resistance of the passive film. This equivalent circuit has provided good fitting for the impedance data. This equivalent circuit consists of one time constant as proposed by Feng et al. [46, 47] to describe the passive behavior of SS in alkaline solutions. **Fig. 4.34** shows the electrode resistance and electrode capacitance in 0.1 KCl solutions. As can be seen in **Table 4.8**, for modified SS, the resistance of passive film decreased with increase in EAS values and cracking film on electrode surface, especially from MnO₂/PPy-coated SS304 at 100 mV s⁻¹ under 50 cycles and MnO₂/PPy-coated SS316 at 200 mV s⁻¹ under 50 cycles electrodes, which were around 3.16 and 0.28 Ω lower than that of PPy-coated SS304 at 100 mV s⁻¹ and PPy-coated SS316 at 200 mV s⁻¹ under 50 cycles electrodes.

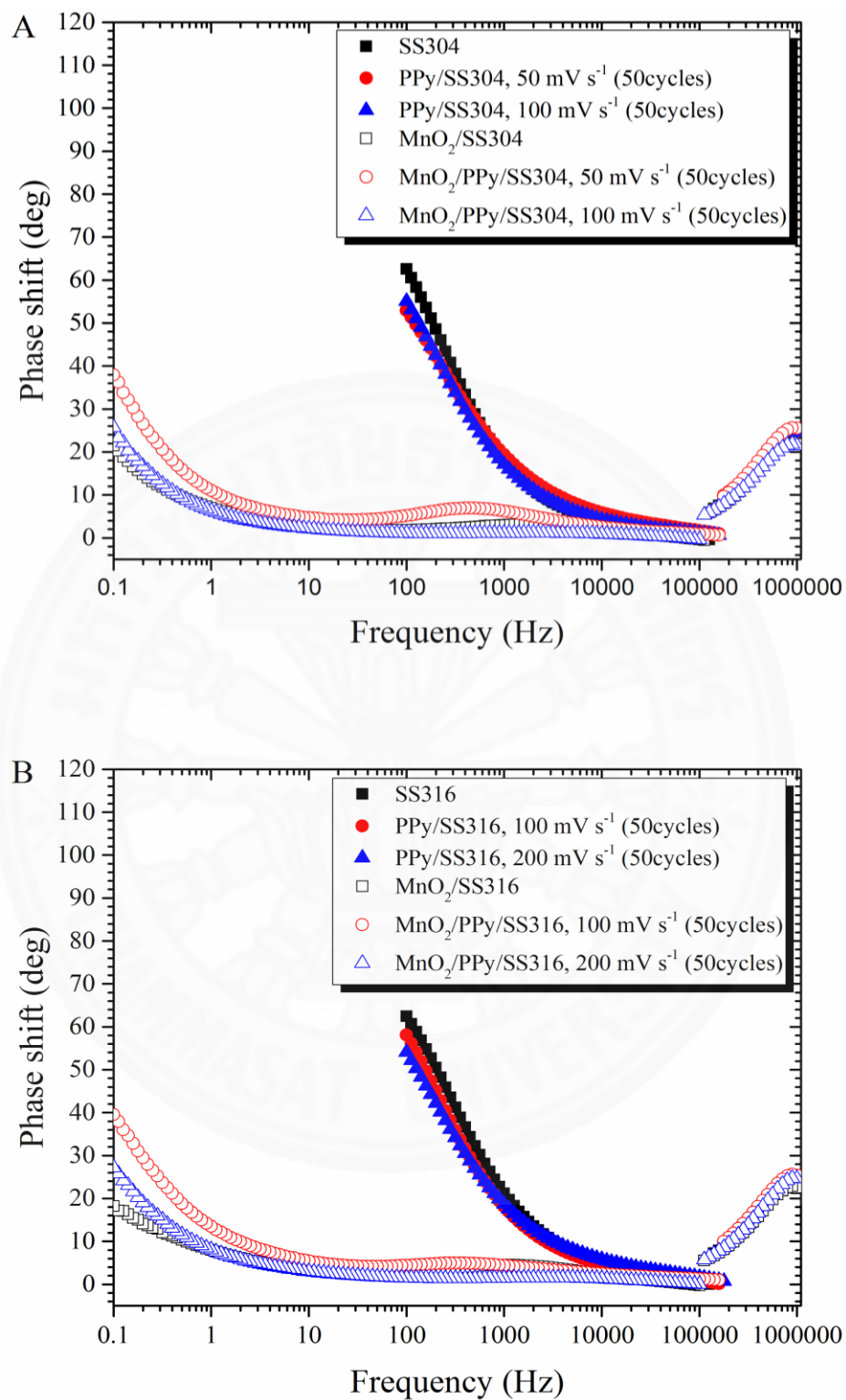


Fig. 4.31 Bode-phase plots of (A) SS 304 and (B) SS 316 electrode materials.

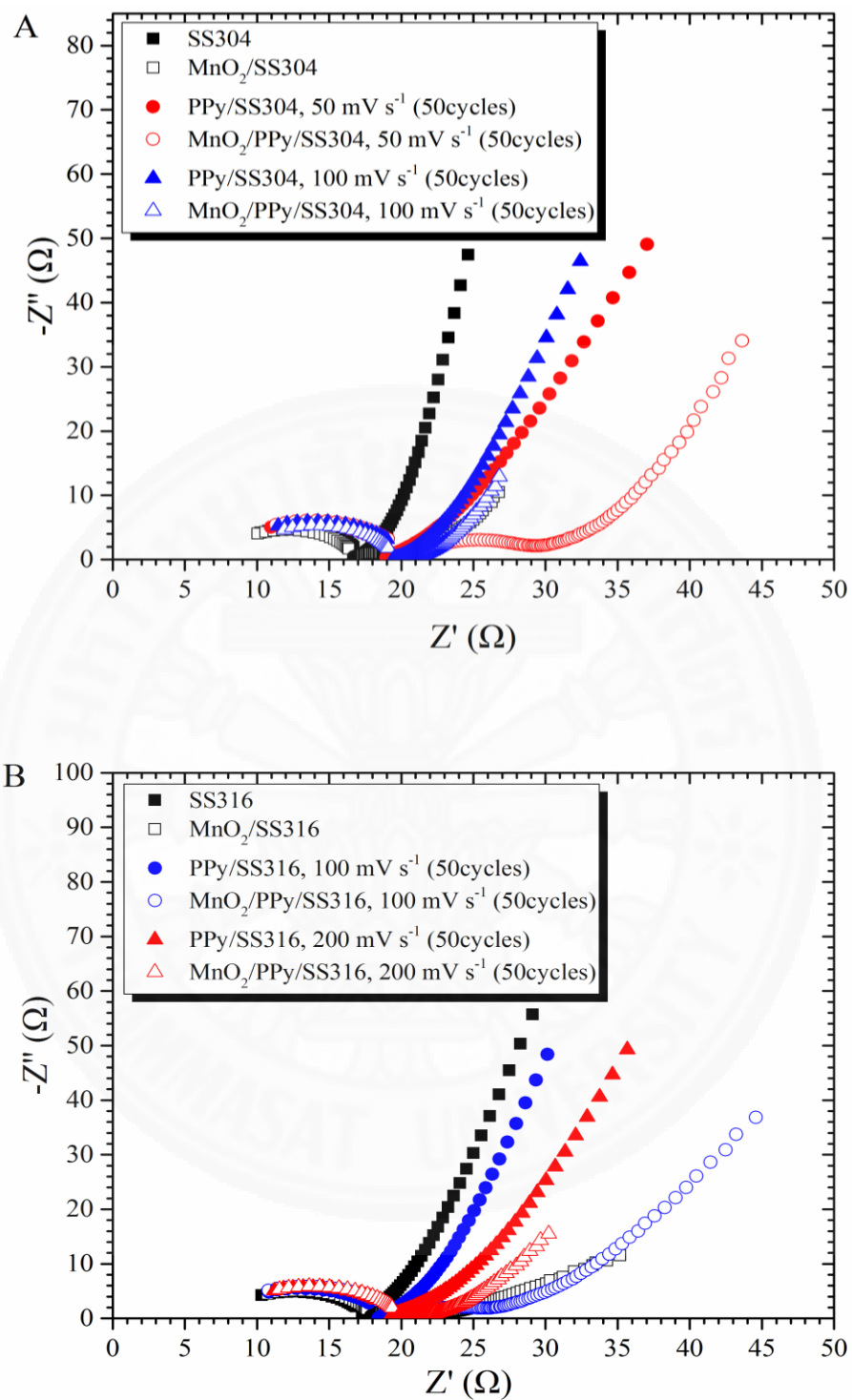


Fig. 4.32 Nyquist plots of (A) SS 304 and (B) SS 316 electrode materials in 0.1 M KCl solutions.

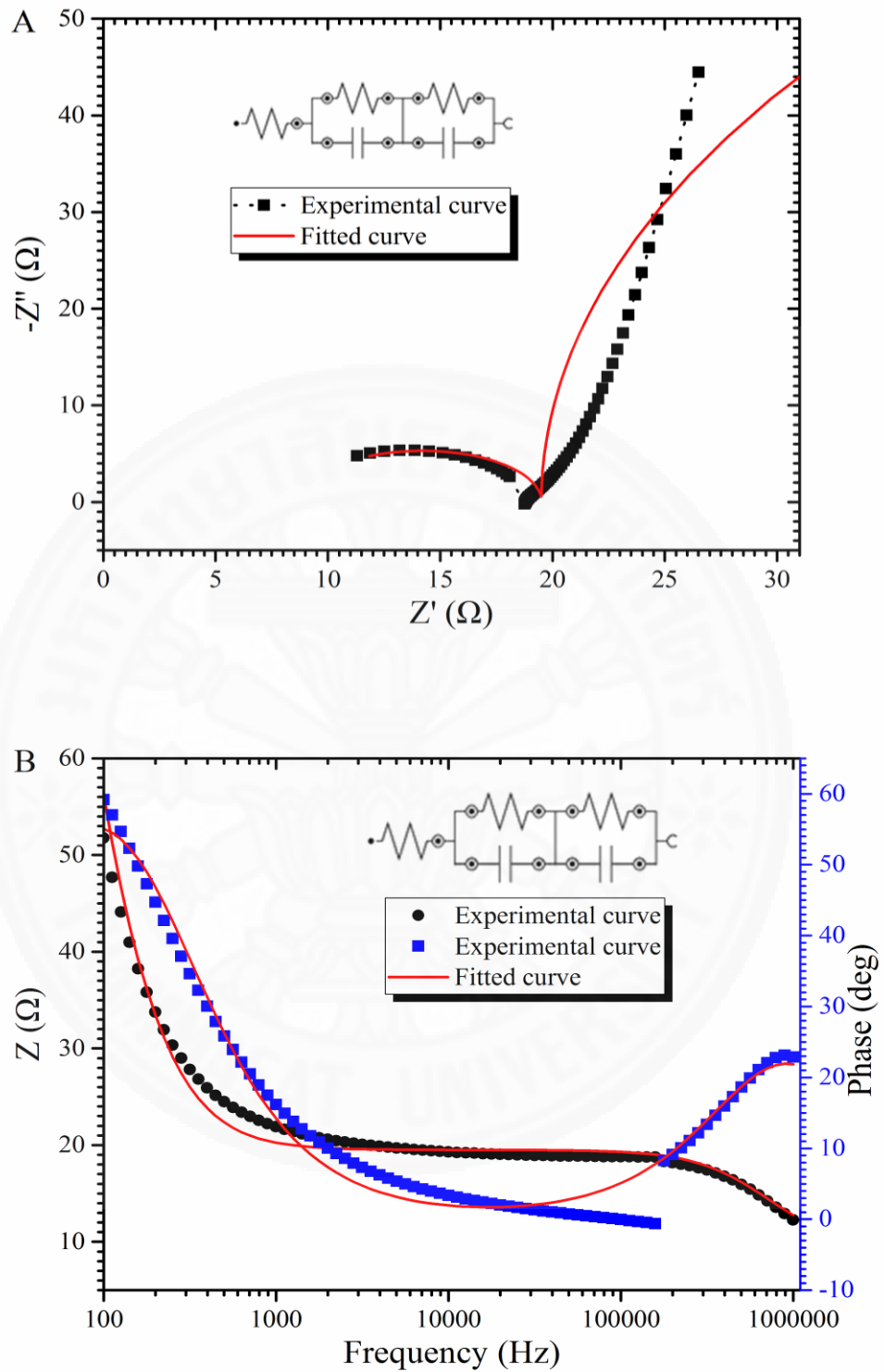


Fig. 4.33 Overlaid experimental and fitted (a) Nyquist plots and (b) Bode-phase plots with equivalent circuit elements of the bare SS 304 in 0.1M KCl solutions.

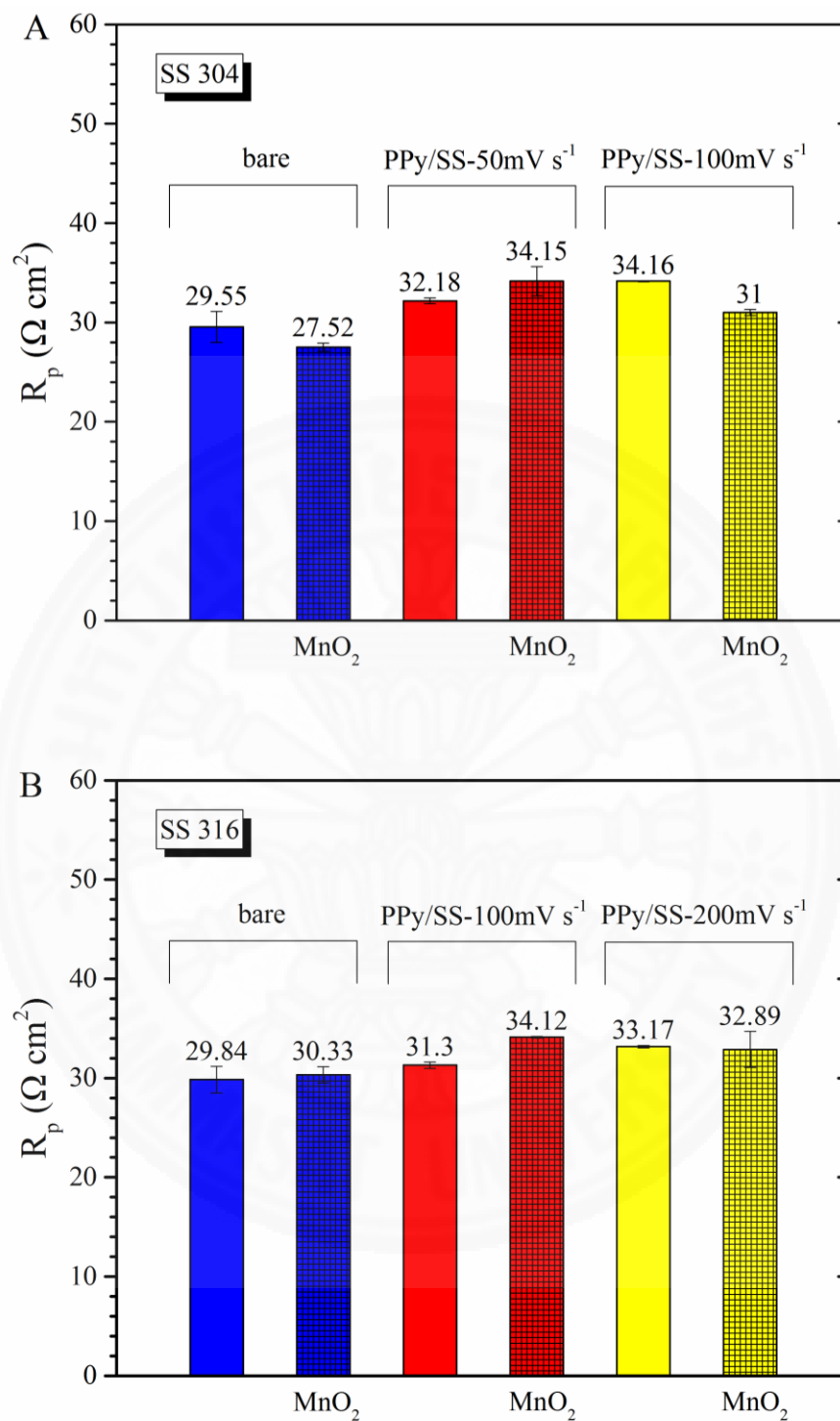


Fig. 4.34 The electrode material resistance of (A) SS 304 and (B) SS 316 in 0.1 KCl solutions.

Table 4.8A The passive film resistance of SS 304 electrodes in 0.1M KCl solutions.

Electrode materials	Resistance of the passive film ($\Omega \text{ cm}^2$)		
	Experimental	Fitted	Estimated Error (%)
Bare SS304	29.6 ± 1.6	30.2 ± 1.6	4.9 ± 0.1
PPy-coated SS304, 50mV/s, 50cycles	32.2 ± 0.3	33.9 ± 0.7	6.1 ± 0.2
PPy-coated SS304, 100mV/s, 50cycles	34.2 ± 0.1	35.5 ± 0.1	5.5 ± 0.2
MnO ₂ /Bare SS304	27.5 ± 0.4	28.0 ± 0.4	8.9 ± 0.2
MnO ₂ /PPy-coated SS304, 50mV/s, 50cycles	34.2 ± 1.5	34.9 ± 1.6	12.6 ± 03
MnO ₂ /PPy-coated SS304, 100mV/s, 50cycles	31.0 ± 0.3	31.6 ± 0.2	4.5 ± 0.1

Table 4.8B The passive film resistance of SS 316 electrodes in 0.1M KCl solutions.

Electrode materials	Resistance of the passive film ($\Omega \text{ cm}^2$)		
	Experimental	Fitted	Estimated Error (%)
Bare SS316	29.8 ± 1.3	30.6 ± 1.5	5.7 ± 0.2
PPy-coated SS316, 100mV/s, 50cycles	31.3 ± 0.3	32.2 ± 0.4	6.5 ± 0.8
PPy-coated SS316, 200mV/s, 50cycles	33.2 ± 0.1	34.7 ± 0.1	6.1 ± 0.3
MnO ₂ /Bare SS316	30.3 ± 0.8	31.0 ± 0.8	9.6 ± 0.1
MnO ₂ /PPy-coated SS316, 100mV/s, 50cycles	34.1 ± 0.1	36.7 ± 0.9	11.3 ± 3.5
MnO ₂ /PPy-coated SS316, 200mV/s, 50cycles	32.9 ± 1.8	33.7 ± 1.7	5.1 ± 0.2

Chapter 5

Conclusions and Recommendations

5.1 Conclusions

In order to improve power output in MFCs through modification of electrode materials. GAC and SS were modified with heat treatment under N₂ flow and Polypyrrole (PPy) coating respectively. Subsequently, MnO₂ catalyst was precipitated and electrodeposited on the heated GAC and PPy-coated SS respectively to promote electrochemical activities of the MFC system.

The surface area and pore volume of heated GAC had been improved. The micropore volume of GAC increased with increasing temperatures. They exhibited a maximum value at 600 °C for GAC (coal-based) and 800 °C for GAC (wood-based). BET results presented that heat treatment also plays an important role in increasing of the specific surface area. The best performance of heat treatment of GAC electrode materials was 600 and 800 °C. Therefore, the electrode modification to prepare large quantity of surface area and pore volume of GAC could be achieved using heat treatment at 600 °C and 800 °C for MnO₂ precipitation method.

After MnO₂ precipitation, SEM, XRD and EDX results confirmed that there are the needle-like morphologies of MnO₂ onto heated GAC surface. Modifying with heat treatment, the EAS values of heated GAC increased to 65 - 282%. Moreover, modifying with heat treatment and MnO₂ precipitation resulted in the EAS values increasing by 79 - 526% compared to the untreated GAC especially from MnO₂/GAC (coal-based) and MnO₂/GAC (wood-based) under 600 °C electrode materials. Also, the EIS results showed that the resistance of these electrode materials decreased when increasing in EAS values. It indicated that modifying with heat treatment and MnO₂ precipitation represent better surface area and micropore volume of electrode materials.

PPy film was electropolymerised on SS in order to increase the EAS values. Weight of PPy was found to be higher with the use of slow scan rate in electropolymerisation. Moreover, the globular morphology of PPy coated onto SS were also affected by potential scan rate; at the slow scan rate, the synthesised PPy film was more granular when compared to the fast scan of 400 mV s⁻¹. Thus, the EAS of

PPy-coated SS was maximised with the use of slow scan rates of 50 and 100 mVs⁻¹ for SS 304 and 100 and 200 mVs⁻¹ for SS 316 mesh. Therefore, the electrode modification to prepare large quantity and high quality of PPy film could be achieved using the slower scan rates of 50, 100 and 200 mVs⁻¹ under 50 cycles of electropolymerisation.

The electrodeposited film of MnO₂ onto PPy-coated SS possessed greater surface area in relation to the polypyrrole films prepared on SS surface. From FT-IR, XRD and EDX results, they are conformed that there are formation of PPy film and hydrated MnO₂. CV experiments reveal that the EAS values of MnO₂/PPy-coated SS 304 at 100 mV s⁻¹ under 50 cycles and MnO₂/PPy-coated SS 316 at 200 mV s⁻¹ under 50 cycles were higher by about 2,368% and 3,594% respectively due to the effect of PPy film and MnO₂ nanostructure. Also, the EIS results showed that the ohmic resistance of these electrode materials decreased when increasing in EAS values. It has been found that these SS electrode materials are the optimum conditions for obtaining maximum electrochemical activities.

5.2 Recommendations

5.2.1 Each GAC has irregular shape. Also, the weight of them is not equal so it is difficult to compare the BET surface are or other parameters but we can test it before and after of the same sample.

5.2.2 PPy film can be peeled off due to the use of acidic solution in MnO₂ electrodeposition. The use of low acidic concentration will be more suitable.

5.2.3 Pyrrole solution is easier to oxidise. So we should flow N₂ gas in the solution before keep it in sealed-container.

References

1. You, J., et al., *Stability and reliability of anodic biofilms under different feedstock conditions: Towards microbial fuel cell sensors*. Sensing and Bio-Sensing Research, 2015. **6**: p. 43-50.
2. Zhou, M., et al., *An overview of electrode materials in microbial fuel cells*. Journal of Power Sources, 2011. **196**(10): p. 4427-4435.
3. Suhasini, *Effect of deposition method and the surfactant on high capacitance of electrochemically deposited MnO₂ on stainless steel substrate*. Journal of Electroanalytical Chemistry, 2013. **690**: p. 13-18.
4. Wang, Y. and D.O. Northwood, *An investigation into polypyrrole-coated 316L stainless steel as a bipolar plate material for PEM fuel cells*. Journal of Power Sources, 2006. **163**(1): p. 500-508.
5. Li, Y., et al., *PPy/AQS (9, 10-anthraquinone-2-sulfonic acid) and PPy/ARS (Alizarin Red's) modified stainless steel mesh as cathode membrane in an integrated MBR/MFC system*. Desalination, 2014. **349**: p. 94-101.
6. Tüken, T., *Polypyrrole films on stainless steel*. Surface and Coatings Technology, 2006. **200**(16–17): p. 4713-4719.
7. Liu, X.-W., W.-W. Li, and H.-Q. Yu, *Cathodic catalysts in bioelectrochemical systems for energy recovery from wastewater*. Chemical Society Reviews, 2014. **43**(22): p. 7718-7745.
8. Pan, N., et al., *Preparation of graphene oxide-manganese dioxide for highly efficient adsorption and separation of Th(IV)/U(VI)*. Journal of Hazardous Materials, 2016. **309**: p. 107-115.
9. Logan, B.E., et al., *Microbial Fuel Cells: Methodology and Technology*. Environmental Science & Technology, 2006. **40**(17): p. 5181-5192.
10. Chouler, J. and M. Di Lorenzo, *Water Quality Monitoring in Developing Countries; Can Microbial Fuel Cells be the Answer?* Biosensors, 2015. **5**(3): p. 450.
11. Logan, B.E. and J.M. Regan, *Microbial fuel cells-challenges and applications*. Environ Sci Technol, 2006. **40**(17): p. 5172-80.

12. Du, Z., H. Li, and T. Gu, *A state of the art review on microbial fuel cells: A promising technology for wastewater treatment and bioenergy*. *Biotechnology Advances*, 2007. **25**(5): p. 464-482.
13. Sourish Karmakar, K.K.a.S.K., *Design and Development of Microbial Fuel cells* Current Research, Technology and Education Topics in Applied Microbial Biotechnology, 2010: p. 1029-1034.
14. Mahadevan, A., D.A. Gunawardena, and S. Fernando, *Biochemical and Electrochemical Perspectives of the Anode of a Microbial Fuel Cell*. *Technology and Application of Microbial Fuel Cells*. 2014.
15. Schroder, U., J. Niessen, and F. Scholz, *A generation of microbial fuel cells with current outputs boosted by more than one order of magnitude*. *Angew Chem Int Ed Engl*, 2003. **42**(25): p. 2880-3.
16. Park, D.H. and J.G. Zeikus, *Improved fuel cell and electrode designs for producing electricity from microbial degradation*. *Biotechnology and Bioengineering*, 2003. **81**(3): p. 348-355.
17. Rhoads, A., H. Beyenal, and Z. Lewandowski, *Microbial Fuel Cell using Anaerobic Respiration as an Anodic Reaction and Biomineralized Manganese as a Cathodic Reactant*. *Environmental Science & Technology*, 2005. **39**(12): p. 4666-4671.
18. Rahimnejad, M., et al., *Microbial fuel cell as new technology for bioelectricity generation: A review*. *Alexandria Engineering Journal*, 2015. **54**(3): p. 745-756.
19. Jiang, D. and B. Li, *Granular activated carbon single-chamber microbial fuel cells (GAC-SCMFCs): A design suitable for large-scale wastewater treatment processes*. *Biochemical Engineering Journal*, 2009. **47**(1-3): p. 31-37.
20. Donaldson, K., et al., *Carbon nanotubes: a review of their properties in relation to pulmonary toxicology and workplace safety*. *Toxicol Sci*, 2006. **92**(1): p. 5-22.
21. Dumas, C., et al., *Marine microbial fuel cell: Use of stainless steel electrodes as anode and cathode materials*. *Electrochimica Acta*, 2007. **53**(2): p. 468-473.
22. Richter, H., et al., *Electricity generation by Geobacter sulfurreducens attached to gold electrodes*. *Langmuir*, 2008. **24**(8): p. 4376-9.

23. Manohar, A.K. and F. Mansfeld, *The internal resistance of a microbial fuel cell and its dependence on cell design and operating conditions*. *Electrochimica Acta*, 2009. **54**(6): p. 1664-1670.
24. Yin, C.Y., M.K. Aroua, and W.M.A.W. Daud, *Review of modifications of activated carbon for enhancing contaminant uptakes from aqueous solutions*. *Separation and Purification Technology*, 2007. **52**(3): p. 403-415.
25. Mohammad Saleh Shafeeyan, W.M.A.W.D., Amirhossein Houshmand, Ahmad Shamiri, *A review on surface modification of activated carbon for carbon dioxide adsorption*. *Analytical and Applied Pyrolysis*, 2010. **89**: p. 143-151.
26. Ohtsuka, T., *Corrosion protection of steels by conducting polymer coating*. *International Journal of Corrosion*, 2012: p. 1-7.
27. Wessling, B., *Passivation of metals by coating with polyaniline: corrosion potential shift*. *Advanced Materials*, 1994. **6**(3): p. 226 - 228.
28. Zou, Y., et al., *A mediatorless microbial fuel cell using polypyrrole coated carbon nanotubes composite as anode material*. *International Journal of Hydrogen Energy*, 2008. **33**(18): p. 4856-4862.
29. Tsai, H.-Y., et al., *Microbial fuel cell performance of multiwall carbon nanotubes on carbon cloth as electrodes*. *Journal of Power Sources*, 2009. **194**(1): p. 199-205.
30. Mustakeem, *Electrode materials for microbial fuel cells: nanomaterial approach*. *Materials for Renewable and Sustainable Energy*, 2015. **4**(4): p. 22.
31. Choi, B., et al., *Fibrous MnO₂ electrode electrodeposited on carbon fiber for a fuel cell/battery system*. *Electrochimica Acta*, 2011. **56**(19): p. 6696-6701.
32. Ben Liew, K., et al., *Non-Pt catalyst as oxygen reduction reaction in microbial fuel cells: A review*. *International Journal of Hydrogen Energy*, 2014. **39**(10): p. 4870-4883.
33. Jackson, A.W.B.a.B.P., *Study of Ferricyanide by Cyclic Voltammetry using the CV-50W*. *Current Separation*, 1996. **15**: p. 25-30.
34. McDuffie, S.J.K.a.B., *Diffusion coefficients of ferri- and ferrocyanide ions in aqueous media using twin-electrode thin-layer electrochemistry*. *Analytical chemistry*, 1970. **42**(14): p. 1741-1746.

35. Abdul Halim Abdullah, A.K., Zulkarnain Zainal, Mohd Zobir Hussien, Dzulkefly Kuang, Faujan Ahmad and Ong Sim Wooi, *Preparation and Characterization of Activated Carbon from Gelam Wood Bark (Melaleuca cajuputi)*. Malaysian Journal of Analytical Sciences, 2001. **7**(1): p. 65-68.
36. Lowell, S., et al., *Surface Area Analysis from the Langmuir and BET Theories, in Characterization of Porous Solids and Powders: Surface Area, Pore Size and Density*. 2004, Springer Netherlands: Dordrecht. p. 58-81.
37. Scott, K., et al., *Application of Modified Carbon Anodes in Microbial Fuel Cells*. Process Safety and Environmental Protection, 2007. **85**(5): p. 481-488.
38. Aljundi, I.H. and S.K. Al-Dawery, *Equilibrium and thermodynamic study of cobalt adsorption on activated carbon derived from date seeds*. Desalination and Water Treatment, 2014. **52**(25-27): p. 4830-4836.
39. Wang, Z., M. Zhong, and L. Chen, *Coal-based granular activated carbon loaded with MnO₂ as an efficient adsorbent for removing formaldehyde from aqueous solution*. Desalination and Water Treatment, 2016. **57**(28): p. 13225-13235.
40. Jackson, A.W.B.a.B.P., *Study of Ferricyanide by Cyclic Voltammetry using the CV-50W*. Current Separation 1996. **15**(1): p. 25-30.
41. Lu, Z., et al., *Biological capacitance studies of anodes in microbial fuel cells using electrochemical impedance spectroscopy*. Bioprocess Biosyst Eng, 2015. **38**(7): p. 1325-33.
42. Özyılmaz, A.T., M. Erbil, and B. Yazıcı, *The electrochemical synthesis of polyaniline on stainless steel and its corrosion performance*. Current Applied Physics, 2006. **6**(1): p. 1-9.
43. Broughton, J.N. and M.J. Brett, *Variations in MnO₂ electrodeposition for electrochemical capacitors*. Electrochimica Acta, 2005. **50**(24): p. 4814-4819.
44. J.V. Thombare, M.C.R., S.H. Han and V.J. Fulari, *Synthesis of hydrophilic polypyrrole thin films by silar method*. Materials Physics and Mechanics, 2013. **16**: p. 118-125.
45. Saville, P., *Polypyrrole: Formation and use*. Vol. 004. 2005, Canada: DRDC Atlantic TM

46. Feng, Z., et al., *Passivity of 316L stainless steel in borate buffer solution studied by Mott–Schottky analysis, atomic absorption spectrometry and X-ray photoelectron spectroscopy*. *Corrosion Science*, 2010. **52**(11): p. 3646-3653.
47. Feng, Z., et al., *Effects of dissolved oxygen on electrochemical and semiconductor properties of 316L stainless steel*. *Journal of Nuclear Materials*, 2010. **407**(3): p. 171-177.





Appendices

Appendix A

The photographs of SS electrode materials

Table A-1 The photographs of SS 304 and PPy-coated SS 304 at various scan rates and cycles.

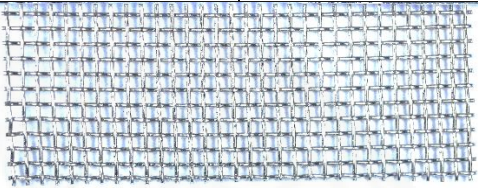
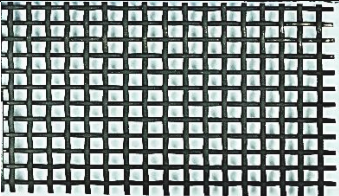
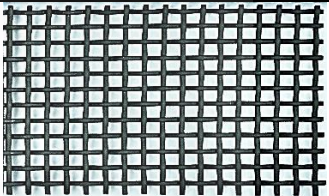
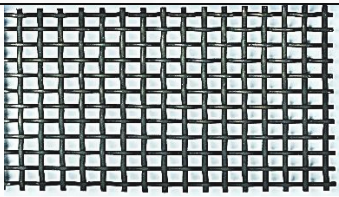
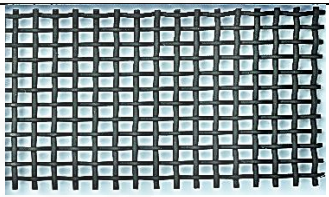
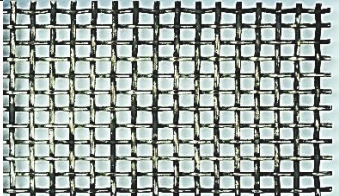
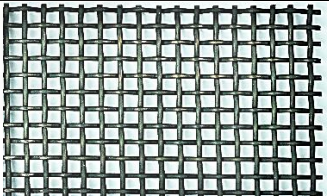
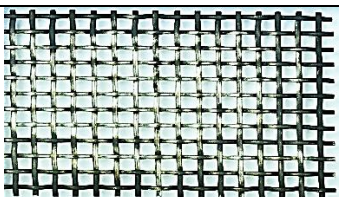
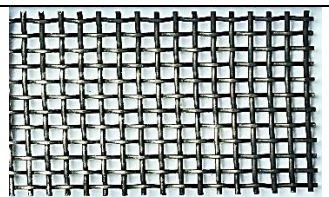

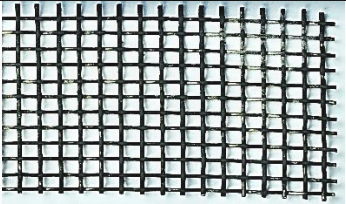
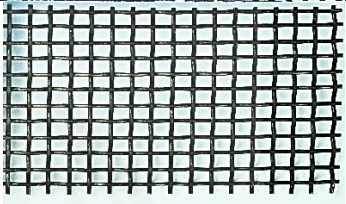
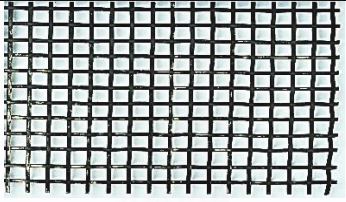
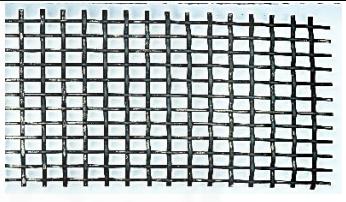
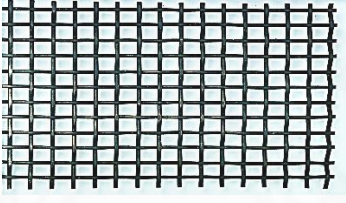
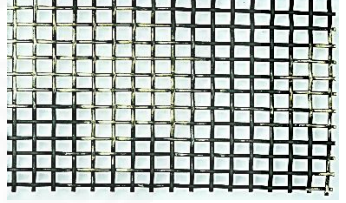
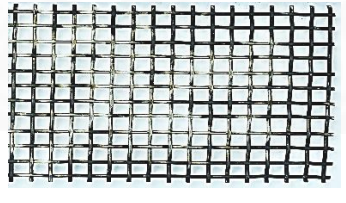
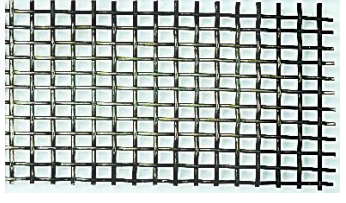
Electrode materials	50 cycles	100 cycles
Bare SS 304		
PPy-coated SS 304, 50 mV s ⁻¹		
PPy-coated SS 304, 100 mV s ⁻¹		
PPy-coated SS 304, 200 mV s ⁻¹		
PPy-coated SS 304, 400 mV s ⁻¹		

Table A-2 The photographs of SS 316 and PPy-coated SS 316 at various scan rates and cycles.

Electrode materials	50 cycles	100 cycles
Bare SS 316		
PPy-coated SS 316, 50 mV s ⁻¹		
PPy-coated SS 316, 100 mV s ⁻¹		
PPy-coated SS 316, 200 mV s ⁻¹		
PPy-coated SS 316, 400 mV s ⁻¹		

Appendix B

The elemental distribution on electrode surface

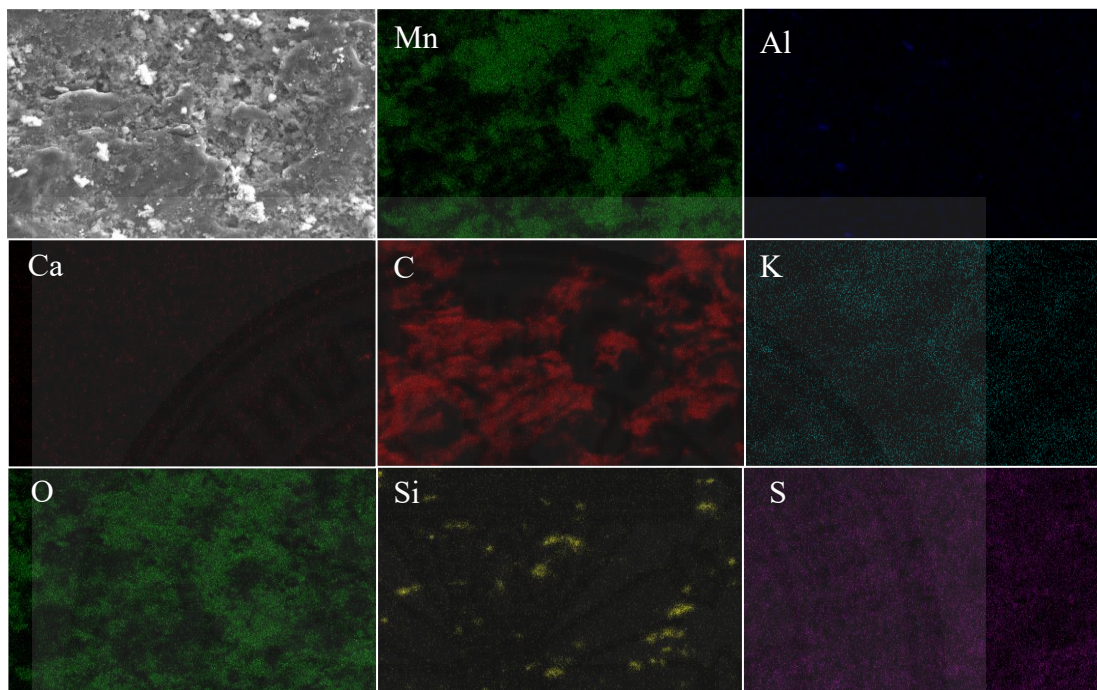


Fig. B-1 SEM image at 500 magnification and elemental distribution of MnO₂/GAC (coal-based) electrode.

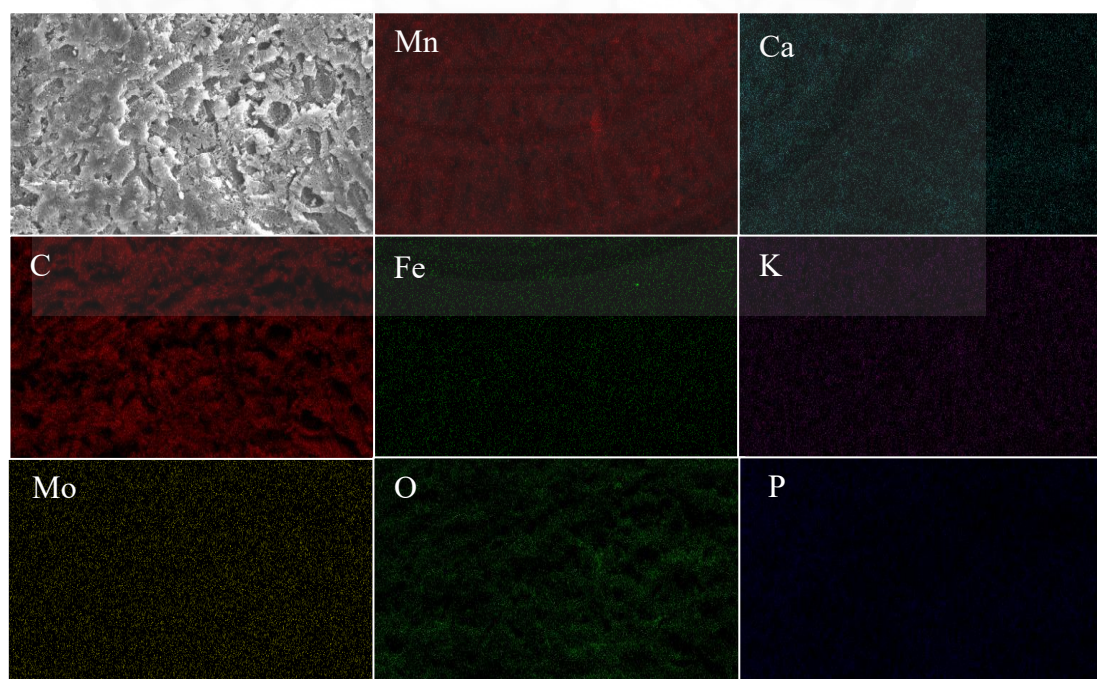


Fig. B-2 SEM image at 500 magnification and elemental distribution of MnO₂/GAC (wood-based) electrode.

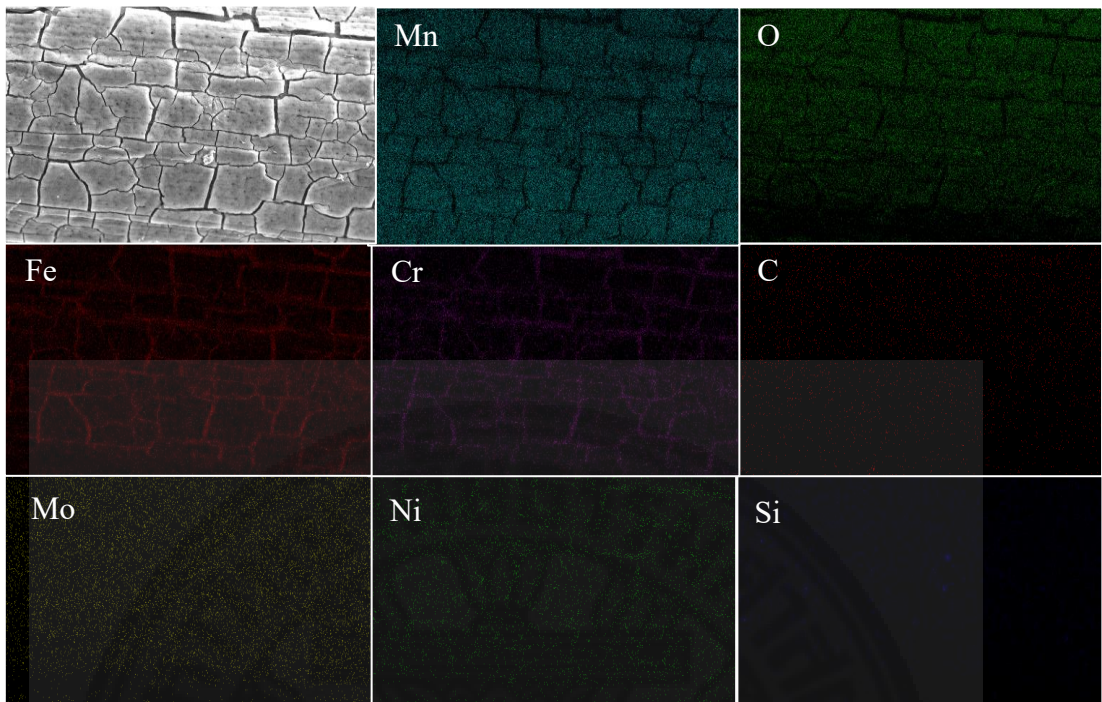


Fig. B-3 SEM image at 500 magnification and elemental distribution of MnO₂/SS 304 electrode.

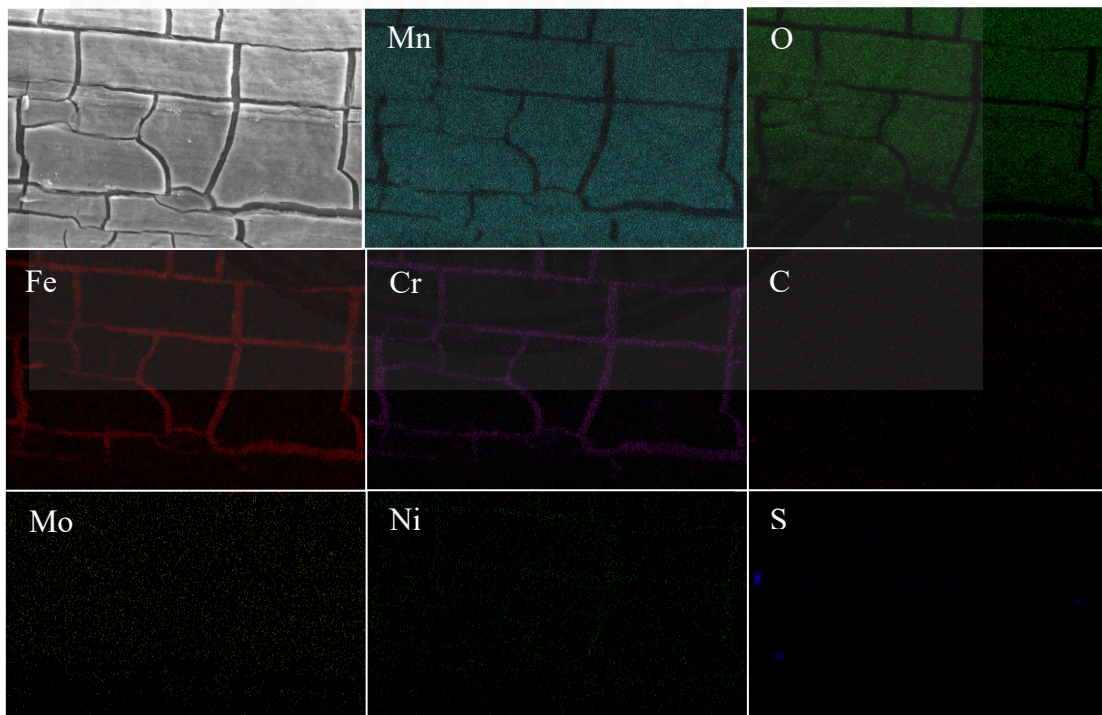


Fig. B-4 SEM image at 500 magnification and elemental distribution of MnO₂/SS 316 electrode.

Appendix C

Peak library of XRD

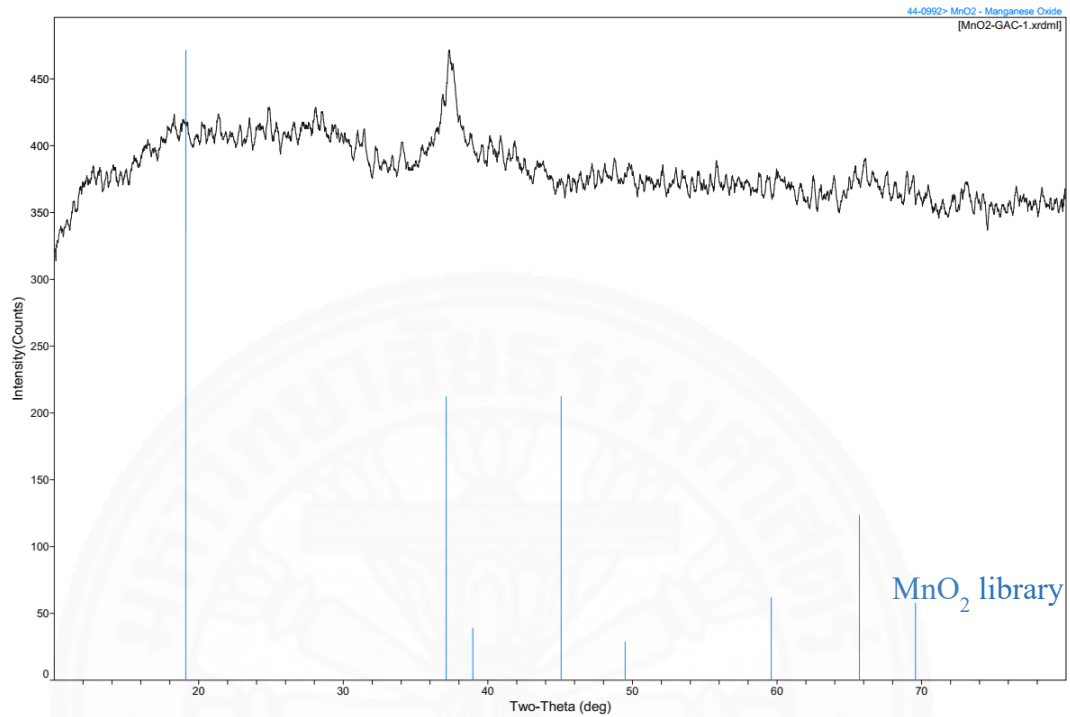


Fig C-1 XRD library of MnO₂ sediment.

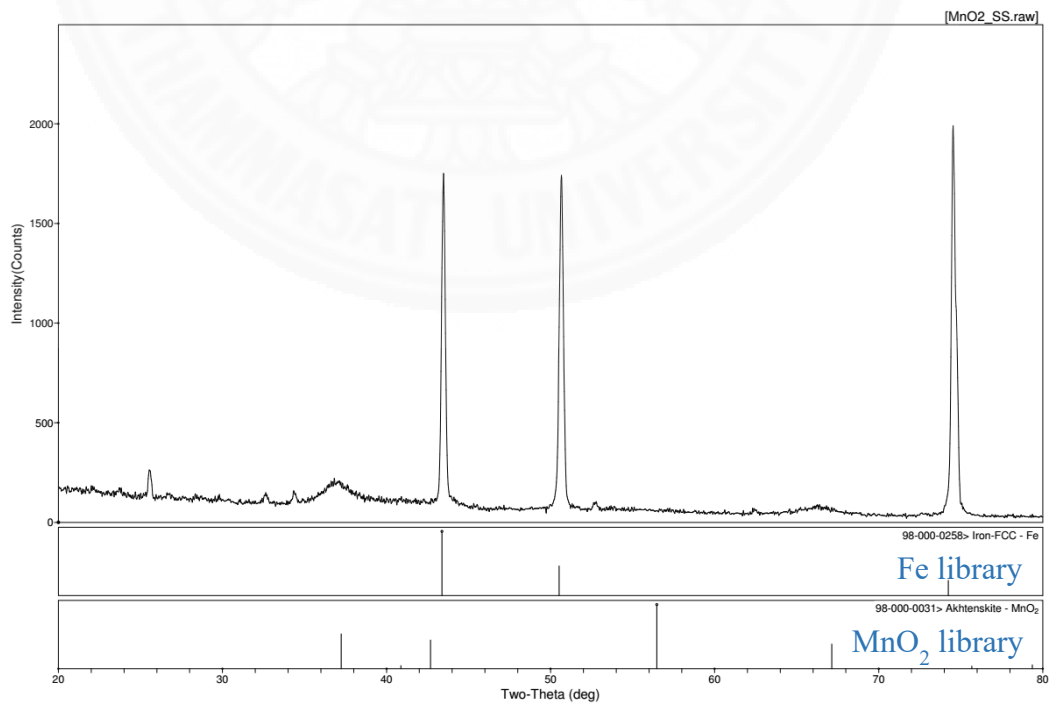


Fig C-2 XRD library of MnO₂ deposited on the SS surface.

Appendix D

CV of electrode materials

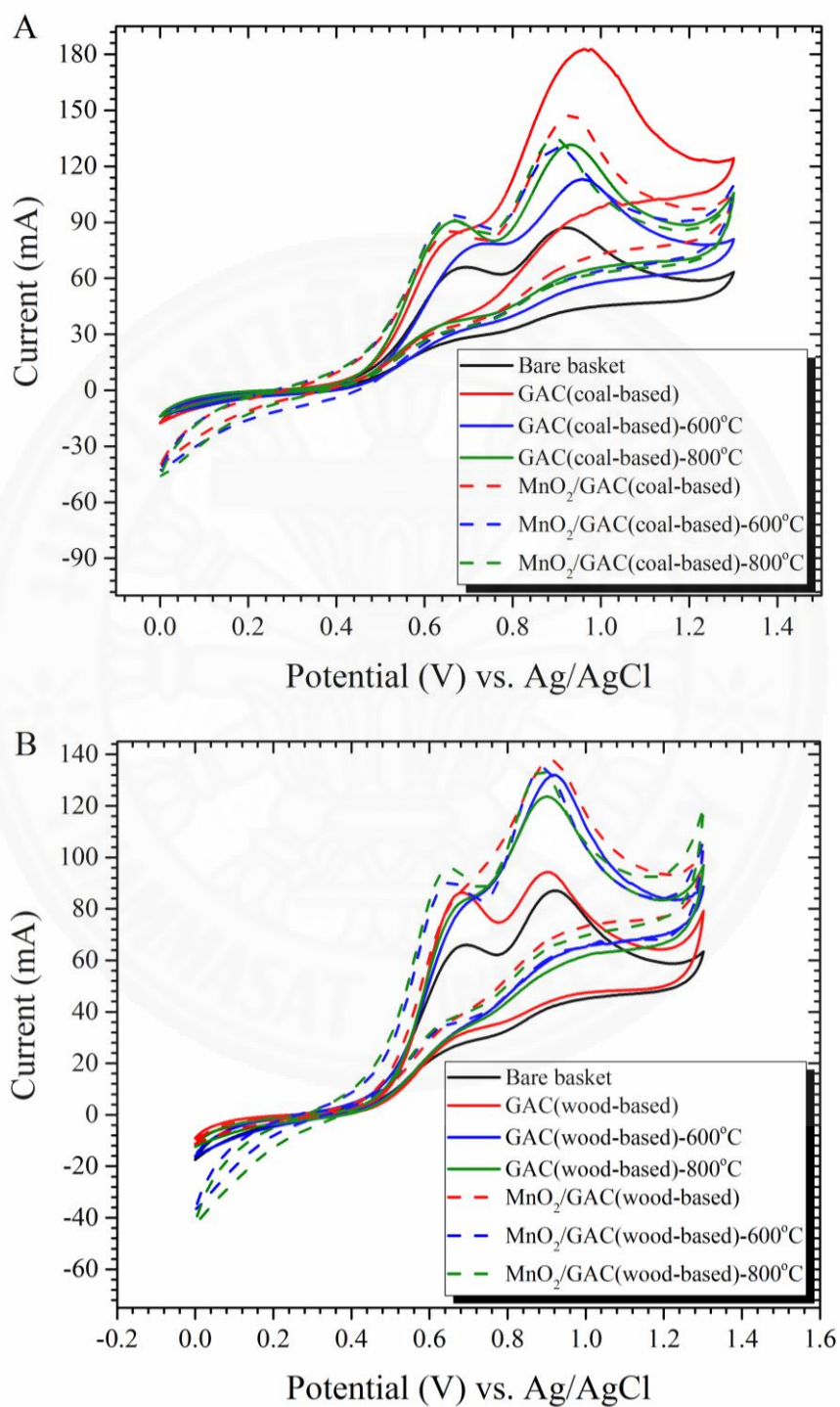


Fig. D-1 CV of 10 mM K₄Fe(CN)₆ in 1.0 M KNO₃ solution recorded at various (A) GAC (coal-based) and (B) GAC (wood-based) electrode materials at the same potential scan rate of 50 mV s⁻¹.

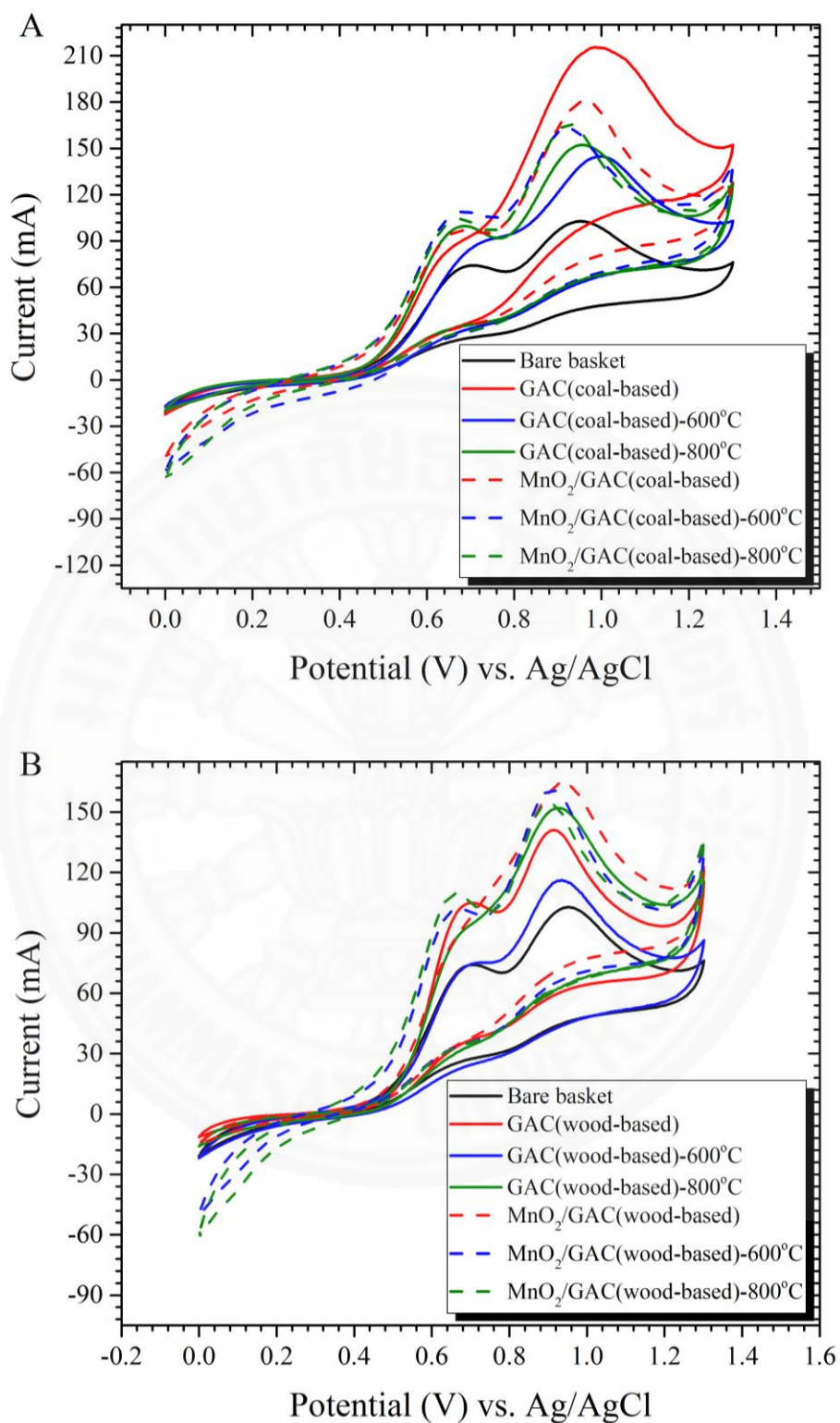


Fig. D-2 CV of 10 mM $K_4Fe(CN)_6$ in 1.0 M KNO_3 solution recorded at various (A) GAC (coal-based) and (B) GAC (wood-based) electrode materials at the same potential scan rate of 100 mV s^{-1} .

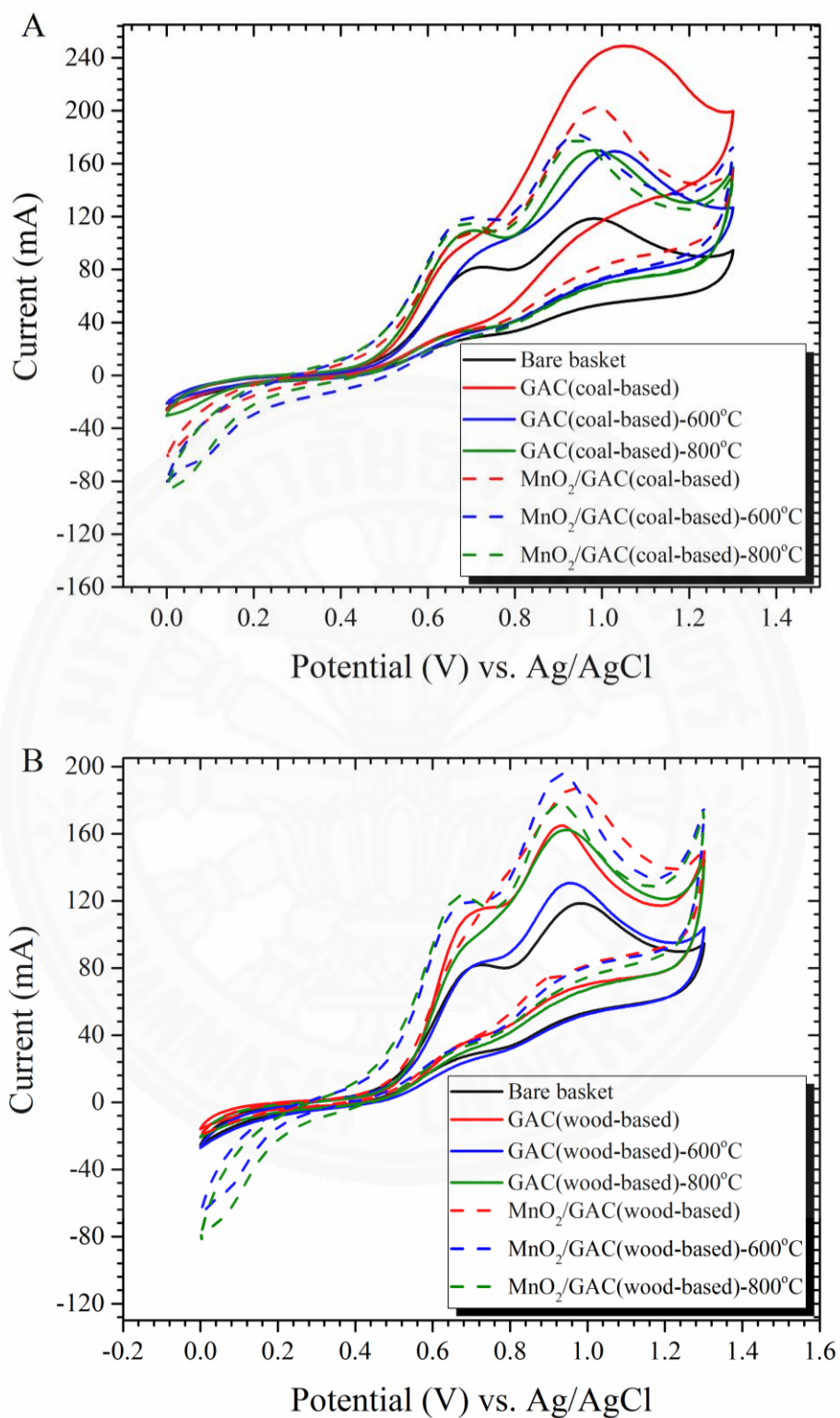


Fig. D-3 CV of 10 mM $K_4Fe(CN)_6$ in 1.0 M KNO_3 solution recorded at various (A) GAC (coal-based) and (B) GAC (wood-based) electrode materials at the same potential scan rate of 200 mV s^{-1} .

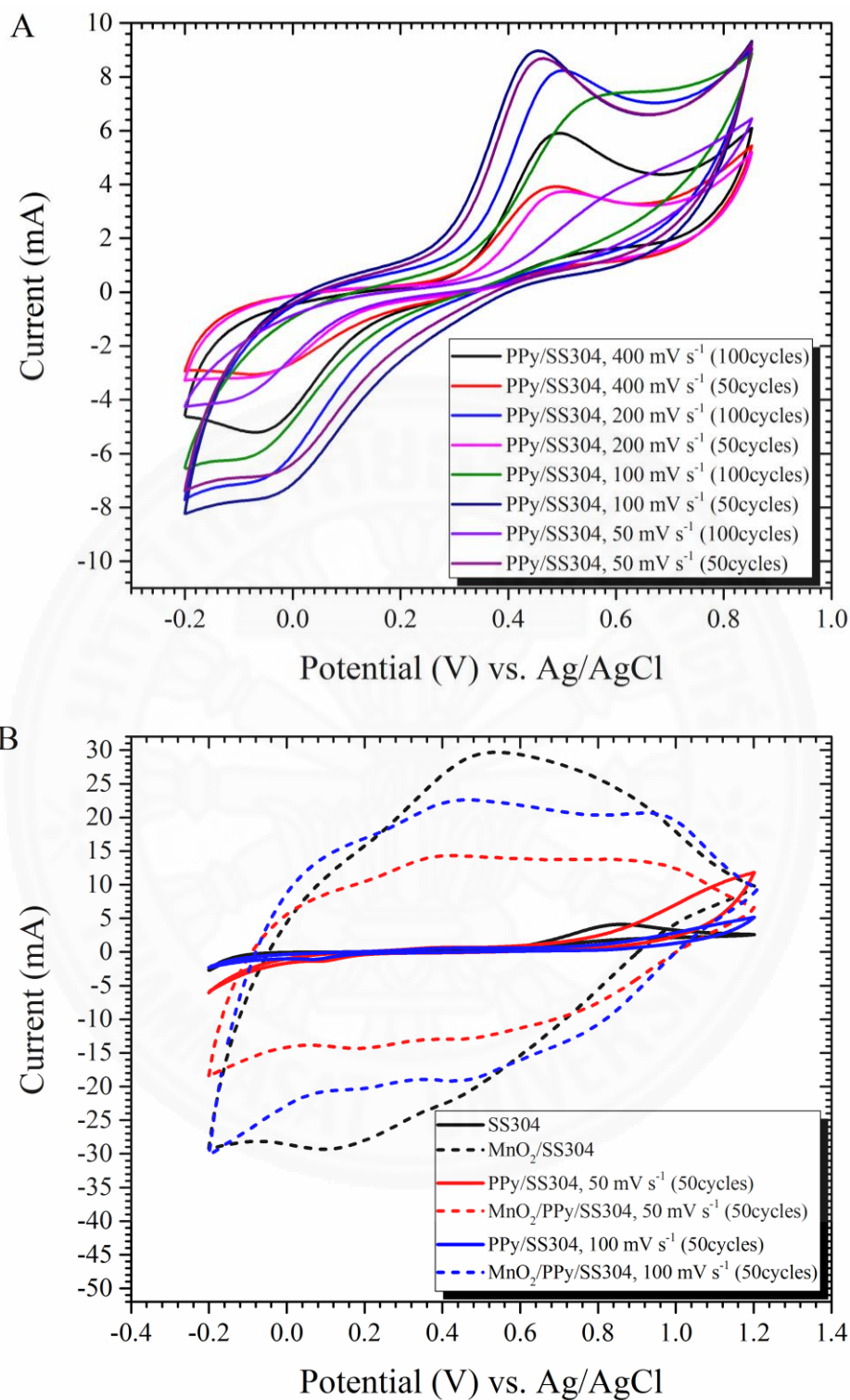


Fig. D-4 CV of 10 mM $K_4Fe(CN)_6$ in 1.0 M KNO_3 solution recorded at various SS 304 electrodes at the same potential scan rate of 50 mV s^{-1} .

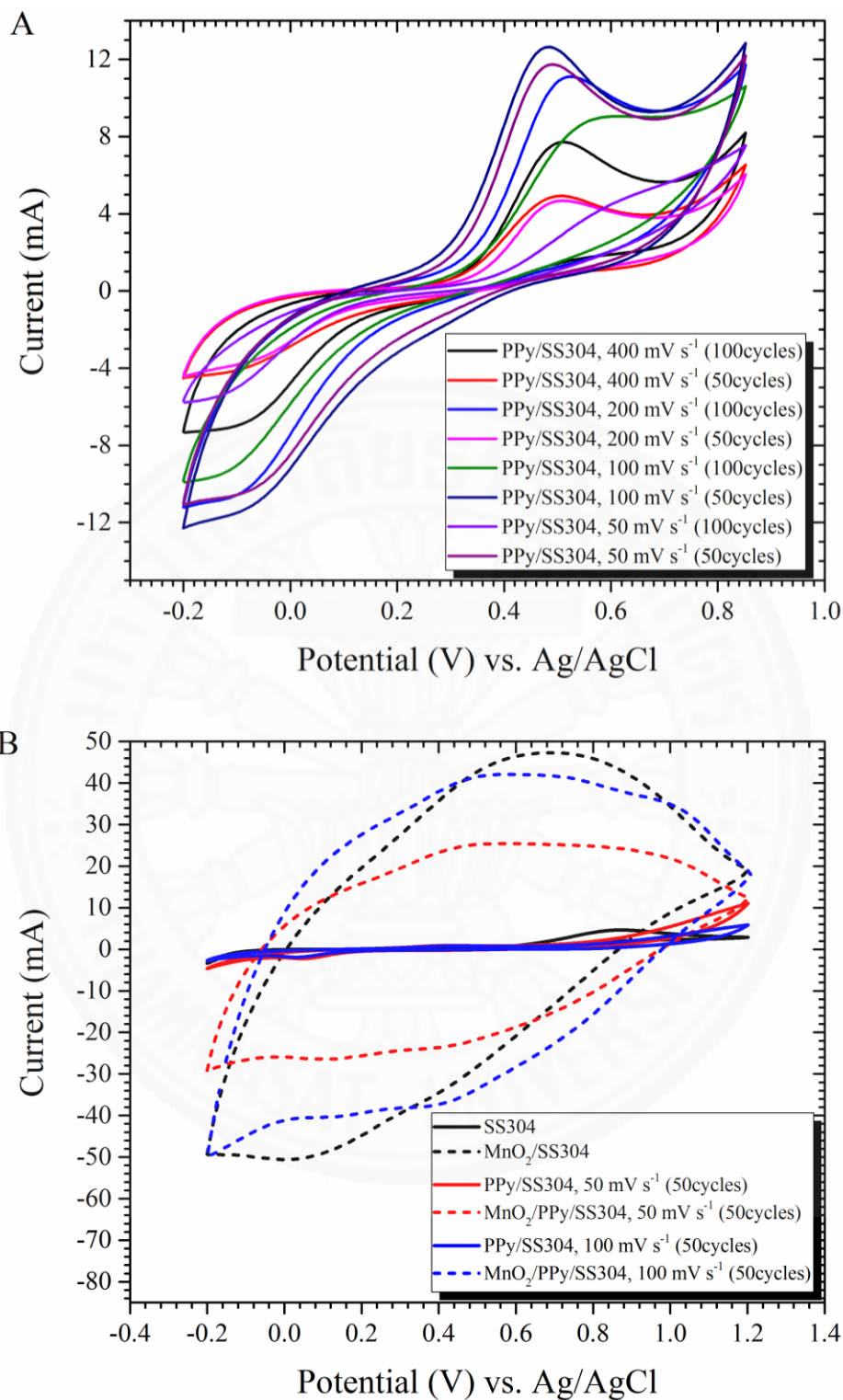


Fig. D-5 CV of 10 mM $K_4Fe(CN)_6$ in 1.0 M KNO_3 solution recorded at various SS 304 electrodes at the same potential scan rate of 100 mV s^{-1} .

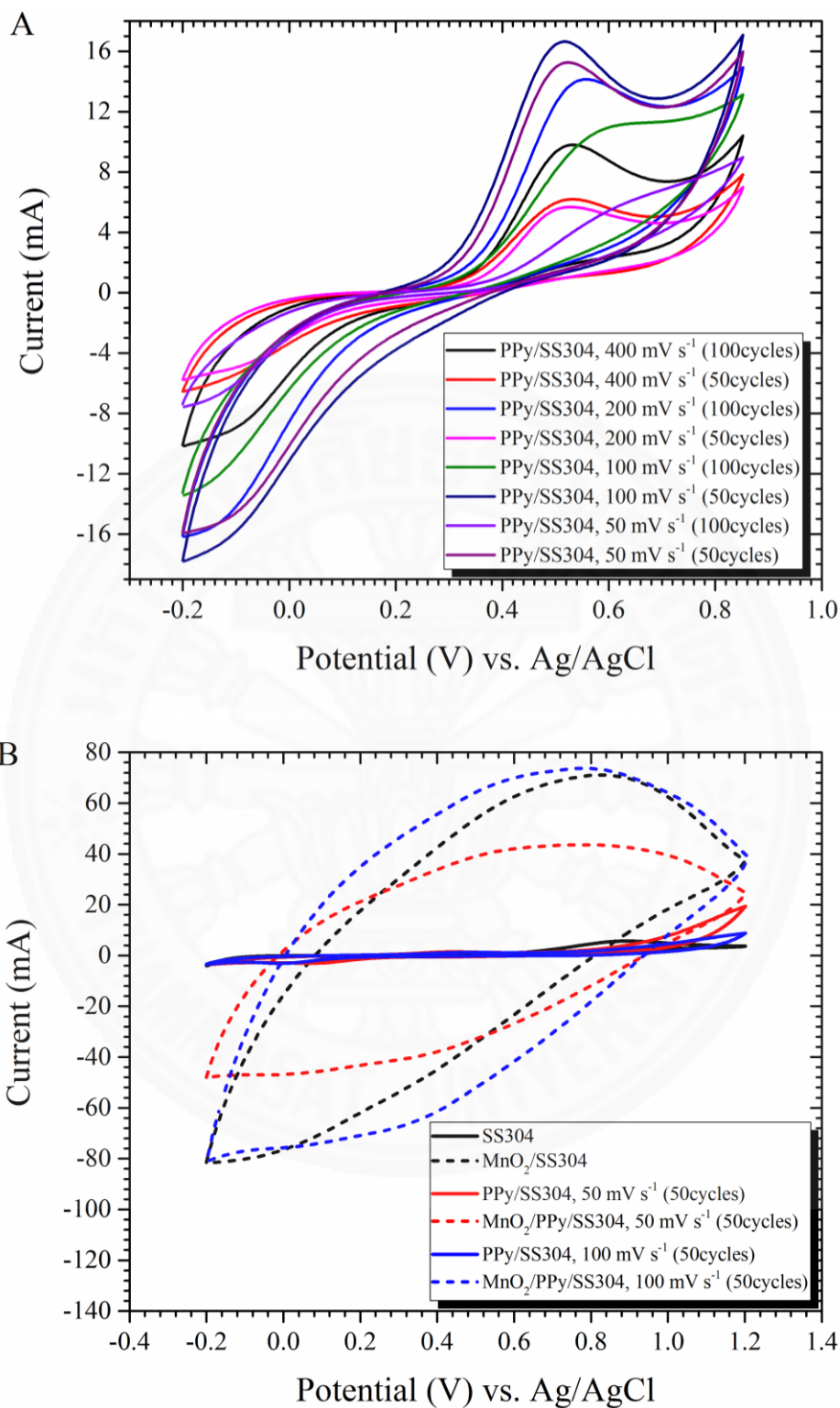


Fig. D-6 CV of 10 mM $K_4Fe(CN)_6$ in 1.0 M KNO_3 solution recorded at various SS 304 electrodes at the same potential scan rate of 200 mV s⁻¹.

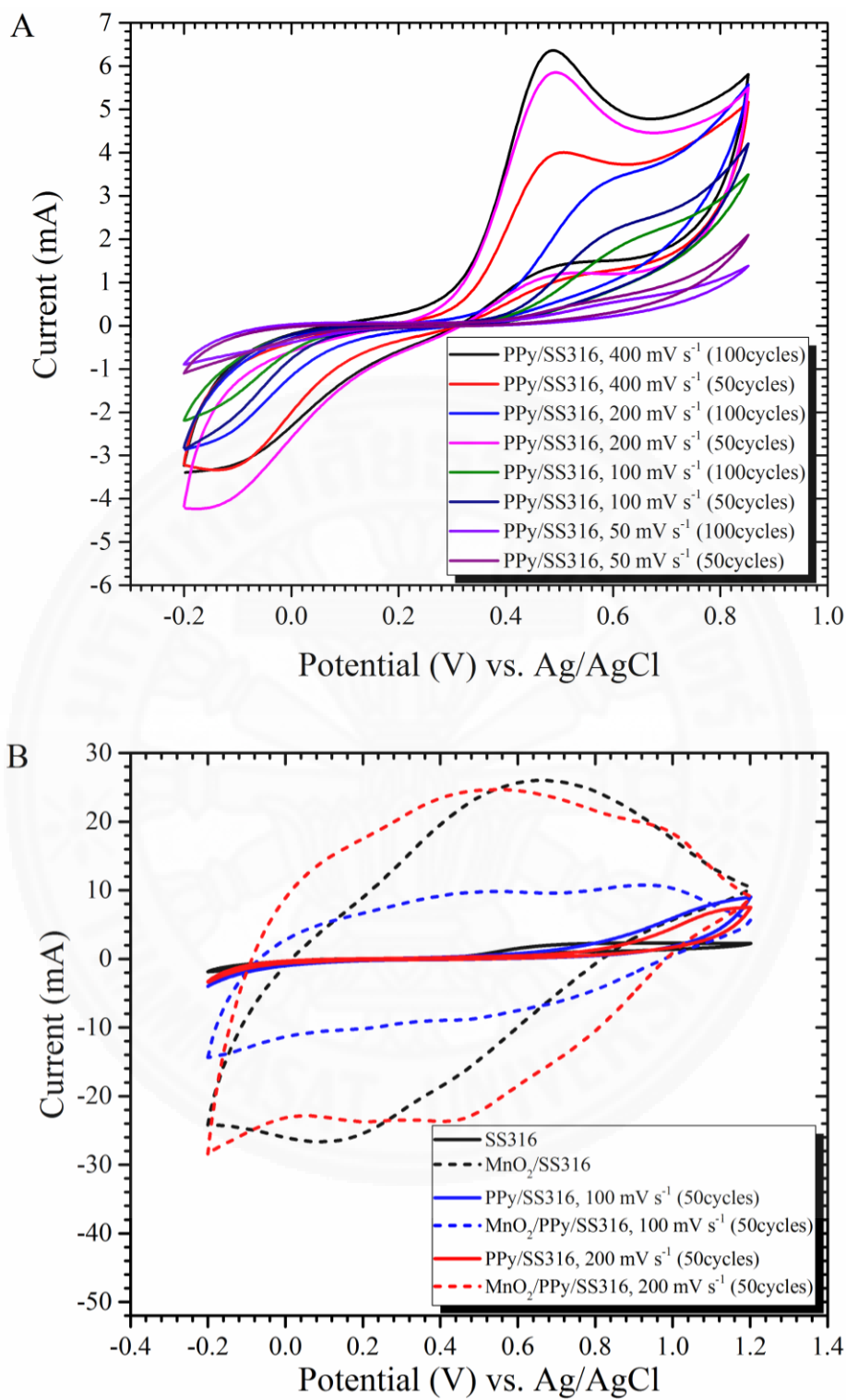


Fig. D-7 CV of 10 mM $K_4Fe(CN)_6$ in 1.0 M KNO_3 solution recorded at various SS 316 electrodes at the same potential scan rate of 50 mV s^{-1} .

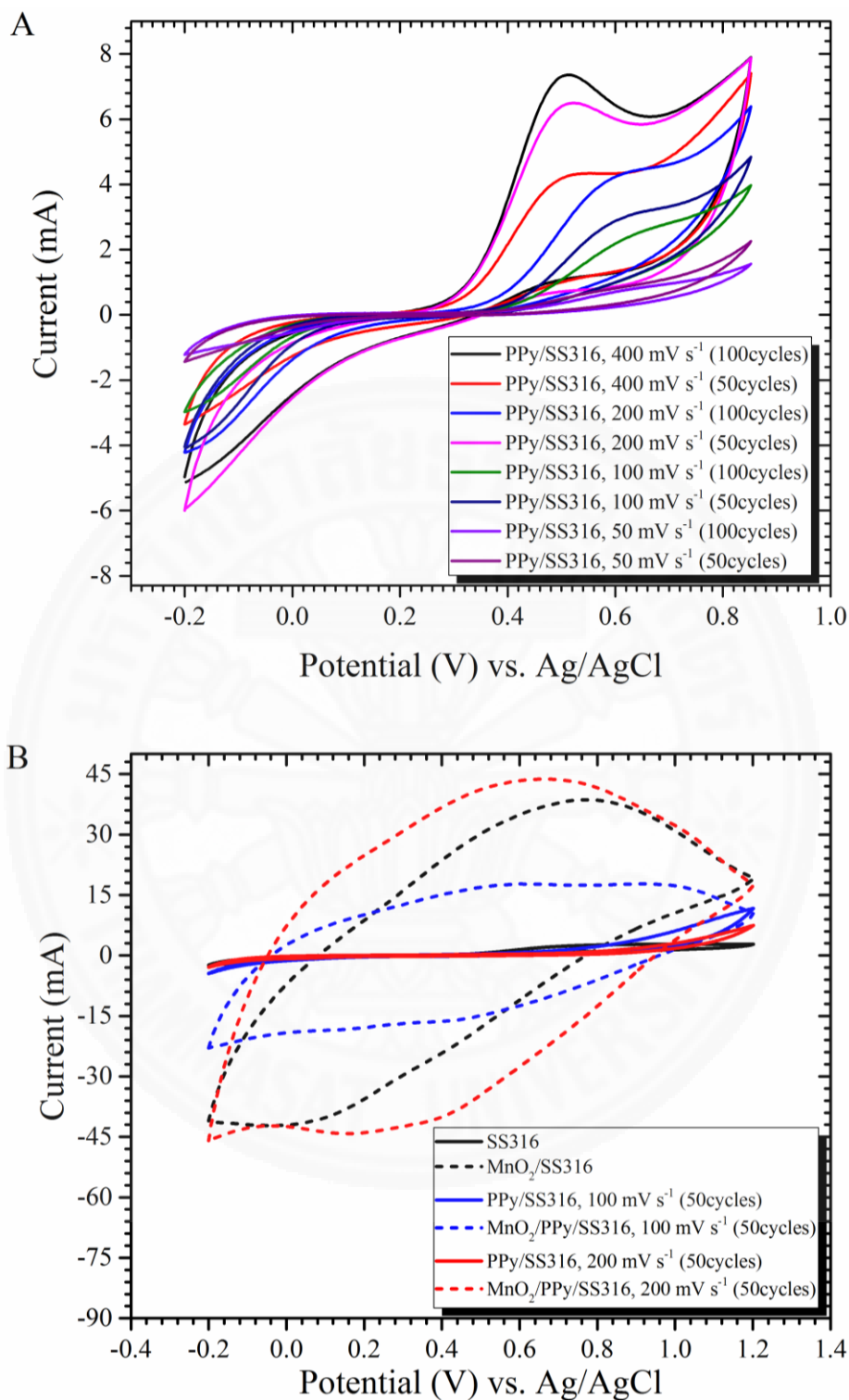


Fig. D-8 CV of 10 mM $K_4Fe(CN)_6$ in 1.0 M KNO_3 solution recorded at various SS 316 electrodes at the same potential scan rate of 100 mV s^{-1} .

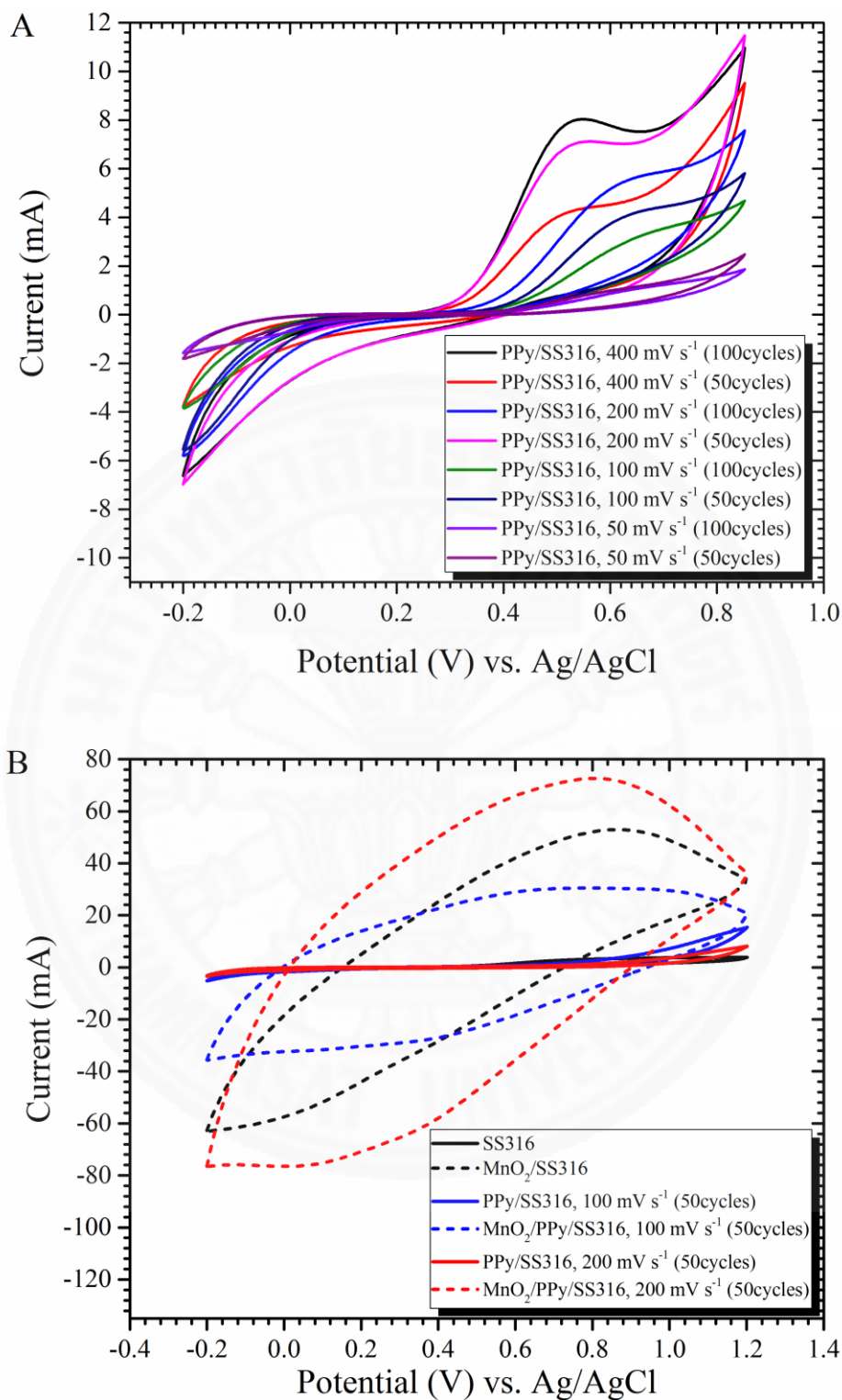


Fig. D-9 CV of 10 mM $K_4Fe(CN)_6$ in 1.0 M KNO_3 solution recorded at various SS 316 electrodes at the same potential scan rate of 200 mV s⁻¹.